

The Effect of an Ozone Layer on Ancient Mars

A Dissertation

Presented to

the faculty of the School of Engineering and Applied Science

University of Virginia

in partial fulfillment

of the requirements for the degree

Doctor of Philosophy

by

Justin Deighan

December

2012

APPROVAL SHEET

The dissertation
is submitted in partial fulfillment of the requirements
for the degree of
Doctor of Philosophy



AUTHOR

The dissertation has been read and approved by the examining committee:


Advisor

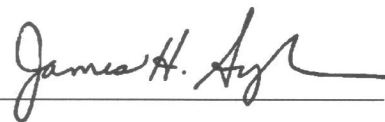








Accepted for the School of Engineering and Applied Science:



Dean, School of Engineering and Applied Science

December
2012

Abstract

The proximity of the planet Mars to Earth, in both distance and characteristics, provides planetary scientists with the opportunity to examine a world both familiar and alien. Here I explore an important possible similarity between ancient Mars and modern Earth: the ability to support a substantial O₃ layer. On Earth, the O₃ layer protects surface life from damaging UV radiation, controls the temperature profile in the stratosphere, acts as a greenhouse gas, and plays an important role in the dissociation of H₂O. While modern Mars lacks a significant O₃ layer, I hypothesize that a thicker atmosphere in the distant past may have been favorable toward the formation of a substantial O₃ layer.

To explore this possibility, I have developed a detailed and optimized 1D radiative-convective model with radiative cross-sections calculated line-by-line to solve the atmospheric energy budget and temperature profile of a terrestrial planet. This is coupled to a photochemical model to calculate the concentration of species, including O₃, produced photochemically in a Martian CO₂-H₂O atmosphere. I find that the optimal conditions for O₃ accumulation are likely to be a 0.3–1 bar CO₂ atmosphere with a planetary surface lacking active weathering and volcanism, as is the case on modern Mars. For plausible O₂ mixing fractions of 10⁻⁵–10⁻² under these conditions, a substantial O₃ layer could form with a column thickness approaching that of modern Earth. These Martian O₃ layers provide significant feedback on photochemistry by shielding the lower atmosphere from UV, humidifying the stratosphere, and providing a source of excited O(¹D) to dissociate H₂O. In contrast, feedback on the energy budget through reduction of planetary albedo, contribution to the greenhouse effect, and suppression of convection

and CO₂ condensation is minor.

While cold, dry periods with little weathering and quiescent volcanism are likely to have been common in Mars' past, it is also of interest to relax these conditions. Therefore, I consider the effect of the ancient Martian surface as an active sink of oxidants and source of volcanic reductants, which produces conditions less favorable to the accumulation of O₃. The results suggest that while a significant amount of weathering and volcanism can still allow for a moderately oxidizing Martian atmosphere, any substantial O₃ layers in the planet's past could only have occurred under relatively cold, dry conditions during an extended period of low volcanic activity.

Table of Contents

Abstract.....	i
Acknowledgments.....	v
List of Variables.....	vi
1. Introduction.....	1
1.1 Conditions for a Thick O ₃ Layer.....	3
1.2 Context in Mars' History and Previous Modeling.....	8
1.3 Summary.....	11
2. Climate-Photochemistry Model.....	13
2.1 Climate Model.....	15
2.1.1 Radiative Cross-sections and Transfer.....	17
2.1.2 Convergence to Radiative-Convective Equilibrium.....	24
2.2 Photochemical Model.....	30
2.2.1 Eddy Diffusion Profile.....	30
2.2.2 Photochemical Reactions.....	32
2.3 Summary.....	39
3. Parameter Space Results.....	40
3.1 Model Validation.....	40
3.2 Climate Parameter Space.....	45
3.3 Photochemistry Parameter Space.....	48
3.3.1 O ₃ Profile and Column.....	49
3.3.2 Energy Budget.....	52

3.3.3 H ₂ O Dissociation.....	56
3.4 Summary.....	60
4. Chemical Surface Sources and Sinks.....	62
4.1 Dry Deposition of Oxidants.....	64
4.1.1 Modern Mars.....	65
4.1.2 Ancient Mars.....	71
4.2 Wet Deposition of Oxidants.....	82
4.3 Volcanic Source of Reductants.....	90
4.4 Summary.....	93
5. Conclusions.....	94
Bibliography.....	97
Appendix A: Heat Capacity of CO ₂	129
Appendix B: Vapor Pressure of H ₂ O ₂	132
Appendix C: Fate of Precipitated H ₂ O ₂	136

Acknowledgments

I would like to thank my adviser Robert E. Johnson for his patience and light but steady touch in guiding my research. I also thank Phil Arras for introducing me to HITRAN and the line-by-line radiative cross-section calculation method, Ben Teolis, Ujjwal Raut, and Aaron Zent for sharing their experience and advice concerning experimental H₂O₂ measurements, and my group mates O.J. Tucker, Justin Erwin, and Meredith Elrod for their advice and friendship. Finally, I give thanks to my supportive friends and family, especially my dear wife, Sara, who is always willing to listen when I encounter problems and help proofread my writing.

List of Variables

P	pressure
T	temperature
T_{eff}	planetary effective temperature
F	energy flux
S	insolation
σ	radiative cross-section; Stefan-Boltzmann constant
ϵ_P	pressure convergence threshold
ϵ_T	temperature convergence threshold
E_P	radiative cross-section pressure error threshold
E_T	radiative cross-section temperature error threshold
ν	wavenumber
γ_D	Doppler half-width
γ_L	Lorentzian half-width
f_i	mixing fraction of species i
Γ	lapse rate
Γ_d	dry adiabatic lapse rate
L	latent heat
l	eddy mixing length
K	eddy diffusion coefficient
H	atmospheric scale height
w	vertical air parcel velocity
c_p	specific heat capacity at constant pressure
ρ	atmospheric density
D	molecular diffusion coefficient
R	aqueous reaction rate
ρ_a	free atmosphere resistance
ρ_b	boundary layer resistance
ρ_c	surface resistance
v_d	deposition velocity
θ	soil porosity
τ	optical depth; soil tortuosity
d	storm depth
p	precipitable water
r	precipitation rate
ω	storm frequency
η	fraction of precipitable water precipitated during storm
X_{ox}	oxidation fraction
z	altitude; subsurface depth

1. Introduction

The planet Mars has long captured the imaginations of scientists, artists, and the general public. Its distinct blood-red hue inspired many civilizations to name it after their god of war: *Nirgal* to the Babylonians, *Mangala* to the Hindus, *Ares* to the Greeks, and *Mars* to the Romans. It is flamboyantly known as the *Fire Star* in Chinese, Korean, and Japanese. In the early 20th century the Red Planet received a boost in public interest due to the enthusiastic observations of Percival Lowell and a flurry of novels centering around Mars, including *The War of the Worlds* by H. G. Wells and *A Princess of Mars* by Edgar Rice Burroughs. When Mariner 4 launched in 1964, scientists were already aware from spectroscopic observations that Mars was a cold desert planet with an average temperature of 210 K. But they also knew that surface temperatures regularly climbed above the freezing point during the day, and most believed that the several millibar of atmospheric CO₂ which had been measured was only a small component of an N₂ atmosphere like Earth's (Kaplan et al. 1964). The possibility was even entertained that seasonal variations in surface color and brightness were due to vegetation, perhaps lichen or some other hardy primitive life existing in favorable microclimates (Lederberg & Sagan 1963). This vision was shattered by the measurements and photographs returned by the flyby of Mariner 4. It was found that the CO₂ represented virtually the entirety of the 6 millibar Martian atmosphere, barely enough to prevent surface water from boiling away. The seasonal surface variations were revealed to be intense dust storms which annually scoured the globe. Moreover, the presence of heavily cratered terrain similar to Earth's moon indicated that much of the planet had seen hardly any resurfacing by water

over the history of the Solar System. The concept of Mars as just a colder, drier version of Earth received a heavy blow.

Yet there are tantalizing signs that there was once a time (or times), however geologically brief, when Mars was indeed somewhat Earth-like. There is now a wealth of chemical and morphological evidence for surface modification by persistent liquid water (Carr & Head 2010). And Mars' atmosphere was not always so thin; significant amounts of atmospheric escape have occurred from the small world since its formation 4.5 billion years ago (R.E. Johnson et al. 2008). The community of scientists studying Mars continues to accumulate evidence from repeated missions, including the current MSL rover *Curiosity* and upcoming MAVEN orbiter, which bolsters and refines the image of a Mars past with a thick atmosphere and liquid surface water, a place bearing great resemblance to our own planet Earth.

Of course, Earth has many other distinct and unique features besides liquid water that set it apart from the other planets in the Solar System. One of the most important of these is the presence of a thick O₃ layer produced photochemically in the stratosphere. It has recently been confirmed that all three atmosphere-bearing terrestrial planets—Venus, Earth, and Mars—posses an O₃ layer of some extent (Montmessin et al. 2011). However, the thick, oxidizing atmosphere of modern Earth is the only one in which O₃ exerts an influence on planetary climate and habitability. Here O₃ has a significant impact on the solar and thermal radiation budgets, being the second most important absorber of ultraviolet (UV) and visible (VIS) radiation and the third most important gas affecting infrared (IR) radiative forcing (Kiehl & Trenberth 1997). This influence on the energy

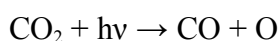
budget allows O₃ to provide substantial photochemical feedback to the climate (Hauglustaine et al. 1994). Stratospheric O₃ also shields surface organisms from damaging solar UV radiation, a critical role which allowed early life to emerge from the sea and colonize the continents (Cockell 2000). In contrast, the O₃ layers observed on Venus and Mars are far too thin to have significant climate feedback, and provide hardly any UV attenuation. Scientific study of O₃ on these bodies is of interest only as probes into atmospheric photochemistry.

However, this does not necessarily mean that O₃ has *never* been an important climate factor on Venus or Mars. It is known that the atmospheres of the terrestrial planets have undergone tremendous evolution over the history of the Solar System (Hunten 1993). For example, Earth maintained a highly reducing atmosphere during its first couple billion years, which was much less favorable to the formation of an O₃ layer than at present (Kasting & Donahue 1980). This raises the question as to whether the other terrestrial planets may have at one time been *more* favorable to the formation of an O₃ layer than they are at present. If this was the case, the resulting energy budget and photochemistry feedback could be important in understanding the planets' climate evolution and habitability. In this thesis I investigate the hypothesis that a thick O₃ layer could have formed on Mars in the past.

1.1 Conditions for a Thick O₃ Layer

In order to identify favorable conditions for the formation of a thick O₃ layer on Mars, it is necessary to understand the fundamental chemistry which drives its production

and destruction. This is intimately connected to the overall oxidation state of the atmosphere, in particular the O₂ content. In an atmosphere irradiated with UV of wavelength $\lambda < 227.5$ nm, CO₂ undergoes photolysis



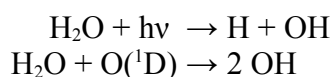
Counteracting this is the three body recombination process



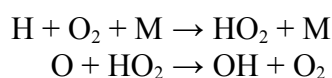
where M is a non-reacting background species, most likely another CO₂ molecule for the Martian atmosphere, the presence of which is required for conservation of energy and momentum. However, this reaction is spin-forbidden, making it very slow at recombining CO₂. This allows time for a much faster competing reaction



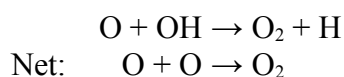
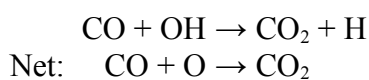
to accumulate a significant concentration of CO and O₂ in equilibrium. Under this mechanism, one would expect a stoichiometric CO:O₂ ratio of 2:1, and mixing fractions of order 10⁻² in the modern Martian atmosphere. However, the actual ratio is closer to 1:2 with a mixing fraction order 10⁻³. This is because the atmosphere of Mars is sufficiently humid that “odd hydrogen” HO_x (H, OH, HO₂) produced by H₂O dissociation catalytically accelerates this chemistry (McElroy & Donahue 1972; Parkinson & Hunten 1972). The H₂O dissociation can occur either by direct photolysis or attack by O(¹D), an O atom in its first excited state



O(¹D) is produced mainly via photolysis of CO₂ or O₂ by very energetic UV photons ($\lambda < 167$ nm and 175 nm, respectively), or O₃ by less energetic UV photons ($\lambda < 310$ nm). The primary catalytic HO_x mechanisms share the same first two steps

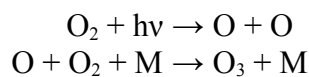


with the last depending on whether CO₂ recombination or O₂ formation takes place

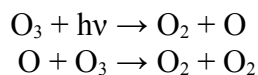


Another complication is that the Martian atmosphere cannot be considered a closed-system from the standpoint of humid photochemistry. When H₂O is dissociated, it produces the stable species H₂ and ½ O₂ through a series of reactions involving HO_x. The H₂ mixes up to the top of the atmosphere, where it is dissociated to H and efficiently lost to space by thermal Jean's escape (R.E. Johnson et al. 2008). This leaves behind an excess of O in the atmosphere, which on modern Mars cannot efficiently escape to space or be weathered out at the surface, and so the atmosphere oxidizes until the O loss rate is large enough to stoichiometrically match the H loss to space in a 1:2 ratio. It is this combination of HO_x chemistry and H escape that controls the equilibrium O₂ content of the modern Martian atmosphere.

The core mechanism for the production and destruction of O₃ in an oxidizing atmosphere was identified by Chapman (1930). In this scheme O₃ is produced via

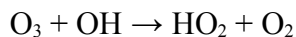
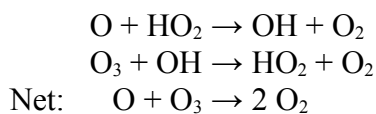
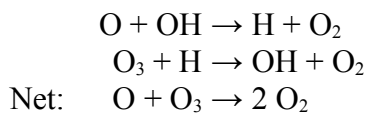


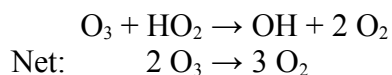
and destroyed by the reactions



In an atmosphere where O_2 is stable and well mixed, its concentration will increase exponentially as one descends through the atmosphere due to hydrostatic equilibrium. At the same time, however, the amount of UV radiation which can produce O via photolysis will decrease as it is absorbed by the overlying column of atmosphere. This gives rise to the so-called Chapman profile, with an initially increasing concentration of O_3 as one descends through the “ O_2 starved” atmosphere, followed by a peak near the altitude where most of the photolyzing radiation has been absorbed, and finally ending in an “ O starved” region where the O_3 concentration declines (Chapman 1930). This behavior produces the stratospheric O_3 layer shape we are familiar with on Earth. On Mars, however, the atmosphere is so thin that its O_3 layer has not yet “peaked” by the time the planet's surface is reached; it is the equivalent of being in the middle of Earth's stratosphere.

In both planets' atmospheres the destruction of O_3 is accelerated by a number of catalytic HO_x cycles which consume “odd oxygen” O_x (O , O_3)





These reactions make the destruction rate of O_3 highly dependent on the local content of HO_x . The majority of Earth's O_3 layer is in the dry, stable stratosphere, which has only a few ppm H_2O , and O_3 is able to accumulate to a column density of $\sim 10^{19} \text{ cm}^{-2}$. Some O_3 from the lower stratosphere is mixed down into the troposphere, the wet, turbulent lower part of the atmosphere, where its lifetime is limited. While there, its photolysis provides a large source of $\text{O}(^1\text{D})$, which drives dissociation of H_2O . This is the primary H_2O dissociation path on Earth, since the stratospheric O_3 layer also blocks direct photolysis of H_2O in the troposphere (Levy 1971). In contrast, most of the O_3 in the current thin Martian atmosphere would be expected near the surface, where the average H_2O content is a few *hundred* ppm. As a result, destruction by HO_x is rapid and the O_3 column is $< 10^{16} \text{ cm}^{-2}$, less than 0.1% the thickness of Earth's O_3 layer and orders of magnitude lower than expected assuming only the Chapman cycle. This depleted O_3 layer produces little $\text{O}(^1\text{D})$ and blocks little UV, so that H_2O dissociation is dominated by direct photolysis (Nair et al. 1994).

Given this analysis, under what conditions would Mars be more favorable to the formation of a thick O_3 layer? This question has been previously raised in the literature by Hiscox & Lindner (1997), though in the interest of engineering Mars to be more Earth-like rather than in the context of paleoclimates. In considering the three-body reaction by which O_3 is produced, Hiscox & Lindner (1997) pointed out that increasing the concentration of either $[\text{O}]$, $[\text{O}_2]$, or $[\text{M}]$ will directly increase the concentration of O_3 .

On Mars, much of the O and O₂ are derived from the photolysis of CO₂, so the presence of a denser CO₂ atmosphere will generally amplify the concentrations of all three species. The reaction rate also has a negative dependence on temperature, making O₃ production faster at lower temperatures. On the other hand, since destruction of the oxidizing species O, O₂, and O₃ in the Martian atmosphere is accelerated by HO_x, a drier atmosphere will increase [O] and [O₂] and reduce the destruction rate of O₃. A thick and cold atmosphere will also contribute to reducing HO_x by shielding H₂O from UV and lowering its vapor pressure, respectively. Finally, a thicker atmosphere would raise the altitude of O₃ production up above the troposphere and into the stratosphere, as on Earth, where many of these favorable conditions exist. From this analysis, Hiscox & Lindner (1997) concluded that a dense, cold, and dry atmosphere would be most likely to produce a thick O₃ layer on Mars.

1.2 Context in Mars' History and Previous Modeling

Having identified a dense, cold, and dry Martian atmosphere as being most favorable to an O₃ layer, it is useful to consider these conditions in the context of what we know about Mars history and the previous climate and photochemical modeling that has been done. As mentioned in the introduction, one of the primary drivers in studying Mars is understanding the chemical and morphological evidence for extensive and persistent liquid water on the surface at some time in the past (Carr & Head 2010). However, climate modeling continues to struggle to achieve average surface temperatures above 273 K on Mars, even under the enhanced greenhouse effect of a thicker CO₂ atmosphere

(Kasting 1991). One approach to solving, or at least alleviating, this discrepancy is the invocation of additional trace greenhouse gases such as CH₄, H₂S, and SO₂ (Halevy et al. 2009; S.S. Johnson et al. 2008; Kasting 1997; Squyres & Kasting 1994). These species require a reducing atmosphere in order to accumulate to effective concentrations, as well as a major geochemical source of replenishment. These conditions could be met by large scale volcanism, and, though Mars is currently inert, there is extensive evidence for past activity, including *Olympus Mons*, the largest volcano in the Solar System. This paradigm results in a picture of early Mars not unlike Archean Earth (Halevy et al. 2007; S.S. Johnson et al. 2009; Tian et al. 2010). Under such a warm, wet, and reducing scenario, oxidizing species would be rapidly destroyed both in the atmosphere and in aqueous solution at the surface (Kasting et al. 1979; Kasting & Walker 1981; Kasting et al. 1985). What little O₃ could exist under such conditions would have negligible feedback on the climate. However, Martian volcanism has been episodic throughout the planet's history, with the most recent large scale caldera activity ending ~100–200 Ma (Neukum et al. 2010; Robbins et al. 2011). During volcanically quiescent geologic periods (such as the current time), any climate-influencing volcanic gases would become depleted and the atmosphere would relax to a colder, drier state. This would allow for the accumulation of oxidizing species such as O₂ and O₃ (Kasting 1995). With atmospheric photochemical equilibrium being achieved in a relatively short period of geologic time (~0.1 Myrs on modern Mars (Zahnle et al. 2008)), many of these volcanic interludes would have experienced oxidizing conditions.

To ascertain whether O₃ feedback was ever significant on Mars, I will focus in

Chapter 3 on the characterization of climate feedback processes during these cold, dry, volcanically quiescent periods of Mars' history. Such conditions provide an optimal, while still plausible, scenario for O₃ accumulation on ancient Mars. However, since such climates are decidedly un-Earth-like, it is also of interest to explore how much weathering and volcanism the Martian atmosphere could tolerate before transitioning to a less oxidizing state. This line of inquiry will be examined in Chapter 4.

The photochemistry relevant to a thick CO₂ atmosphere lacking volcanism has been examined by several authors (Hiscox & Lindner 1997; Rosenqvist & Chassefière 1995; Segura et al. 2007; Selsis et al. 2002; Zahnle et al. 2008). The ability of trace amounts of a strong UV absorber (SO₂) to modify the ancient Martian atmosphere's temperature structure has also been demonstrated (Yung et al. 1997). However, the feedback between a photochemical product such as O₃ and the planetary thermal structure has received less attention. Hiscox & Lindner (1997) made the case that a Martian CO₂ atmosphere thick enough to support liquid water at the surface would also produce an O₃ layer substantial enough to shield the surface from UV radiation and contribute to the greenhouse effect. However, their analysis was rough and somewhat qualitative, lacking detailed photochemical calculations. The studies of Rosenqvist & Chassefière (1995), Segura et al. (2007), and Zahnle et al. (2008) used a fixed temperature profile for their photochemical calculations. Selsis et al. (2002) did examine feedback between O₃ photochemistry and the temperature profile, but this was not the focus of the study and a converged solution was not achieved due to excessively long run times.

Here I take a complementary approach. A detailed 1D radiative-convective model

with radiative cross-sections calculated on a line-by-line basis is used, with optimizations to allow timely convergence for practical climate calculations. This is coupled to a simplified photochemical model containing the basics of O₃ photochemistry, but neglecting atmospheric mixing and HO_x reactions. This provides a first order estimate of stratospheric O₃ concentration while ensuring timely model convergence. Comparison with a fully detailed photochemical model is performed to demonstrate the validity of such simplifications under the conditions of interest. Using the simple model I explore the parameter space of atmospheric pressure, insolation, and O₂ mixing fraction to identify conditions likely to support a substantial O₃ layer, and then examine the significance and robustness of its feedback on the climate. A number of case studies including weathering and volcanic activity are also examined using the full photochemical model in order to estimate the extent to which these processes could operate without upsetting an oxidizing atmosphere.

1.3 Summary

This thesis examines the question of whether Mars could have ever maintained an O₃ layer thick enough to provide significant feedback on climate and photochemistry through its influence on the energy budget, as is the case on modern Earth. The conditions most likely to support the hypothesized O₃ layer are a dense, cold, dry atmosphere. Such a scenario is possible in the early history of Mars during geologic periods of quiescent volcanic activity. It is also of interest to examine more Earth-like atmospheric conditions which are sub-optimal for the accumulation of O₃, and toward

this end I estimate the amount of weathering and volcanic activity that an ancient Martian climate could tolerate without converting to a highly reducing state.

2. Climate-Photochemistry Model

To investigate the feedback of O_3 on Martian climate, a model capable of evaluating both the energy budget and photochemistry is required. Here this is achieved using a vertical 1D radiation-convection model to calculate globally averaged climatic conditions, which is self-consistently coupled to a photochemical model to calculate the concentrations of photochemical species like O_3 . The coupling between the climate model and photochemical model is conceptually straight forward. The climate model balances the planetary energy budget and calculates vertical profiles for temperature, pressure, and radiative flux based on a given chemical composition of the atmosphere. To initialize the program, the atmosphere is taken to consist only of CO_2 and H_2O . The resulting vertical profiles are then fed to the photochemical model, which solves for the chemical composition of the atmosphere by calculating the production and destruction rates of species (CO , O_2 , $O(^1D)$, O , O_3 , H_2 , H , OH , HO_2 , H_2O_2 , $HOCO$) generated from the dissociation of CO_2 and H_2O . Some of these, particularly O_2 and O_3 , modify the energy budget, and so the climate model is executed again. This in turn modifies the environmental conditions, and the photochemical model must be iterated once more. The sequence is repeated until both the climate model and photochemical model have converged. This is generally taken to be when atmospheric variables (e.g. temperature, species concentration) change only at the 6th decimal place after an iteration. A control flow diagram (CFD) of the coupled climate-photochemistry model is depicted in Diagram 2.1.

The domain of the climate-photochemistry model extends from the planet's

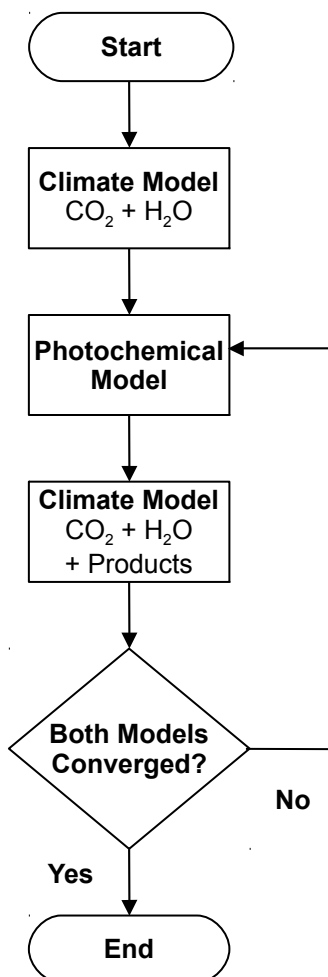


Diagram 2.1: Control flow diagram for coupled climate-photochemistry model.

surface up to the altitude where atmospheric pressure approaches 10^{-6} bar (0.1 Pa). The domain is divided into layers of equal thickness, with a nominal size of 2 km. During development, testing was often performed at higher resolutions, including 1 km and 0.5 km, to ensure that the atmosphere was sufficiently well resolved. The upper cut-off of 10^{-6} bar is chosen to be low enough to avoid many of the complex effects found in the upper atmosphere. These include (1) the onset of the ionosphere, where a significant fraction of the atmosphere becomes plasma and electron/ion chemistry is important, (2)

transition of the dominant mass transfer mechanism from eddy diffusion to molecular diffusion at the homopause, (3) transition of the dominant heat transfer mechanism from radiation to conduction at the mesopause, and (4) violation of local thermodynamic equilibrium, due to infrequent collisions between molecules (Bougher et al. 2008, López-Valverde et al. 1998). These characteristics derive from the intense high energy radiation and rarefied atmospheric conditions at the top of the atmosphere. While the upper atmosphere certainly has an effect on the lower atmosphere, particularly via the escape of species to space, the small amount of matter contained there is dwarfed by the bulk of the middle and lower atmosphere. This means that the upper limit of the model is justified in terms of capturing the majority of CO₂ and H₂O photolysis occurring in the Martian atmospheres studied. It is also sufficiently high that any O₃ layer is not prematurely truncated on its upper side.

2.1 Climate Model

The climate model generates the atmospheric structure of pressure P , temperature T , and energy fluxes F by balancing the energy budget for radiative-convective equilibrium. The surface pressure P_s is held fixed for a given run, and the vertical P profile then derived from the T profile by assuming that the atmosphere is in hydrostatic equilibrium. The T profile is determined by setting the net F for each layer in the atmosphere to zero. F takes into account absorption of solar radiation, thermal absorption and emission, and convective heat transport. Calculation of F requires radiative cross-sections σ , which themselves depend on P and T .

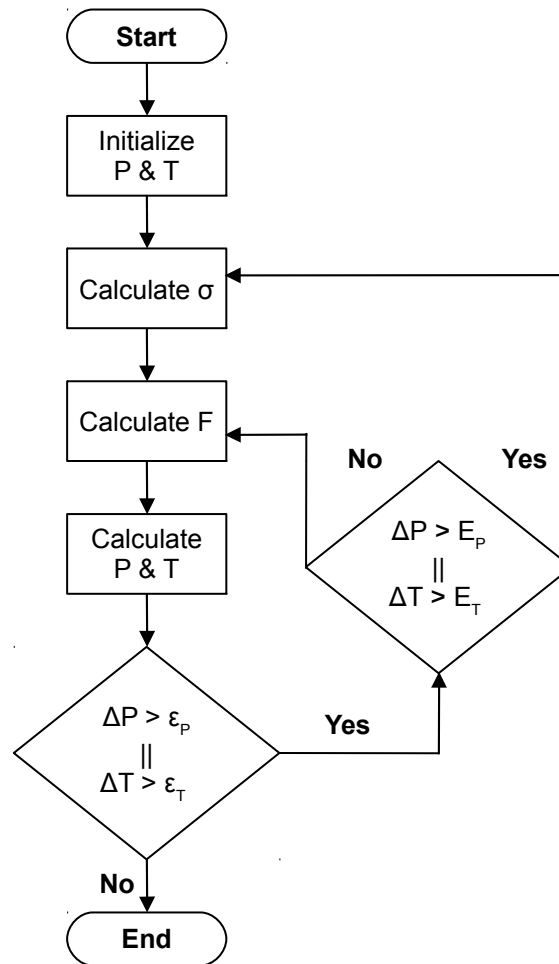


Diagram 2.2: Control flow diagram of the climate model. P is pressure, T is temperature, σ represents the radiative cross-sections, F is the energy flux, ΔP and ΔT are the changes in their respective variables over an iteration, ϵ_P and ϵ_T are the acceptable errors in these variables for convergence, and E_P and E_T are the acceptable errors for calculation of σ .

The manner by which the climate model achieves equilibrium is depicted as a CFD in Diagram 2.2. The program is initialized using an estimate for the T profile, with an isothermal atmosphere at the planet's equilibrium temperature typically being sufficient. The P profile is then derived from this, which allows for the calculation of σ .

This is followed by the calculation of F , and finally the adjustment of the T profile necessary to balance the atmospheric energy budget. If both of the resulting changes ΔP and ΔT are sufficiently small, less than some error thresholds ε_P and ε_T , then convergence is considered complete. If not, new F need to be calculated and P and T adjusted again, in a march toward equilibrium. While σ could be recalculated every time F needs to be evaluated, this proves to be prohibitively time-consuming for the detailed cross-section calculation method used in this thesis. In the interest of computational economy, an additional step is added which determines whether ΔP and ΔT are large enough to warrant recalculation of σ , as determined by the error thresholds E_P and E_T . These are actively adjusted during iteration to maintain an error in σ that is less than $\Delta F/F$ from the previous iteration. This ensures that the error in F due to suspending recalculation of σ is always less than the error due to P and T not yet being in equilibrium.

2.1.1 Radiative Cross-sections and Transfer

At the core of the radiative model is a line-by-line (LBL) calculation of wavelength dependent radiative opacity in the visible/infrared (VIR). The decision to develop and use a LBL code is motivated by recent concerns that the standard 1D models of ancient Mars, such as used by Pollack et al. (1987) and Kasting (1991), suffer from serious parameterization issues. For example, the treatment of collision-induced-absorption (CIA) by CO_2 molecules has been handled improperly in the past (Halevy et al. 2009; L. Kaltenegger, pers. comm., 2009; Wordsworth 2010a). This CIA becomes important when calculating radiation transfer in thick CO_2 atmospheres (> 0.1 bar) and is

a critical aspect of the energy budget for ancient Martian climates. There is also a broader concern with the correlated-k technique commonly used to calculate radiative transfer in many terrestrial planet climate models. The correlated-k technique became popular in the 1970–1980s due to its ability to divide the solar and infrared spectra into a few broad bands for treatment instead of attempting to resolve hundreds of thousands of radiative lines for each major radiatively active species. This feature of correlated-k was critical for practical applications due to limitations in computational power at that time. However, recent work has demonstrated that correlated-k parameterizations commonly used for Earth result in radiative forcing by H₂O and O₃ which can deviate significantly, up to 200%, from those given by LBL calculations (Forster et al. 2011). Specifically, when atmospheric temperature or the concentration of a radiatively active species does not decrease with altitude, the fundamental assumptions of the correlated-k technique are violated (Tvorogov et al. 2005). While for some applications this limitation may not be critical, it is particularly relevant to the modeling of O₃ layers on Mars, since it is anticipated that both temperature and O₃ concentration will increase with altitude in the lower stratosphere.

While LBL calculation is more fundamentally correct than other methods and is important for benchmarking the accuracy of alternative techniques, it has been rejected for many applications in the past because it is computationally slow (Liou 2002). However, given new optimization techniques and the steady advance in computing power, such models are becoming more common in planetary science (Corrêa et al. 2005; Letchworth & Benner 2007; Kuntz & Höpfner 1999; Quine & Drummond 2002; Wells

1999).

In order to calculate radiative properties LBL, a database of line characteristics is needed, such as HITRAN (Rothman et al. 2009). The effects of Doppler broadening by temperature and pressure broadening by neighboring molecules on each radiative transition may then be taken into account. Non-zero temperatures broaden the line by Doppler shifting, making the lineshape a “Doppler profile” (also known as the Gaussian distribution) in the low pressure limit. This is characterized by the “Doppler half-width”, i.e. the distance from the line center to where the profile is reduced to half its value at the center

$$\gamma_D = \nu_0 \sqrt{\frac{2 \ln(2) k T}{m c^2}} \quad (2.1)$$

with ν_0 being the wavenumber of the line center, k is Boltzmann's constant, c is the speed of light in vacuum, T is the temperature, and m is the radiating molecule's mass. In the high pressure limit (typically > 0.1 bar), perturbations due to the collisional impact of surrounding atmospheric molecules with the radiating molecule produce a “Lorentzian profile” (also known as a Cauchy distribution)

$$\alpha_L(\nu) = \frac{1}{\pi} \frac{\gamma_L}{\gamma_L^2 + (\nu - \nu_0)^2} \quad (2.2)$$

The characterizing “Lorentzian half-width” γ_L is taken from tabulated values in HITRAN and adjusted for a given temperature and pressure. To accurately calculate the line shape at intermediate pressures, the Doppler and Lorentzian profiles must be convoluted to produce the Voigt profile

$$\alpha_V(x, y) = K_0 \frac{y}{\pi} \int_{-\infty}^{\infty} \frac{e^{-t^2}}{(x-t)^2 + y^2} dt \quad (2.3)$$

Where $K_0 = 1/\gamma_D \sqrt{\ln(2)}/\pi$, $x = (v - v_0)/\gamma_D \sqrt{\ln(2)}$, and $y = \gamma_L/\gamma_D \sqrt{\ln(2)}$. The Voigt has no closed form solution, and there are a wide variety of approaches to calculating the function depending on the desired accuracy and speed. Many methods include decomposition of the x and y parameter space into separate domains where tractable approximations may be made which apply to each domain. For both large x and y , the Voigt profile approaches a Lorentzian profile. Since calculating values in this domain constitutes most of the radiative calculations performed, I have developed an approximation of Eq. (2.3) in this limit. It is based on expanding the Lorentzian profile as a Taylor series and then integrating this as a series of Gaussian moments with the Taylor coefficients as weights, effectively a Gauss-Hermite quadrature. This is then readily reorganized in terms of the Lorentzian as a power series, providing a conceptually and computationally efficient analytical approximation. The resulting form is

$$\alpha_V(x, y) = \sum_{i=1} c_i(y) \alpha_L(x)^i \quad (2.4)$$

where the y dependencies have been consolidated into the c_i coefficients. Since the value of y is constant at all x for a given line, the coefficients need only be calculated once for all sample points along the line profile. Using just a few terms of the series, the wings of the Voigt profile may be calculated to within a few half-widths of the line center while maintaining error $< 1\%$ under all pressure conditions. The computational efficiency is competitive with state of the art, and is similar to the method of Letchworth & Benner

(2007) in the same domain. For the relatively small number of calculations of the Voigt profile close to the center of radiative lines, the IMSL Numerical Library is used, as it is found to provide excellent accuracy at an acceptable speed.

Within the radiative transfer model the spectrum is divided into two regions: a UV region from 119 nm to 400 nm at 1 nm resolution and a visible/infrared (VIR) region ranging from 25000 cm^{-1} (400 nm) to 0 cm^{-1} with a non-uniform grid. The resolution of the pre-computed VIR grid varies from $2^{-15}-1 \text{ cm}^{-1}$ in order to resolve individual radiative lines at one half-width or better, and is optimized for the input parameters of a given run. This is accomplished by first producing an array of 16-bit integers, with each integer corresponding to a bin in a grid at 2^{-15} cm^{-1} resolution, giving $\sim 10^9$ bins across the wavenumber domain and occupying ~ 1.5 GB of computer memory. Each bit in a 16-bit integer is used to represent a level in a series of grids with binarily decreasing resolution. A “1” for the 0th bit (the “first” or “Least Significant Bit”) indicates that a 2^0 cm^{-1} bin would be sufficient to accurately resolve spectral features at that location in wavenumber space. Likewise, the next bit indicates that a 2^{-1} cm^{-1} bin would be sufficient, the next indicates 2^{-2} cm^{-1} to be sufficient, etc. The array of integers is initialized to resolve at $2^0 = 1 \text{ cm}^{-1}$, i.e. the first bit is “1” and the rest “0”. Then, for each radiative line, the minimum necessary resolution needed to achieve 1% error in the cross-section for a constant value in each bin is computed, and the corresponding bit is set appropriately. Finally, the array of integers is scanned to determine the highest bit set for each bin after this process, as this indicates the maximum resolution needed for that location in wavenumber space. The non-uniform optimized grid is then generated based on this information, and typically

contains only $\sim 10^6$ bins.

The solar radiation source in the UV is taken from the ASTM E-490 reference spectrum, and VIR radiation uses the synthetic spectrum provided by the AER group (Clough et al. 2005), which is generated from the Kurucz (1992) solar source function. A solar zenith angle of 60° is used in order to globally average the incident flux, and a factor of 1/2 is applied for diurnal averaging. Absorption by CO_2 , H_2O , and O_3 is considered in both spectral regions and O_2 is included in the UV.

UV cross-sections are obtained from various authors via the MPI-Mainz-UV-VIS Spectral Atlas of Gaseous Molecules and Sander et al. (2011). Temperature dependent CO_2 UV cross-sections are used via linear interpolation of data at 295 K and 195 K, being held constant below 195 K. The temperature sensitive Schumann-Runge bands of O_2 in the UV are computed via the method of Minschwaner et al. (1992) and binned at 1 nm.

VIR cross-sections are calculated LBL, as described previously, using the 2008 HITRAN database (Rothman et al. 2009). Pressure broadening and line shifting of H_2O lines by CO_2 instead of air (N_2/O_2) is implemented using the results of Brown et al. (2007). This increases pressure-broadened half-widths by a factor of 1.7 on average relative to terrestrial air. Based on this, pressure-broadened half-widths of O_3 lines in air are multiplied by 1.7, since data on CO_2 pressure-broadening of O_3 is lacking. A Voigt line shape profile is used out to 40 Doppler half-widths from the line center and beyond that a van Vleck–Weisskopf profile is used. The van Vleck–Weisskopf profile is simply a Lorentzian differenced with its mirror image reflected around $\nu = 0$, and provides the correct limit at short wavenumbers as $\nu \rightarrow 0$. For H_2O and O_3 a Lorentzian wing cut-off

of 25 cm^{-1} from the line center is used, while sub-Lorentzian CO_2 wings are treated by using empirical χ -factors with a maximum cut-off of 500 cm^{-1} (Halevy et al. 2009; Wordsworth et al. 2010a). The χ -factor of Perrin & Hartmann (1989) is used in the wavenumber range $0\text{--}3000 \text{ cm}^{-1}$, that of Tonkov et al. (1996) is used for $3000\text{--}6000 \text{ cm}^{-1}$, and that of Meadows & Crisp (1996) is used $> 6000 \text{ cm}^{-1}$.

For H_2O and O_3 only the most common isotopologues are used (H^{16}OH , $^{16}\text{O}^{16}\text{O}^{16}\text{O}$), while for CO_2 the three most common isotopologues are considered ($^{16}\text{O}^{12}\text{C}^{16}\text{O}$, $^{16}\text{O}^{13}\text{C}^{16}\text{O}$, $^{16}\text{O}^{12}\text{C}^{18}\text{O}$). Also, for each layer, weak radiative lines are excluded from calculations based on the criterion of optical depth $\tau < 0.01$ at the line center when integrated across the overhead atmospheric column. These measures are taken for computational economy, and including rarer species and weaker lines has a negligible ($< 1 \text{ K}$) effect on the temperature profile.

CO_2 CIA is accounted for using the “GBB” parameterization of Wordsworth et al. (2010a). This is based on the experimental work of Baranov et al. (2004) and Gruszka & Borysow (1998). The Chappuis and Wulf continua of O_3 in the VIR are sampled at 1 cm^{-1} from the MT_CKD continuum model (Clough et al. 2005). Rayleigh scattering cross-sections for CO_2 are calculated from its refractive index. In the UV the refractive index is taken from Bideau-Mehu et al. (1973), while in the VIR the results of Old et al. (1971) are used. In both regions the King correction factor is taken from Alms et al. (1975).

For radiative transfer the plane-parallel approximation is used and treatment follows a two-stream method, applying the technique of Toon et al. (1989) for scattering of solar radiation. Since clear sky conditions are assumed, the only significant scattering

in the atmosphere is due to Rayleigh scattering. The planet's surface is taken to be a grey Lambertian reflector with an albedo of 0.20 for solar radiation and an emissivity of 1.0 for thermal radiation.

2.1.2 Convergence to Radiative-Convective Equilibrium

The model solves for the temperature profile by iteratively calculating the net flux F_{net} for each layer in the atmosphere and then setting it to zero. This is done by assuming that the absorbed flux is constant, and adjusting the emitted flux F_{emt} by changing the layer temperature T . To find the necessary step size ΔT , an estimate of the derivative dF_{emt}/dT is required. I begin by taking the emitted flux to be

$$F_{emt} = \pi \int_0^{\infty} B(\nu, T) (1 - e^{-\tau(\nu, T)}) d\nu \quad (2.5)$$

By assuming that $e^{-\tau}$ has a weak dependence on temperature over the interval ΔT , the derivative may be approximated as

$$\frac{dF_{emt}}{dT} \approx \pi \int_0^{\infty} \left[\frac{dB}{dT} \right]_{\nu} (1 - e^{-\tau(\nu, T)}) d\nu \quad (2.6)$$

For the conditions considered here, the radiatively active $\nu_2 = 667 \text{ cm}^{-1}$ bending mode of CO_2 dominates thermal transfer in the stratosphere, where the atmosphere is in radiative equilibrium. This allows for two more useful approximations. First, thermal emission occurs in the high energy tail of the Planck function at the temperatures of interest ($T \ll \theta_2 = 960 \text{ K}$), allowing the simplification

$$\frac{dF_{emt}}{dT} \approx \pi \int_0^{\infty} \frac{h\nu}{kT^2} B(\nu, T) (1 - e^{-\tau(\nu, T)}) d\nu \quad (2.7)$$

Second, the ν_2 emission band is approximated as a δ -function

$$\frac{dF_{emt}}{dT} \approx \frac{h\nu_2}{kT^2} \pi \int_0^{\infty} B(\nu, T) (1 - e^{-\tau(\nu, T)}) d\nu \quad (2.8)$$

which is readily recognized as

$$\frac{dF_{emt}}{dT} \approx \frac{h\nu_2}{kT^2} F_{emt} \quad (2.9)$$

This simple formulation is surprisingly accurate under the conditions for which it is derived, with typical errors $< 1\%$ compared to a (much slower) numerical integration without approximations.

The surface temperature is also marched toward convergence by adjusting F_{emt} based on F_{net} . However, since the surface is treated as a greybody, Eq. (2.5) simplifies to the Stefan-Boltzmann law multiplied by a characteristic emissivity ε

$$F_{emt} = \varepsilon \sigma T^4 \quad (2.10)$$

The derivative of this equation is readily found

$$\frac{dF_{emt}}{dT} = 4 \frac{F_{emt}}{T} \quad (2.11)$$

and the only remaining step is to determine what value to use for T . A naive assessment would indicate that the surface temperature T_s would be appropriate. However, this results

in stability issues when the atmosphere is opaque enough to intercept a large fraction of the surface's thermal emission, because T_s becomes less directly coupled to the total energy balance of the planet. I find that highly satisfactory behavior is achieved by setting T equal to the planet's effective temperature $T_{eff} = (F_{\uparrow, top}^{IR} / \sigma)^{1/4}$, where $F_{\uparrow, top}^{IR}$ is the upward IR flux at the top of the atmosphere and σ is the Stefan-Boltzmann constant. T_{eff} is identical to T_s for a radiatively transparent atmosphere, and provides the necessary sensitivity to the total energy balance when atmospheric absorption and emission strongly modify the IR flux.

After the atmospheric and surface temperatures have been modified by the ΔT factors derived above, a convective adjustment is applied in any layers where the lapse rate exceeds the threshold for convective instability. In an atmosphere without condensing species, the dry adiabatic lapse rate is $\Gamma_d = g/c_p$, where g is gravitational acceleration and c_p is the specific heat capacity of the atmosphere. Here I use a theoretical expression for the heat capacity of CO_2 at zero-pressure which closely matches experiment, and account for higher pressure corrections using a Virial expansion; details are available in Appendix A.

In an atmosphere which experiences condensation during convection, the release of latent heat may significantly alter the critical lapse rate from the dry adiabat. As a simple model of precipitation, it is assumed that the condensate is rapidly removed from the site of condensation. For the condensation of a minor species, such as H_2O , this yields the pseudo-adiabatic lapse rate

$$\Gamma = \Gamma_d \frac{1 + \frac{P_v L}{P R T}}{1 + \frac{P_v L^2}{c_p P R T^2}} \quad (2.12)$$

where P_v is the partial pressure of the condensing vapor, P is the total atmospheric pressure, L is the latent heat of condensation, and R is the universal gas constant. The surface is taken to be an H_2O source at a specified relative humidity (RH). The H_2O profile is determined differently depending on whether the simple or full photochemical model is used, as discussed in Section 2.4.

The condensation of CO_2 may also affect the lapse rate in a thicker Martian atmosphere, as pointed out by Kasting (1991). In this case the critical lapse rate is such that the P - T relationship corresponds to the vapor pressure curve of CO_2 . In this work the vapor pressure of CO_2 is calculated using the formulation of Span & Wagner (1996). The effect of CO_2 clouds on the energy budget are not included (Forget & Pierrehumbert 1997). These structures may act to either warm or cool the lower atmosphere depending on cloud thickness and altitude (Mischna et al. 2000). Detailed microphysics of the CO_2 condensate must be considered to properly model these values, making them sensitive to dust, water vapor, and dynamical phenomena which require a 3D model (Colaprete & Toon 2003). Work in this field is ongoing, and beyond the scope of this thesis. I therefore limit my comments on CO_2 condensation in the results to how thick the atmosphere must be for condensation to begin in the middle atmosphere. It should be noted that even if CO_2 condensation does not occur in an equilibrium solution, it could still be present on a limited local scale, as it is on Mars today. This occurs in cold regions at high latitude

(Kelly et al. 2006) and in the mesosphere due to temperature fluctuations driven by atmospheric waves (Montmessin et al. 2006). While forgoing any detailed calculations, it may be hypothesized that an O₃ layer would interact strongly with CO₂ clouds through both the energy budget and photochemistry. As will be seen in Chapter 3, local heating by an O₃ layer can inhibit CO₂ condensation at high altitudes, and even prevent it altogether in some cases. Atmospheric transport of O₃ is not considered in those results, and it is expected that convection driven by CO₂ condensation would bring down O₃ from the stratosphere and increase heating, thereby acting to dissipate CO₂ clouds. On the other hand, the CO₂ clouds would scatter back upwards some solar radiation otherwise absorbed by the surface. This extra radiation would increase both O₃ heating and photolysis, which act to reduce its concentration. These lines of thought suggest that the interplay between an O₃ layer and CO₂ clouds in thick terrestrial atmospheres is a rich area of study that should be considered in future research.

It was specified previously that the ν_2 band of CO₂ generally dominates thermal radiative transfer in the stratosphere. However, one might question the propriety of this approximation in thick, warm, wet atmospheres, where other CO₂ bands and H₂O can become important. Under such conditions, the IR spectrum becomes filled in and the representation of atmospheric opacity by a δ -function at 667 cm⁻¹ breaks down. Instead, the radiative characteristics approach that of a greybody, like the planet's surface, with significant opacity at most IR wavelengths. As a point of comparison between the ν_2 approximation and a greybody, the factor $h\nu_2/kT \approx 4$ when $T \approx 240$ K. Coincidentally, this is roughly the temperature at which the vapor pressure of H₂O is high enough that it

becomes a significant greenhouse gas in these Martian simulations. Even at $T \approx 273$ K, it is found that $h\nu_2/kT \approx 3.5$, which is sufficiently close to the actual derivative that there is no significant penalty to the rate of convergence. This serendipity allows the use of Eq. (2.9) for efficient convergence throughout the Martian atmosphere and across the entire parameter space of pressure and insolation.

However, an unrelated issue with convergence by this method does arise when lower layers in the atmosphere become optically thick across the entire thermal IR. If there is a surplus of outgoing radiation at the top of the model, adjusting the surface temperature to achieve flux balance is no longer effective because changes must diffuse through the atmosphere up to space over several iterations. In the meantime, the surface receives little feedback and makes further changes, resulting in stability issues. Since modeling these thick, warm, wet Martian climates is of general interest, the issue must be resolved. My solution is to reduce temperatures throughout the optically thick region of the atmosphere along with the surface temperature. First I locate the region between the surface and the altitude where the temperature drops below the planet's effective temperature T_{eff} . After the normal iteration technique to balance radiative flux and convection is applied, the layer in this region with the smallest ΔT value, ΔT_{min} , is identified. The temperatures of all layers in the region are then adjusted

$$T_{adj} = T_{norm} - \Delta T_{min} + \Delta T_S \quad (2.13)$$

where T_{adj} is the adjusted temperature, T_{norm} is the normal unadjusted temperature, and ΔT_S is the negative temperature change normally made at the surface. This technique ensures that the planet cools when there is a surplus of outgoing flux, but retains the relative

temperature changes between atmospheric layers in each iteration.

2.2 Photochemical Model

The photochemical model is constructed as a series of atmospheric layers co-located with those of the radiative-convective model. Photolysis rates are self-consistently derived from the UV/VIS flux profiles generated by the radiative-convective model, with quantum efficiencies taken from JPL Data Evaluation, No. 17 for Chemical Kinetics and Photochemistry (Sander et al. 2011). The Kinetic-PreProcessor (KPP) code is used to solve for photochemical equilibrium (Daescu et al. 2003; Damian et al. 2002; Sandu et al. 2003). KPP is a highly developed stiff differential equation solver which allows the photochemical model to calculate equilibrium concentrations in each layer despite a huge range in reaction rate timescales. For example, on modern Mars O₂ and CO have a photochemical lifetime of order 10 years, while O(¹D) has a lifetime of roughly 100 nanoseconds (or less).

2.2.1 Eddy Diffusion Profile

For the fully detailed model, transport between layers is treated by eddy diffusion

$$\Phi_i = -K n \frac{df_i}{dz} \quad (2.14)$$

where Φ_i is flux of species i at a layer interface, K is the eddy diffusion coefficient, n is the total number density of all atmospheric species, f_i is the mixing fraction of species i ,

and z is altitude. There is no standard method of prescribing the eddy diffusion coefficient profile $K(z)$ for a terrestrial planetary atmosphere with arbitrary characteristics. One general feature is that in the middle and upper atmosphere K is expected to scale approximately as $n^{-1/2}$ due to turbulence driven by the breaking of gravity waves (Lindzen 1981). This relationship does not hold in the troposphere, where convection dominates the production of turbulence. Nevertheless, based on the scaling concept, some studies of hypothetical terrestrial planet atmospheres use the eddy diffusion coefficient profile measured for Earth by Massie & Hunten (1981), and then scale the profile to obtain equivalent K at a given density or pressure level in the atmosphere (e.g. Johnson et al. 2009; Segura et al. 2007; Tian et al. 2010). In exploring a range of possible Martian atmospheres from 1–100 mbar, Zahnle et al. (2008) scaled against a K profile representative of modern Mars instead of Earth. In the simplest case, a constant value of K is assumed for the entire atmosphere and varied through a reasonable range to test sensitivity (Rosenqvist & Chassefière 1995). The reasons for this disparity of approaches are (1) the inherently approximate nature of eddy diffusion as a means of quantifying turbulence driven atmospheric mixing, and (2) the practical reality that estimating K to within an order of magnitude is sufficient for many photochemical applications.

In photochemical model developed here, the formulation $K = 2 \times 10^{13} n^{-1/2} \text{ cm}^2/\text{s}$ is used for the middle and upper atmosphere. This is consistent with values inferred from observations of that region on modern Mars (Krasnopolsky 1993), and also comparable to values measured for Venus (Bougher et al. 2008) and Earth (Massie & Hunten 1981). For the lower atmosphere, mixing length theory is employed to make a physically based

prediction of the tropospheric eddy diffusion coefficient. In mixing length theory, the eddy diffusion coefficient is set to $K = lw = \alpha Hw$, where l is the mixing length, taken to be the pressure scale height H multiplied by a dimensionless factor α , and w is the characteristic velocity of air parcels. For vertical mixing in the turbulent troposphere, this velocity arises from buoyancy-driven convection, and K may be written as (Satoh 2004, p. 378)

$$K = \alpha \frac{F_c}{\rho c_p \left(\Gamma_d + \frac{dT}{dz} \right)} \quad (2.15)$$

where F_c is the convective heat flux, ρ is the atmospheric density, c_p is its heat capacity, Γ_d is the dry adiabatic lapse rate, and $-dT/dz$ is the actual lapse rate. The factor α is retained to tune K based on observations of Earth. Following this methodology and inserting values appropriate for Earth near the surface ($F_c \approx 100 \text{ W/m}^2$, $\rho \approx 1 \text{ kg/m}^3$, $c_p \approx 1 \text{ kJ/kg/K}$, $dT/dz \approx -6 \text{ K/km}$, $\Gamma_d \approx 10 \text{ K/km}$), I find that $\alpha \approx 1/2$ reproduces the $K \approx 1 \times 10^5 \text{ cm}^2/\text{s}$ tropospheric value typically used by the terrestrial modeling community (Massie & Hunten 1981).

2.2.2 Photochemical Reactions

The network of atmospheric photochemical reactions considered in the fully detailed model generally follows previous work studying modern and ancient Mars (e.g. Krasnopolsky 2006; Nair et al. 1994; Rosenqvist & Chassefière 1995; Zahnle 2008). The reactions included are listed in Table 2.1. Convergence is achieved by either specifying

Reactants	Products	Rate Coefficient	Reference
$\text{CO}_2 + \text{h}\nu$	$\rightarrow \text{CO} + \text{O}$	J_1	[1]
$\text{CO}_2 + \text{h}\nu$	$\rightarrow \text{CO} + \text{O}(^1\text{D})$	J_2	[1]
$\text{O}_2 + \text{h}\nu$	$\rightarrow \text{O} + \text{O}$	J_3	[1]
$\text{O}_2 + \text{h}\nu$	$\rightarrow \text{O} + \text{O}(^1\text{D})$	J_4	[1]
$\text{O}_3 + \text{h}\nu$	$\rightarrow \text{O}_2 + \text{O}$	J_5	[1]
$\text{O}_3 + \text{h}\nu$	$\rightarrow \text{O}_2 + \text{O}(^1\text{D})$	J_6	[1]
$\text{H}_2\text{O} + \text{h}\nu$	$\rightarrow \text{OH} + \text{H}$	J_7	[1]
$\text{HO}_2 + \text{h}\nu$	$\rightarrow \text{OH} + \text{O}$	J_8	[1]
$\text{H}_2\text{O}_2 + \text{h}\nu$	$\rightarrow \text{OH} + \text{OH}$	J_9	[1]
$\text{O}(^1\text{D}) + \text{CO}_2$	$\rightarrow \text{CO}_2 + \text{O}$	$k_{10} = 7.5 \times 10^{-11} e^{115/T}$	[1]
$\text{O}(^1\text{D}) + \text{H}_2\text{O}$	$\rightarrow \text{HO} + \text{HO}$	$k_{11} = 1.63 \times 10^{-10} e^{60/T}$	[1]
$\text{O}(^1\text{D}) + \text{H}_2$	$\rightarrow \text{HO} + \text{H}$	$k_{12} = 1.2 \times 10^{-10}$	[1]
$\text{O} + \text{O}_3$	$\rightarrow \text{O}_2 + \text{O}_2$	$k_{13} = 8.0 \times 10^{-12} e^{-2060/T}$	[1]
$\text{O} + \text{OH}$	$\rightarrow \text{O}_2 + \text{O}_2$	$k_{14} = 1.8 \times 10^{-11} e^{180/T}$	[1]
$\text{O} + \text{HO}_2$	$\rightarrow \text{O}_2 + \text{OH}$	$k_{15} = 3.0 \times 10^{-11} e^{200/T}$	[1]
$\text{O} + \text{H}_2\text{O}_2$	$\rightarrow \text{OH} + \text{HO}_2$	$k_{16} = 1.4 \times 10^{-12} e^{-2000/T}$	[1]
$\text{O} + \text{H}_2$	$\rightarrow \text{OH} + \text{H}$	$k_{17} = 6.34 \times 10^{-12} e^{-4000/T}$	[2]
$\text{O}_2 + \text{HOCO}$	$\rightarrow \text{HO}_2 + \text{CO}_2$	$k_{18} = 2 \times 10^{-12}$	[1]
$\text{H} + \text{O}_3$	$\rightarrow \text{O}_2 + \text{OH}$	$k_{19} = 1.4 \times 10^{-10} e^{-470/T}$	[1]
$\text{H} + \text{HO}_2$	$\rightarrow \text{OH} + \text{OH}$	$k_{20} = 7.2 \times 10^{-11}$	[1]
$\text{H} + \text{HO}_2$	$\rightarrow \text{H}_2\text{O} + \text{O}(^1\text{D})$	$k_{21} = 1.6 \times 10^{-12}$	[1]
$\text{H} + \text{HO}_2$	$\rightarrow \text{H}_2 + \text{O}_2$	$k_{22} = 6.9 \times 10^{-12}$	[1]
$\text{H} + \text{H}_2\text{O}$	$\rightarrow \text{HO}_2 + \text{H}_2$	$k_{23} = 2.8 \times 10^{-12} e^{-1890/T}$	[2]
$\text{H} + \text{H}_2\text{O}_2$	$\rightarrow \text{OH} + \text{H}_2\text{O}$	$k_{24} = 1.7 \times 10^{-11} e^{-1800/T}$	[2]
$\text{OH} + \text{O}_3$	$\rightarrow \text{O}_2 + \text{HO}_2$	$k_{25} = 1.7 \times 10^{-12} e^{-940/T}$	[1]
$\text{OH} + \text{OH}$	$\rightarrow \text{H}_2\text{O} + \text{O}$	$k_{26} = 1.8 \times 10^{-12}$	[1]
$\text{OH} + \text{HO}_2$	$\rightarrow \text{H}_2\text{O} + \text{O}_2$	$k_{27} = 4.8 \times 10^{-11} e^{250/T}$	[1]
$\text{OH} + \text{H}_2\text{O}_2$	$\rightarrow \text{HO}_2 + \text{H}_2\text{O}$	$k_{28} = 1.8 \times 10^{-12}$	[1]
$\text{OH} + \text{H}_2$	$\rightarrow \text{H}_2\text{O} + \text{H}$	$k_{29} = 9.0 \times 10^{-13} e^{-1526/T}$	[3] (200-250 K)
		$k_{29} = 4.3 \times 10^{-13} (298/T)^{-2.4} e^{-1240/T}$	[3] (250-480 K)
$\text{HO}_2 + \text{O}_3$	$\rightarrow \text{O}_2 + \text{O}_2 + \text{OH}$	$k_{30} = 1.0 \times 10^{-14} e^{-490/T}$	[1]
$\text{HO}_2 + \text{HO}_2$	$\rightarrow \text{H}_2\text{O}_2 + \text{O}_2$	$k_{31} = 3.0 \times 10^{-13} e^{460/T}$	[1]
$\text{HO}_2 + \text{HO}_2 + \text{H}_2\text{O}$	$\rightarrow \text{H}_2\text{O}_2 + \text{O}_2 + \text{H}_2\text{O}$	$k_{32} = k_{31} \times 1.4 \times 10^{-21} e^{2200/T}$	[1]
$\text{HO}_2 + \text{HO}_2 + \text{M}$	$\rightarrow \text{H}_2\text{O}_2 + \text{O}_2 + \text{M}$	$k_{33} = 4.2 \times 10^{-33} e^{920/T} *$	[1]
$\text{HO}_2 + \text{HO}_2 + \text{H}_2\text{O} + \text{M}$	$\rightarrow \text{H}_2\text{O}_2 + \text{O}_2 + \text{H}_2\text{O} + \text{M}$	$k_{34} = k_{33} \times 1.4 \times 10^{-21} e^{2200/T}$	[1]

$O + O + M \rightarrow O_2 + M$	$k_{35} = 5.4 \times 10^{-33} (300/T)^{3.25} *$	[4]
$O + CO + M \rightarrow CO_2 + M$	$k_{36} = 2.2 \times 10^{-33} e^{-1780/T}$	[5]
$O + O_2 + M \rightarrow O_3 + M$	$k_{37} = 1.5 \times 10^{-33} (300/T)^{2.4} *$	[1]
$H + O_2 + M \rightarrow HO_2 + M$	$k_{38} = 8.8 \times 10^{-32} (300/T)^{1.3} *$	[1] Low P
	$k_{38} = 7.5 \times 10^{-11} (300/T)^{-0.2}$	[1] High P
$H + H + M \rightarrow H_2 + M$	$k_{39} = 1.6 \times 10^{-32} (298/T)^{2.27}$	[6]
$H + OH + M \rightarrow H_2O + M$	$k_{40} = 1.3 \times 10^{-30} (300/T)^2 *$	[2]
$OH + CO + M \rightarrow H + CO_2 + M$	$k_{41} = 1.5 \times 10^{-13} (300/T)^{-0.6}$	[1] †
	$2.1 \times 10^9 (300/T)^{-6.1}$	[1] †
$OH + CO + M \rightarrow HOCO + M$	$k_{42} = 1.2 \times 10^{-32} (300/T)^{1.4} *$	[1] Low P
	$1.1 \times 10^{-12} (300/T)^{-1.3}$	[1] High P
$OH + OH + M \rightarrow H_2O_2 + M$	$k_{43} = 9.0 \times 10^{-31} (300/T) *$	[1] Low P
	2.6×10^{-11}	[1] High P

Table 2.1: List of photochemical reactions considered in the full model.

References: [1] (Sander et al. 2011), [2] (Baulch et al. 2005), [3] (Orkin et al. 2006), [4] (Smith & Robertson 2008), [5] (Inn 1974), [6] (Walkauskas & Kaufman 1975)

* Indicates enhancement factor has been applied for $M = CO_2$. See text.

† Special case. See (Sander et al. 2011).

the concentration of a long lived, well mixed species (e.g. O_2 , H_2) or specifying a flux at the top and/or bottom boundaries of the atmosphere (Krasnopolsky 1995). Whichever variable is specified, the other is solved for during convergence.

The simplified photochemical model is used to provide a first order analysis of O_3 feedback processes in a more computationally timely manner. It is identical to the full model, except that all reactions involving HO_x are neglected and the concentrations of O_2 and CO are fixed at a 1:1 ratio for a prescribed mixing fraction. This ratio is chosen as a middle ground between the roughly 1:2 ratio in the current Martian atmosphere and the

2:1 stoichiometric ratio expected for a completely dry CO₂ atmosphere. In addition, eddy diffusion transport is neglected for the trace photochemical species (O(¹D), O, O₃). While not strictly accurate, this model converges to photochemical equilibrium very rapidly, allowing a broad range of atmospheres with varying pressure, insolation, and oxidation to be explored. This is a useful approach, given the great uncertainty in the exact set of atmospheric conditions Mars has experienced in the past. The simple model is validated as an acceptable first order approximation against the full photochemical model in Chapter 3.

In the simple photochemical model, the mixing fraction of H₂O is given a simple “step” profile, being held constant from the surface up to the condensation altitude, at which point its vapor pressure curve is followed up to the cold trap based on the temperature profile. Above this the mixing fraction is again assumed to be constant. This is a typical practice when modeling modern Mars (Nair et al. 1994). In the full model, which implements eddy diffusion, H₂O is allowed to diffuse from the surface up to the condensation level, which is determined by the enforcement of flux continuity. Above the cold trap H₂O is given a constant mixing fraction, as in the simple model. A fairly dry surface relative humidity of RH=20% is used for all the results given here, comparable to modern Mars (Zahnle et al. 2008).

For most reaction kinetics I utilize the most recent JPL evaluation, No. 17 (Sander et al. 2011), with supplementation by the evaluation of Baulch et al. (2005). However, a thorough review of the literature was performed, and a few reaction rates have been taken from individual studies in cases where the work is more recent or better suited to the

Martian atmosphere than the evaluated rates of Sander et al. (2011) and Baulch et al. (2005).

For example, the atmospheric community has long used the results of Campbell & Gray (1973) to calculate the rate of k_{35} as function of temperature. However, experiments by Smith & Robertson (2008) have recently produced a more accurate parameterization with significantly higher rates at low temperatures (< 200 K). This is an important reaction for this work, since k_{35} is the primary O_2 production mechanism when there is little HO_x present (Nair et al. 1994; Rosenqvist & Chassefière 1995).

Computational quantum chemistry work by Mousavipour & Saheb (2007) has proven that excited $O(^1D)$, not the ground state $O(^3P)$, is the primary O product in reaction k_{21} . This work appears to have been overlooked by the atmospheric modeling community. While the modification is of some academic interest, as it is the only non-photolysis path by which $O(^1D)$ is created in the atmospheric model, in practice it does not significantly affect the results presented here. However, it might be important for the $O(^1D)$ photochemistry of terrestrial planets with relatively humid stratospheres, such as during a runaway greenhouse on Venus or an exoplanet.

The temperature dependence of most two-body reaction rates are well represented by an Arrhenius parameterization. An exception here is reaction k_{29} , which is a major chemical destruction path for H_2 . The experimental fit of Orkin et al. (2006) is used, and separate parameterizations are employed above and below 250 K.

In the three-body reaction rates used in this work, an effort has been made to apply parameterizations intended for use with CO_2 as the third body. However,

experimental data for these conditions are sparse, and the only reactions for which reliable temperature dependent fits could be found were k_{36} (Inn 1974) and k_{39} (Walkauskas & Kaufman 1975). Thus, for all other cases, I resort to the common practice of modifying rates intended for N_2 by an enhancement factor to account for the greater efficiency of CO_2 in three-body reactions. Many studies follow the practice of Nair et al. (1994), who used a factor of 2.5 derived from the well studied k_{37} reaction and applied it to all three-body reactions. I have made an effort to identify individual enhancement factors for each reaction based on the fixed temperature measurements available in the literature. For k_{35} an enhancement factor of 1.8 from Jamieson et al. (2009) is used, for k_{40} a factor of 1.9 is used based on the work of Zellner et al. (1977), and for k_{43} a factor of 1.3 is used based on the work of Black & Porter (1962) and Caldwell & Back (1965). All of these studies were carried out at room temperature. The only three-body reactions for which appropriate experimental enhancement factors could not be determined were k_{33} , k_{38} , and k_{42} . Based on the enhancement factors for which there is available data, I have opted to simply apply a generic factor of 2 to these reaction rates.

The hydrogen bearing organic species HCO and H_2CO are neglected here, which is justified considering the results of previous studies and the inherently oxidizing conditions I examine. Zahnle et al. (2008) examined the possibility that these species could be involved in a H_2 production pathway on Mars both past and present. They found that kinetics from the literature which reproduced an H_2 concentration consistent with observations of modern Mars made this mechanism generally unimportant. Liang et al. (2006) examined the effect of H_2CO surface deposition and burial on the H_2 budget for a

cold “Snowball Earth” climate with volcanism. However, even under the reducing conditions generated by the volcanic source, only low concentrations of H_2CO (< 1 ppt) were produced. The oxidizing conditions examined here make such compounds even less stable and thus insignificant for photochemistry.

Reactions involving N bearing compounds are also neglected. This deserves remark, since N_2 is the second most abundant gas in the modern Martian atmosphere (2.7% mixing fraction). The primary reason for neglecting N photochemistry is its relative unimportance in the Martian atmosphere. According to the calculations of Stock et al. (2012), catalytic pathways involving NO_x (NO , NO_2) account for only 10% of the CO_2 recombination on modern Mars, with all other pathways being mediated by HO_x species. This makes the contribution of N compounds comparable to the uncertainty of the HO_x reaction rates. Zahnle et al. (2008) also found that N compounds played at most a minor role in their study of Martian photochemistry for atmospheres in the range of 1–100 mbar. A secondary reason for neglecting N chemistry is that conditions of past Martian atmospheres are not sufficiently well known to allow for an accurate treatment. While an N_2 mixing fraction similar to modern Mars might be inferred from the atmosphere of Venus and cometary ices, conditions on Mars both past and present are highly favorable for the sequestration of N as nitrate minerals in the subsurface (Segura & Navarro-González 2005; Sutter et al. 2007). Thus, the initial atmospheric N_2 reservoir may have been largely removed over the first few hundred Myrs of the planet's history. In addition, the rate of NO_x formation by volcanism and lightning on early Mars may only be estimated to zeroth order at best (Segura & Navarro-González 2005). The final reason

for neglecting N compounds is the utility of studying the photochemistry of a pure CO₂-H₂O atmosphere as a baseline scenario. The effects of N photochemistry may always be included in future modeling to better understand their significance and impact.

2.3 Summary

A coupled climate-photochemistry model has been developed to study the potential for significant O₃ feedback on the ancient Martian climate. The climate portion consists of a radiative-convective model applying detailed LBL calculations and a two-stream radiative transfer method to balance the energy budget and solve for the equilibrium temperature profile. While a LBL treatment is computationally intensive, the calculations have been optimized to allow for practical use (convergence times on the order of minutes to an hour). The full photochemical model has been constructed after a thorough review of the literature concerning eddy diffusion profiles and reaction rates, and contains numerous modest improvements over previous work. A simpler photochemical model is also defined, which, while not strictly accurate, allows for more rapid convergence with the climate model while maintaining first order accuracy for O₃ layer characteristics and feedback processes. The climate and photochemical models are coupled by self-consistent temperature, pressure, and radiation flux profiles, and executed in turn to progress the entire system toward equilibrium.

3. Parameter Space Results

In this Chapter I explore the most favorable, but still plausible, conditions under which an O₃ layer might form on Mars. Validation of the climate model, the full photochemical model, and the simple photochemical model is provided. The parameter space of pressure P and insolation S is evaluated using the climate model alone to identify what range of these variables are most conducive for oxidizing conditions. Based on these results, the P range of interest is narrowed and the parameter space extended to include the O₂ mixing fraction f_{O_2} . The photochemical feedback of O₃ is then explored by coupling my simple photochemical model to my climate model.

3.1 Model Validation

As a validation of the radiative-convective model some test runs were performed without photochemistry to compare with the results of selected models in the literature. Under modern insolation a surface temperature of 273 K is achieved for a surface pressure of 2.5 bar, somewhat higher than the 2.2 bar reported by Pollack et al. (1987). This difference may be explained by the inclusion of CO₂ condensation (Kasting 1991) and differing treatment of CIA parameterization (Wordsworth et al. 2010a). The differences in H₂O profile structure and surface albedo between the two models also have minor influences. To compare with the model of Wordsworth et al. (2010a), the insolation is scaled by a factor of 0.75 at all wavelengths to approximate early solar conditions and H₂O is removed from the atmosphere. Under these conditions a peak surface temperature

of 215 K is found at a surface pressure of ~ 1 bar, and condensation of the atmosphere at the surface occurs near a temperature of 208 K and pressure of just over 2.7 bar. These results are in good agreement with those of Wordsworth et al. (2010a) for their “GBB” CIA parameterization (Baranov et al. 2004; Gruszka & Borysow 1998) with sub-Lorentzian wings for CO₂ lines. This is encouraging, as this model is the most similar to the one presented here in the calculation of radiative cross-sections. Like the results of Wordsworth et al. (2010a), our detailed clear-sky radiative-convective model produces temperatures significantly lower than those used in previous studies modeling thick atmospheres (e.g. Tian et al. 2010).

The full photochemical model was validated by assuming a modern Mars configuration and comparing with observation and previous modeling. Because the current form of the radiative-convective model does not have dust implemented, it cannot accurately predict the temperature profile of modern Mars. For this reason, the fixed temperature profile used by Zahnle et al. (2008) is applied, which has a surface temperature of 211 K and a lapse rate of 1.4 K/km up to an isothermal stratosphere at 50 km. In the troposphere the eddy diffusion coefficient K is set to be 10^6 cm²/s. Surface pressure is taken to be 6.3 mbar and the relative humidity at the surface is tuned to reproduce the observed precipitable H₂O column of ~ 10 micron. The O₂ mixing fraction is fixed at the observed value of 1.3×10^{-3} and all other variables are solved for photochemical equilibrium. Overall, the results are similar to previous work (e.g. Krasnopolsky 2003; Nair et al. 1994; Zahnle et al. 2008). The equilibrium content of H₂ is 10 ppm, somewhat lower than that found by other modelers, but still consistent with

the 15 ± 5 ppm observation of Krasnopolsky & Feldman (2001). A surface mixing fraction of 13 ppb H_2O_2 and an O_3 column of $2.6 \times 10^{15} \text{ cm}^{-2}$ are produced, also consistent with previous modeling and observation (Encrenaz et al. 2011; Lefèvre et al. 2004). The CO mixing fraction of 1.8×10^{-4} is significantly below the observed value of 7×10^{-4} , however this is a longstanding unresolved issue with photochemical models of the Martian atmosphere (Krasnopolsky 2003). A plot of the vertical profiles for some of the photochemically produced species is given in Fig. 3.1. Note how the O_3 mixing fraction declines below 50 km due to the increased amount of HO_x , primarily in the form of HO_2 .

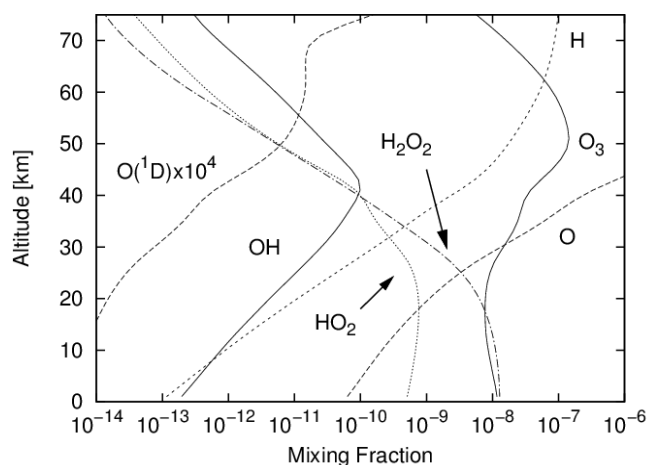


Figure 3.1: Photochemical species' abundance profiles calculated for the current Martian atmosphere.

To validate the simple version of the photochemical model for the examination of O_3 climate feedback in thick atmospheres, a number of tests were performed. The sensitivity of the model to the assumed 1:1 ratio for $\text{CO}:\text{O}_2$ is not large, with an order of magnitude change typically altering the O_3 column by only $\sim 30\%$. Likewise, the results

are not highly dependent on the assumption of a well-mixed CO profile, however they do require that O₂ be well-mixed. Under paleo-Earth conditions, the profiles of O₂ and CO deviate from being well-mixed for fractions < 10⁻⁴ due to vigorous destruction by HO_x in the troposphere. However, the production of HO_x in the thick Martian atmospheres considered here is several orders of magnitude lower than on paleo-Earth, so this threshold is reduced. To examine this, a full photochemical calculation including HO_x destruction in a 0.3 bar atmosphere with O₂ and CO at a 10⁻⁵ mixing fraction under modern insolation was performed. Atmospheric lifetimes on the order of years were determined, which is comparable to modern Mars and consistent with the assumption of these species being well mixed.

In the simplified version of my photochemical model the effects of HO_x chemistry and atmospheric transport on the O₃ profile have consciously been omitted. These effects are especially important in the upper troposphere, where the radiative forcing of O₃ is most sensitive to its concentration (Forster & Shine 1997) and heating of the cold trap can influence stratospheric photochemistry. The simple model is expected to overestimate the stratospheric O₃ concentration due to neglecting catalytic destruction by HO_x and downward transport to the troposphere. Conversely, it underestimates the tropospheric O₃ concentration because of the neglect of downward transport from the stratosphere, though this would be partially counteracted by HO_x reactions. In terms of climate forcing, this means that cooling by stratospheric O₃ is too large and warming by tropospheric O₃ too low. This suggests that the simple model *underestimates* the climate warming effect of O₃, making the results conservative in their bias.

In the results presented here, the peak O₃ concentration is always above the tropopause. The location of this peak is determined by where the overhead column of O₃ absorbs most of the UV capable of splitting CO₂ and O₂ to O, thus cutting off the means of O₃ production (Chapman 1930). Including catalytic HO_x destruction reduces the O₃ column at a given altitude in the stratosphere, in turn lowering the altitude of peak O₃ concentration. This descent of the O₃ layer into the upper troposphere would strengthen some of the feedback effects examined in this study, such as inhibition of CO₂ condensation and alteration of the dominant H₂O dissociation pathway. Including convective transport of O₃ from the stratosphere to the troposphere would have similar effects.

To quantify the importance of these effects, a comparison between the simple and full photochemical models was performed for a 1 bar atmosphere under modern insolation with an O₂ mixing fraction of 10⁻³. The temperature profile was converged using the simple model and then left fixed for the run with the full model. In the troposphere the O₃ mixing ratio became well-mixed at ~10 ppb in the full model, significantly higher than that found with the simple model, and in fact similar to Earth. Sensitivity tests with the climate model indicate that tropospheric O₃ must be > 10 ppb to significantly affect the Martian energy budget. In the full photochemical model stratospheric O₃ concentrations were reduced by a factor of 2 relative to the simple model, as was the overall column. This decline would be somewhat less if the temperature profile were to be converged with the full photochemistry model, as the stratosphere would be dehumidified. The altitude of the peak stratospheric O₃

concentration was also lowered by 8 km, but remained well above the tropopause. This demonstrates that the primary results of this chapter using the simple photochemical model are valid as a first order approximation, and that the foregoing qualitative analysis regarding the effects of neglecting HO_x reactions and O₃ transport is sound.

3.2 Climate Parameter Space

To guide the search for atmospheres that would have been most conducive to the formation of O₃, I first use the radiative-convective model with no photochemistry to explore the parameter space of surface pressure P and insolation S , where S is the insolation as a fraction of modern intensity. A plot of the resulting surface temperature is shown in Fig. 3.2a, with the diamond symbols identifying for each value of S at what surface pressure CO₂ condensation begins in the middle atmosphere. Unlike the model of Kasting (1991), which produced CO₂ condensation at modern insolation levels for $P \geq 0.35$ bar, this model (without photochemistry) does not condense until $P \geq 0.92$ bar. The discrepancy is likely due to the differing treatment of NIR solar absorption between the models, with the present model having greater stratospheric heating (J. F. Kasting & R. Ramirez, pers. comm., 2011). It is worth noting that both models calculate a globally averaged temperature profile and assume radiative-convective equilibrium. CO₂ condensation could still occur for $P < 0.92$ bar, as it does on Mars today, in cold regions at high latitude (Kelly et al. 2006) and in the mesosphere due to temperature fluctuations driven by atmospheric waves (Montmessin et al. 2006).

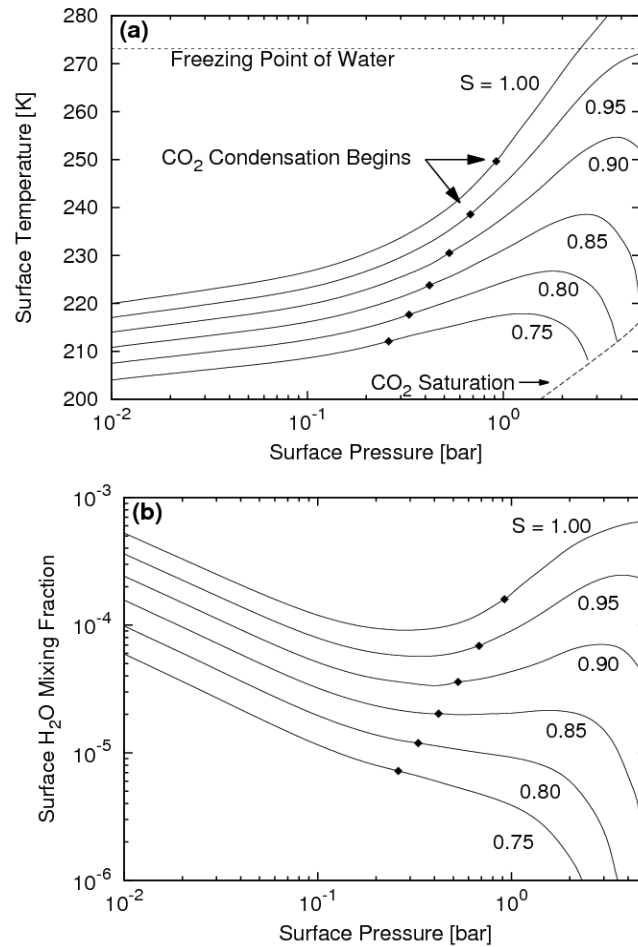


Figure 3.2: Parameter space showing (a) surface temperature and (b) surface H₂O mixing ratio as a function of surface pressure P and insolation S (for modern Sun intensity $S = 1.00$). For each S track the pressure above which CO₂ condensation begins in the middle atmosphere is indicated by \blacklozenge .

Surface H₂O mixing fraction f_{H_2O} is shown in Fig. 3.2b as a function of P and S . It is seen that for $S > 0.85$ there exists a local minimum for f_{H_2O} . The reason for this minimum is as follows: For $P < 0.3$ bar the surface temperature increases only weakly

with pressure, causing the vapor pressure of H₂O to rise less quickly than the CO₂ pressure and resulting in the decline of f_{H_2O} . At $P > 0.3$ bar H₂O becomes an important greenhouse gas for these atmospheres and its positive feedback on temperature is strong enough to increase f_{H_2O} with increasing surface pressure. For $S < 0.85$ the surface temperature never rises enough for H₂O to become a significant greenhouse gas, and so its mixing fraction decreases monotonically with P .

For the purpose of identifying conditions likely to support a thick O₃ layer, it is of interest to summarize here some of the results of Rosenqvist & Chassefière (1995). Modeling a CO₂-H₂O atmosphere with a fixed temperature profile and varying pressure, they identified three distinct photochemical regimes for the O₂ mixing fraction f_{O_2} , which may be compared with those for f_{H_2O} outlined above. For $P < 0.1$ bar f_{O_2} declined with P , while for $0.1 < P < 1$ bar it rose with P , and finally declined again at $P > 1$ bar. The cause of rising f_{O_2} for $0.1 \text{ bar} < P < 1 \text{ bar}$ was determined to be increased shielding of H₂O against photolysis, resulting in decreased destruction of O₂ by HO_x. By $P \sim 1$ bar this caused the atmospheric photochemistry to be insensitive to H₂O content. For $P < 1$ bar they found that artificially reducing f_{H_2O} (making the atmosphere drier) also reduced HO_x and produced a higher f_{O_2} .

Taking the results presented above concerning pressure and temperature with no photochemistry along with those of Rosenqvist & Chassefière (1995) concerning pressure at fixed temperature, it would seem that conditions favorable to O₃ formation are most likely to be found at moderate pressures of 0.3–1.0 bar. The lower end of this range corresponds with my finding of a minimum mixing fraction of tropospheric H₂O for

pressures ≥ 0.3 bar, while the upper end is determined by the finding of Rosenqvist & Chassefière (1995) that tropospheric H₂O is increasingly shielded as pressures approach 1 bar. Thus, within this range a minimum of H₂O photolysis is expected, with a corresponding maximum in accumulation of oxidizing species like O₂ and O₃.

In a broader context, focusing on atmospheric pressures of 0.3–1.0 bar is consistent with recent work suggesting that Mars had an atmosphere ≥ 0.2 bar at some time in its past (Manga et al. 2012), but has volcanically outgassed ≤ 1 bar CO₂ over its history (Grott et al. 2011). It is also notable that this range falls within the 0.1–1 bar “dead zone” in Mars' history identified by Richardson & Mischna (2005). That study pointed out that within this range of pressures diurnal temperature highs would rarely reach the freezing point of water. Subsequently, loss of CO₂ by surface weathering would be limited, reducing its utility for explaining the modern observed pressure of 6 mbar. For climates in this “dead zone” it is expected that feedback from O₃ would be relatively strong. If a significant positive effect on surface temperature exists, warming by O₃ might have helped stabilize ephemeral liquid water, facilitating continued weathering out of CO₂. This possibility is considered when investigating the effect of O₃ on the energy budget in the next section.

3.3 Photochemistry Parameter Space

To explore the feedback processes of O₃, the climate model is next coupled to the simple photochemical model. Based on the results of the previous section, and in order to more directly compare with previous work by Selsis et al. (2002), a nominal atmospheric

model is selected with a surface pressure $P = 1$ bar, a modern insolation intensity $S = 1.00$, and an O_2 mixing fraction $f_{O_2} = 10^{-3}$. These parameters are then varied in turn to characterize their effect on the O_3 layer and its feedbacks. The ranges of $P = 0.3\text{--}1.0$, $S = 0.75\text{--}1.00$, and $f_{O_2} = 10^{-5}\text{--}10^{-2}$ are examined. The range for f_{O_2} is based on the $CO_2\text{-}H_2O$ photochemical modeling results of Rosenqvist & Chassefière (1995), which is appropriate for the assumption of negligible volcanic outgassing and surface weathering (Kasting 1995). This range is also similar to that covered in the work of Kasting & Donahue (1980), which quantified the impact of an O_3 layer on ancient Earth. Note that not all atmospheres within the explored parameter space are necessarily self-consistent or realistic. For example, it is quite certain that Mars has not had an atmosphere of order 1 bar during the past billion years when $S \sim 1$. The purpose of this study is to identify the important effects and feedback mechanisms (if any) of plausible thick Martian O_3 layers and to characterize them. A parameter space investigation fulfills this goal by allowing independent tuning of a number of variables. This provides a foundation of understanding upon which to build future work involving more a detailed and self-consistent treatment of photochemistry.

3.3.1 O_3 Profile and Column

I begin the characterization of potential Martian O_3 layers by examining their concentration profiles and integrated column densities. Varying f_{O_2} , it is found that with more O_2 the O_3 layer becomes thicker and its peak value larger and located at higher altitude (Fig. 3.3). This same behavior has been found by models examining the

photochemistry of early Earth (Kasting & Donahue 1980), and it is due to the increased availability of O_2 for O_3 production and decreased penetration of UV. In contrast, it is found that varying P and S have little or no effect on the profile when altitude is plotted as pressure. Given these findings, I will focus in this section on the impact of f_{O_2} on the

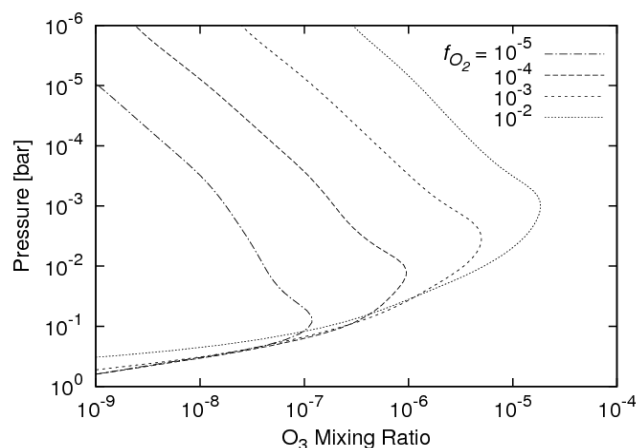


Figure 3.3: O_3 profiles for various f_{O_2} in a 1 bar atmosphere with modern insolation.

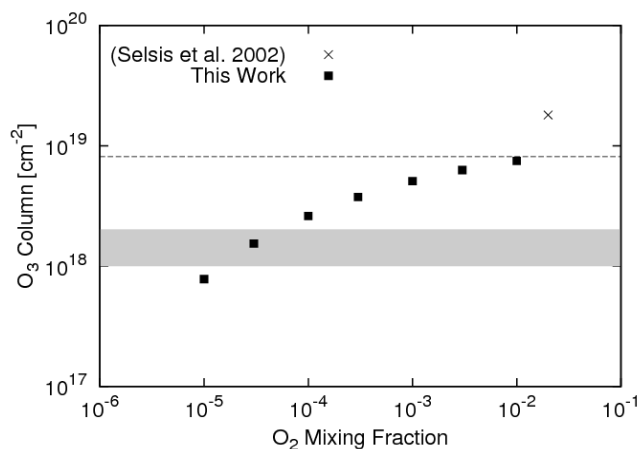


Figure 3.4: O_3 column as a function of f_{O_2} . The dashed line is a typical column on modern Earth ($8.1 \times 10^{18} \text{ cm}^{-2}$), and the shaded region estimates the column necessary to protect bacteria from UV radiation (François & Gérard 1988).

O₃ profile.

While increasing f_{O_2} generally increases the O₃ column (Fig. 3.4), it eventually levels off at a value comparable to that of modern Earth (300 Dobson units $\approx 8.1 \times 10^{18}$ cm⁻²). Again, this is in line with models of the early Earth (Kasting & Donahue 1980). An O₃ column of 7.5×10^{18} cm⁻² is obtained for our most oxidizing atmosphere with $f_{O_2} = 1 \times 10^{-2}$. This is less than half of the 1.8×10^{19} cm⁻² column of the “*super ozone layer*” reported by Selsis et al. (2002) for a 1 bar Martian atmosphere with $f_{O_2} = 2 \times 10^{-2}$. While the results here are not directly comparable with those of Selsis et al. (2002) due to the different f_{O_2} , as previously mentioned it is expected that the O₃ column would be little different for higher f_{O_2} . Curiously, since the model of Selsis et al. (2002) has a lower CO mixing ratio and contains catalytic HO_x destruction of O₃ while the current model does not, it is expected that their model would produce a smaller column smaller, not larger. Furthermore, both models contain the majority of their O₃ in the stratosphere, so the detailed tropospheric photochemistry implemented in Selsis et al. (2002) cannot be the cause of disagreement. It was considered that the difference might be due to the diurnal averaging of solar flux for photochemistry (Krasnopolsky 2006), but a test run of my model using average daytime insolation increases the O₃ column by only 10%. The model's insensitivity to solar flux also rules out the disagreement being caused simply by a differing choice in solar zenith angle (Kasting & Donahue 1980). I conclude that the discrepancy most likely comes about because the result in Selsis et al. (2002) is not a converged solution, and should only be considered as an upper limit. The results of the simple converged model presented here thus provide a tighter constraint on the maximum

stratospheric O₃ column in a thick Martian atmosphere, limiting it to very nearly the same value as on Earth.

In the interest of assessing the potential habitability of these Martian atmospheres for primitive life, an estimate for the minimum O₃ column necessary to ensure bacterial survival from UV damage is included in Fig. 3.4. I follow Hiscox & Lindner (1997) in taking the minimum tolerable O₃ column range determined for Earth by François & Gérard (1988) and scaling it to account for the lower UV flux at Martian orbit. It is found that, under this globally averaged, clear sky, 1 bar CO₂ atmosphere with modern insolation, obtaining surface UV conditions capable of allowing bacterial survival requires $f_{O_2} > 10^{-5}$. Including clouds and dust in the atmosphere would further reduce the UV flux at the surface. It should also be noted that in the early solar system, the UV flux from the young Sun was generally less than that of the modern Sun at $\lambda > 200$ nm and greater at $\lambda < 200$ nm (Ribas et al. 2010). Since CO₂ absorbs virtually all radiation at $\lambda < 200$ nm regardless of O₂ and O₃ column, the use of a modern solar spectrum by François & Gérard (1988) somewhat overestimates the minimum O₃ column required to support primitive surface life on Mars under the young Sun.

3.3.2 Energy Budget

While temperatures in the middle atmosphere strongly increase with more O₂ due to increased solar absorption by the O₃ layer, the surface temperature is not greatly affected (Fig. 3.5). Testing with the removal of the O₃ IR bands resulted in a surface temperature drop of at most ~ 1 K, indicating that the contribution of O₃ to the

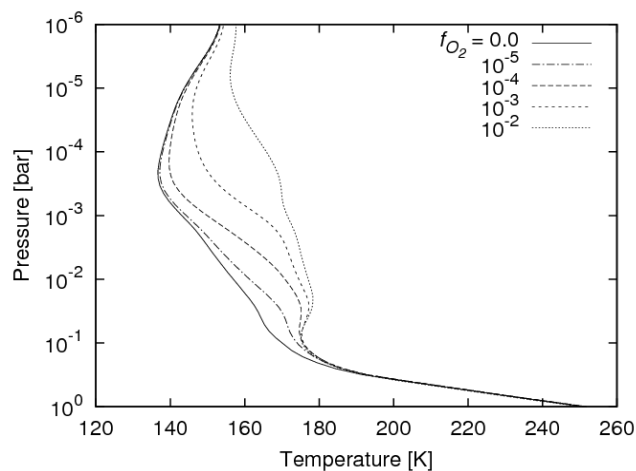


Figure 3.5: Temperature profile for various f_{O_2} in a 1 bar atmosphere under modern insolation.

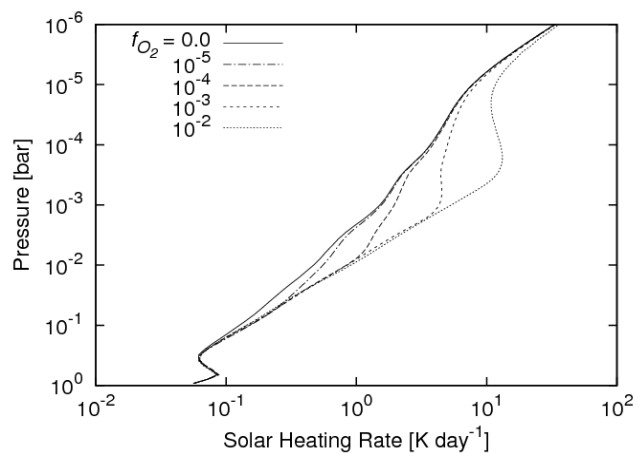


Figure 3.6: Solar heating profile for various f_{O_2} in a 1 bar atmosphere under modern insolation.

greenhouse effect in these models is insignificant. Solar absorption by thin O_3 layers primarily cause heating just above the tropopause, and the altitude and magnitude of peak solar heating by O_3 rises with increasing O_2 (Fig. 3.6). The majority of this heating is due to absorption in the UV/VIS wavelengths, as on Earth, and occurs above the 0.1 bar

pressure level in the atmosphere where Rayleigh scattering becomes important. As a result, the planetary bond albedo is significantly reduced, with a decrease of 8.1% at $f_{O_2} = 10^{-2}$ relative to an atmosphere without an O_3 layer. This corresponds to a 3.8% increase in solar energy absorbed by the planet. The portion of this energy injected into the upper troposphere suppresses the thermal convective flux, resulting in a small warming effect at the surface. However, for thick O_3 layers this is counteracted by an overall reduction in the amount of solar radiation reaching the surface, as the majority of the O_3 absorption occurs high in the atmosphere and is simply re-radiated to space thermally. A listing of convective, longwave, and shortwave fluxes at the surface and top of the atmosphere for various values of f_{O_2} are given in Table 3.1.

f_{O_2}	$\Delta F_{\uparrow, surf}^C$	$\Delta F_{\downarrow, surf}^L$	$\Delta F_{\downarrow, surf}^S$	$\Delta F_{\uparrow, top}^S$
10^{-5}	-0.3 (-0.6%)	+2.2 (+1.1%)	-0.6 (-0.6%)	-1.4 (-2.9%)
10^{-4}	-0.6 (-1.2%)	+2.7 (+1.4%)	-1.3 (-1.3%)	-2.4 (-5.1%)
10^{-3}	-1.6 (-3.2%)	-0.4 (-0.2%)	-1.9 (-2.0%)	-3.2 (-6.8%)
10^{-2}	-2.3 (-4.8%)	-3.7 (-1.9%)	-2.4 (-2.5%)	-3.8 (-8.1%)

Table 3.1: Effect of varying f_{O_2} on O_3 energy budget forcing for $P = 1$ bar, $S = 1.00$. Each ΔF is taken with respect to the atmosphere with $f_{O_2} = 0$ and as has units of W/m^2 . Superscripts C = convective, L = longwave, and S = shortwave.

Holding $f_{O_2} = 10^{-3}$ and lowering S below 1.00 enhances the suppression of convection and alters the change in downward surface IR flux from a slight decrease to an increase (Table 3.2). In contrast, approximately constant relative reductions in the

amount of solar radiation reaching the surface and reflecting to space are maintained, so the net effect of reducing S is to enhance the relative surface warming effect of O_3 . This suggests O_3 could act to buffer surface temperature against reductions in solar flux, although the effect is very weak for the atmosphere considered here.

S	$\Delta F_{\uparrow, surf}^C$	$\Delta F_{\downarrow, surf}^L$	$\Delta F_{\downarrow, surf}^S$	$\Delta F_{\uparrow, top}^S$
1.00	-1.6 (-3.2%)	-0.4 (-0.2%)	-1.9 (-2.0%)	-3.2 (-6.8%)
0.95	-1.4 (-3.3%)	+0.8 (+0.5%)	-1.9 (-2.0%)	-3.1 (-6.9%)
0.90	-1.3 (-3.5%)	+2.1 (+1.5%)	-1.9 (-2.1%)	-3.0 (-7.0%)
0.85	-1.2 (-3.8%)	+2.6 (+2.1%)	-1.9 (-2.1%)	-2.8 (-7.1%)
0.80	-1.2 (-4.8%)	+2.3 (+2.2%)	-1.7 (-2.1%)	-2.7 (-7.1%)
0.75	-1.3 (-6.2%)	+2.0 (+2.4%)	-1.6 (-2.1%)	-2.6 (-7.2%)

Table 3.2: Effect of varying S on O_3 energy budget forcing for $P = 1$ bar, $f_{O_2} = 10^{-3}$. Each ΔF is taken with respect to the atmosphere with $f_{O_2} = 0$ and as has units of W/m^2 . Superscripts are the same as in Table 3.2.

I also examined the effect of O_3 heating on CO_2 condensation in the middle atmosphere. Fig. 3.7 shows that while a 1 bar atmosphere with $f_{O_2} = 0$ at $S = 1.00$ condenses near the 0.1 bar level, an atmosphere with $f_{O_2} = 10^{-3}$ does *not* due to heating by O_3 . And though CO_2 condensation is not completely suppressed at very low insolation ($S = 0.75$), it does continue to be inhibited at altitudes above the 0.1 bar level. This finding likely has ramifications for the ability of CO_2 clouds to warm the surface through scattering of IR (Forget & Pierrehumbert 1997; Mischna et al. 2000), though accurately quantifying the effect would require detailed microphysical modeling (Colaprete & Toon

2003).

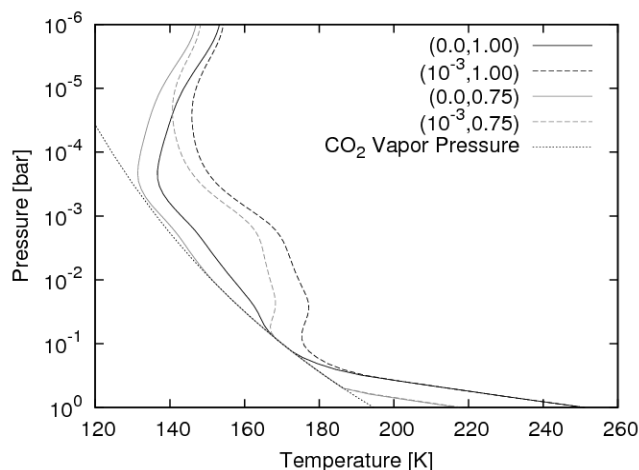


Figure 3.7: Temperature profiles for $f_{O_2} = 0$ and 1×10^{-3} in a 1 bar atmosphere with $S = 1.00$ and 0.75 . Line titles are in the format (f_{O_2}, S) .

3.3.3 H_2O Dissociation

The effect of O_3 on the column integrated H_2O dissociation rate is important because it plays a role in both the atmosphere's photochemistry and its loss over time. In general, the greater the amount of dissociation, the more the atmosphere will be dominated by the chemistry of HO_x products and the more H_2 will be produced. Increasing the concentration of H_2 in the atmosphere directly increases its loss rate to space and thus the loss rate of H_2O from Mars, regardless of whether loss of H_2 is limited by the escape rate of H or diffusion of H_2 at the homopause (R.E. Johnson et al. 2008; Zahnle et al. 2008). The concentration of H_2 in the upper atmosphere can also indirectly

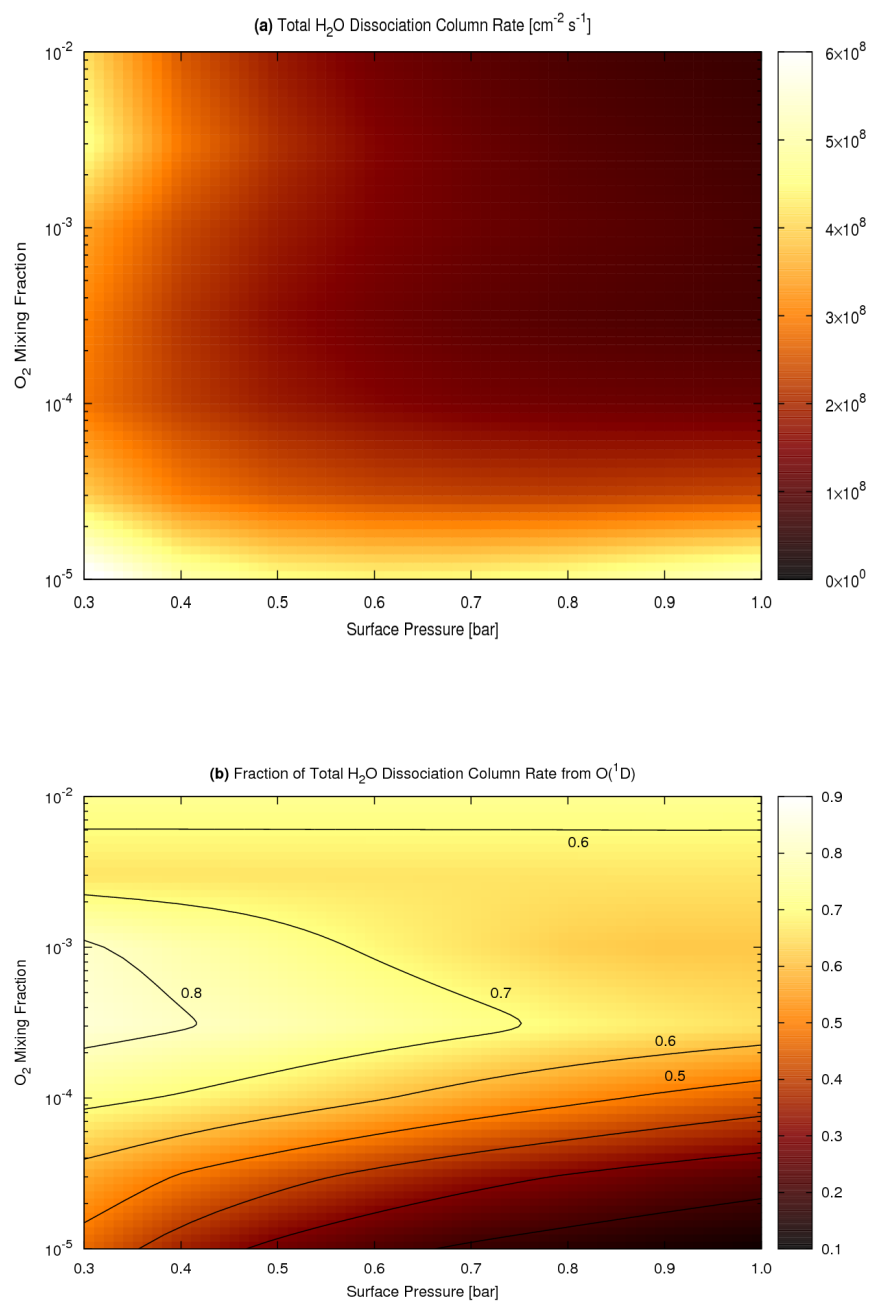


Figure 3.8: Characterization of H_2O dissociation as a function of f_{O_2} and P : (a) total column integrated dissociation rate (photolysis + $O(^1D)$ attack) and (b) fraction of dissociation attributable to $O(^1D)$ attack.

affect the loss of other species by shielding them from the EUV which powers their non-thermal escape mechanisms (Fox 2003).

As seen in Table 2.1, the two pathways by which H₂O is dissociated are direct photolysis by UV and attack by O(¹D). The vast majority of O(¹D) in the modeled atmospheres was produced by photolysis of O₃ (J_6). Fig. 3.8 maps the total column integrated H₂O dissociation rate and the fraction dissociated by O(¹D) in the parameter space of P and f_{O_2} . In low pressure atmospheres the column integrated O(¹D) attack rate is large because the low altitude O₃ layer produces abundant O(¹D) near the H₂O rich upper troposphere. However, for high pressure atmospheres the O₃ layer is raised up into the H₂O poor stratosphere, reducing the contribution of O(¹D) attack to H₂O dissociation. For $f_{O_2} \sim 10^{-5}$ – 10^{-4} the O₃ layer provides little UV shielding, so the direct photolysis rate of H₂O is large at all surface pressures and tends to dominate dissociation. It is particularly dominant at high pressures because the warmer temperatures preferentially moisten the troposphere, where most direct photolysis occurs, while the stratospheric humidity, where a substantial amount of O(¹D) attack takes place, is less affected. In the range $f_{O_2} \sim 10^{-4}$ – 10^{-3} a substantial O₃ layer accumulates and strongly suppresses H₂O photolysis. This lowers the total dissociation rate and causes O(¹D) attack to dominate at all surface pressures. When $f_{O_2} \sim 10^{-3}$ – 10^{-2} a thick O₃ layer forms. At low surface pressure this strongly heats the cold trap, allowing more H₂O into the stratosphere where it can be directly photolyzed or attacked by O(¹D). This enhancement in dissociation is not seen in high pressure atmospheres because the O₃ layer is high above the cold trap and warms it only weakly.

The details of these effects are illustrated for a 1 bar atmosphere in Fig. 3.9. It is seen that for low f_{O_2} most H₂O dissociation occurs by photolysis in the lower troposphere, similar to modern Mars (Nair et al. 1994). On the other hand, for high f_{O_2} dissociation by O(¹D) attack becomes dominant, as on modern Earth (Levy 1971). This is due to the shielding of direct H₂O photolysis by O₃ UV absorption and the enhanced production of O(¹D) by photolysis of O₃. The shielding of H₂O is partially counteracted by humidification of the stratosphere, increasing the rate of H₂O photolysis above the O₃ layer.

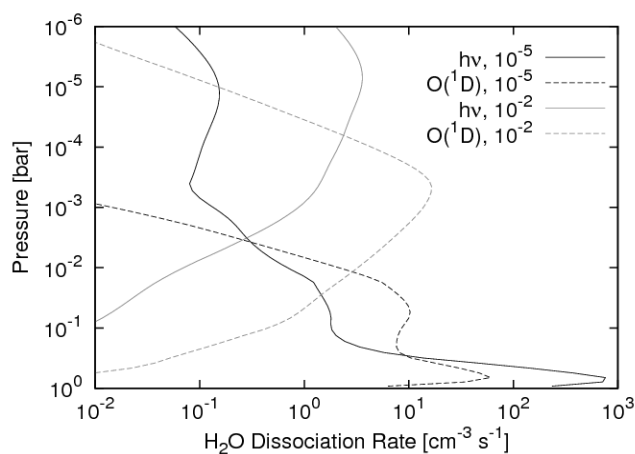


Figure 3.9: Comparison of H₂O dissociation profiles by photolysis and O(¹D) attack for $f_{O_2} = 10^{-5}$ and 10^{-2} . Line titles are in the format (dissociation type, f_{O_2}).

The primary effect of reducing insolation is to scale down the overall rate of H₂O dissociation. This is mostly due to the lower temperatures reducing the H₂O vapor pressure, with the reduction in UV flux contributing to a lesser extent. This is accurate for

the young Sun, since the majority of penetrating UV capable of dissociating H₂O is at $\lambda > 200$ nm (Ribas et al. 2010). For the thick O₃ layers encountered at $f_{O_2} > 10^{-3}$, the fraction of dissociation by O(¹D) attack is insensitive to changes in S at all surface pressures, varying at most a couple of percent as S was reduced to 0.75. On the other hand, at low insolation it is found that atmospheres with $f_{O_2} \sim 10^{-5}$ – 10^{-4} experience a consistent O(¹D) dissociation fraction of ~ 0.5 , regardless of surface pressure. This difference from the results in Fig. 3.8b is due to the surface temperature at $S = 0.75$ being far more constant as a function of P than it is at $S = 1.00$ (Fig. 3.2a). Thus, direct photolysis does not experience a boost from tropospheric moistening at higher pressures.

3.4 Summary

I have explored here the possibility of a substantial O₃ layer accumulating in the Martian atmosphere for O₂ mixing fractions of 10^{-5} to 10^{-2} , a range reasonable during the volcanically quiescent periods of Mars' history. The parameter space study focused on atmospheres with surface pressures of 0.3–1.0 bar, as they are likely to have less HO_x and thus more O₂ and O₃. I find that for modest O₂ mixing fractions of $f_{O_2} > 10^{-5}$ an O₃ layer capable of effectively protecting primitive life from UV radiation would form. As f_{O_2} approaches 10^{-2} the O₃ column becomes comparable to that of modern Earth ($\sim 10^{19}$ cm⁻²).

The presence of a thick O₃ layer decreases planetary albedo, up to 8.1% for a 1 bar atmosphere with O₃ column $\sim 10^{19}$ cm⁻². A portion of this extra heating goes toward inhibiting CO₂ condensation and weakening convection, both of which act to warm the

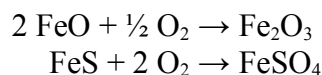
surface for the clear sky conditions examined. However, for thick O₃ layers this surface warming is largely counteracted by stratospheric absorption of solar energy, which efficiently radiates back into space energy which otherwise would have reached the surface. Contribution of O₃ to the greenhouse effect is small under the conditions examined, with a surface temperature increase of only ~ 1 K. The net surface warming effect is underestimated due to the simple photochemical model producing O₃ layers biased toward higher altitudes, but a test including HO_x and eddy mixing suggests the bias is minor.

I have also shown that O₃ has a major influence on the column integrated dissociation rate of H₂O by decreasing UV radiation in the lower atmosphere, increasing the production of O(¹D), and increasing stratospheric humidity. Increasing the thickness of the O₃ layer causes H₂O dissociation to shift from a “modern-Mars-like” state dominated by direct photolysis near the surface to a “modern-Earth-like” state where photolysis is strongly suppressed and O(¹D) attack becomes dominant. For atmospheres > 0.5 bar, an increase in the thickness of the O₃ layer generally lowered the H₂O dissociation rate, with rates at $f_{O_2} = 1 \times 10^{-2}$ being ~ 1/10th their value at $f_{O_2} = 1 \times 10^{-5}$. This suggests the presence of a thick O₃ layer in Mars' past could have suppressed the photochemical production of H₂, and, consequently, the loss of H₂O to space. However, future work with the full photochemical model is required to make a definitive assessment of how a thick O₃ layer would affect H₂ production on ancient Mars.

4. Chemical Surface Sources and Sinks

While it was demonstrated in Chapter 3 that a substantial O₃ layer could have existed in a past thick Martian atmosphere, this is only possible if the O₂ content is sufficiently high. In the atmosphere of Mars, net O₂ accumulates abiotically by dissociation of H₂O followed by the loss of H to space. The O₂ mixing fraction is then determined by the efficiency of O sinks, either by loss to space or weathering at the surface, which balance the H and O loss in a 2:1 ratio. The presence of a volcanic reductant source may also act as an O sink, because geogenic H₂ and CO can reduce O₂ to H₂O or CO₂.

Whether the dominant sink on modern Mars is to space or the surface has recently been a matter of debate. The analysis of Lammer et al. (2003) suggested that only a 20:1 ratio could be accounted for by O loss to space, implying that the planetary surface is the primary sink for O. Redox reactions with Fe and S were considered, which may be represented as



This gives 1 O consumed by every 2 Fe(II) and 4 O consumed by every 1 S. It was also shown that the required balance of these oxidized minerals generated over Mars' history could reasonably be worked down into the subsurface by impact gardening, though the current rate at which this process operates was not evaluated. Following up on the possibility of the surface as an O sink, Zahnle et al. (2008) favored the deposition of atmospheric H₂O₂ and O₃ as the underlying mechanism of surface oxidation. On the other hand, detailed modeling of O loss to space by Fox & Hać (2009) achieved an H:O ratio of

4:1. They cautioned that this value has a high uncertainty, and suggested that loss to space should not yet be ruled out as a major component of the O budget. This is bolstered by the recent modeling of Valeille et al. (2010), which has succeeded in producing O loss rates which approach the necessary 2:1 ratio. Thus, the primary O sink on modern Mars remains slightly controversial. Hopefully, an answer will be provided by the upcoming MAVEN spacecraft, which seeks to measure the current loss rates of species from the Martian atmosphere (including O) and its evolution over time.

Similarly, a reliable estimate of past volcanic emission rates on Mars is elusive. The only volcanic gases in the Solar System for which composition has been measured are on Earth, which is not necessarily a suitable representation for Martian geochemistry (Hirschmann & Withers 2008; Stanley et al. 2011). Also, since Martian volcanic activity has been irregular in space and time, obtaining a globally averaged emission rate during a given period of its history is difficult at best.

For these reasons, a definitive characterization of the O sinks on Mars past and present is beyond the scope of this thesis. Instead, I will focus on what magnitude of O sink is required to strongly violate the assumption of a chemically inert planetary surface, and how such conditions fit in the context of Mars' history. This is a relatively tractable goal, and has received only scattered attention in the literature. Modeling of paleo-Earth has demonstrated that if net O sinks rise above a critical threshold, equal to the rate at which net O is produced by H escape to space, then the atmospheric O₂ content can drop dramatically (Kasting et al. 1979; Kasting & Walker 1981). Modern Mars has been observed to have a net O production rate of $\sim 10^8 \text{ cm}^{-2} \text{ s}^{-1}$ from H escape (Chaufray et al.

2008; Feldman et al. 2011). In addition, modeling suggests that paleo-Mars (Catling & Moore 2003) and paleo-Earth (Kasting et al. 1979) had a similar production rate. Thus, I adopt an O flux of $10^8 \text{ cm}^{-2} \text{ s}^{-1}$ as the order of magnitude a surface O sink must attain to strongly effect the Martian atmosphere's oxidation state. For redox reactions in the subsurface, the following potentially limiting factors are examined: (1) the transport of oxidants and reductants to a reaction zone and (2) the overall reaction rate within this zone. Two types of oxidizer transport are considered: “dry deposition”, in which oxidizing atmospheric gases are directly absorbed by the surface (which may be either regolith, water, or a mixture thereof), and “wet deposition”, in which soluble oxidizers (e.g. H_2O_2) are scavenged from the atmosphere by precipitation and then deposited on the surface. For volcanic emissions a sampling of previous emission estimates is made, and a new estimate for the earliest period of Mars' history is produced based on modeling of the Martian interior.

4.1 Dry Deposition of Oxidants

The dry deposition flux down onto a planetary surface is modeled as the atmospheric concentration $[C]$ of the gas species multiplied by a “deposition velocity” v_d

$$\Phi_d = v_d [C] \quad (4.1)$$

This deposition velocity can be broken down into three resistances

$$v_d = \frac{1}{\rho_a + \rho_b + \rho_c} \quad (4.2)$$

where ρ_a is the resistance to turbulent mixing through the free atmosphere above the surface, ρ_b is the resistance of the “quasi-laminar” boundary layer, a thin (0.1-1 mm) layer of stagnant air just above the surface, and ρ_c is the surface resistance, which depends on how readily the gas species is taken up by the surface. The boundary layer resistance ρ_b is typically very small compared to the other resistances for gas molecule transport, and so is neglected.

4.1.1 Modern Mars

On modern Mars dry deposition is the only plausible pathway by which oxidizers could be transported to the surface. Working under the assumption that surface oxidation comprises the primary O sink on Mars, Zahnle et al. (2008) examined the possibility that the reactive oxidizing species H_2O_2 and O_3 are responsible for surface oxidation. They determined that the highly turbulent atmosphere of modern Mars makes ρ_a relatively small, and thus the surface resistance ρ_c must limit the O loss rate. Photochemical modeling and tuning to observation suggested a value of $v_d = 0.02$ cm/s for H_2O_2 and O_3 . This is not unreasonable for a desert surface deposition velocity. For O_3 deposition in the Nevada desert, Stocker et al. (1987) measured $v_d = 0.11$ cm/s during the day and 0.03 cm/s at night. Similarly, in the Sahara desert Güsten et al. (1996) found 0.1 cm/s during the day and 0.04 cm/s at night. This deposition velocity is also consistent with previous estimates of the flux of H_2O_2 into the Martian subsurface (Bullock et al. 1994).

Zahnle et al. (2008) assumed that all O delivered to the surface by H_2O_2 and O_3 would inevitably oxidize the soil and be incorporated into minerals. However, this may

not be accurate. In fact, the solid state diffusion of reductants, such as Fe^{2+} , from within mineral particles out to the particle surface limits the rate of oxidation under cold, highly oxidizing conditions (Perriat et al. 1996). If transport of atmospheric oxidizers is not the rate limiting step for mineral oxidation, the particle surface may either passivate or catalyze the production of H_2O and O_2 from H_2O_2 and O_3 . The less reactive O_2 is then released back to the atmosphere rather than sequestering it in the mineral. This has been demonstrated for O_3 on Saharan dust by Hanisch & Crowley (2003) and for H_2O_2 on Saharan and Gobi dust by Pradhan et al. (2010). It also explains the unexpectedly slow oxidation rates of Fe bearing minerals by H_2O_2 under simulated Martian conditions found by Chevrier et al. (2006). An illustration of the proposed process is given in Diagram 3.1.

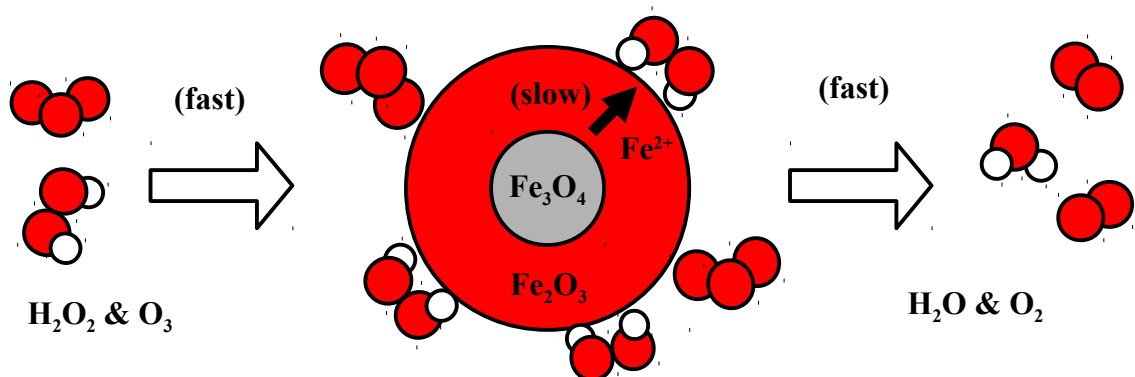


Diagram 3.1: Representation of mineral oxidation by H_2O_2 and O_3 using the shrinking core model, with competition from recombination to H_2O and O_2 .

To provide an estimate of the solid state diffusion limited oxidation rate, a “shrinking core” model may be applied to the regolith particles. The particles oxidize from the outside in, producing an increasingly thick layer of oxidized material that Fe^{2+} from the core must diffuse through to reach the oxidizers at the particle surface. As an

approximation, I assume that the particles are spherical and made entirely of the mineral magnetite (Fe_3O_4), which is oxidized to hematite (Fe_2O_3). This is crudely representative of Fe rich grains in the Martian regolith, and the system lends itself well to the shrinking core model, as there is virtually no volume change after oxidation. Also, the oxidation of Fe_3O_4 appears to be the rate limiting intermediate step for the oxidation of other Fe bearing minerals, including siderite (FeCO_3) (Seguin 1966) and fayalitic olivine (Fe_2SiO_4) (Mackwell 1992). The diffusion coefficient for Fe^{2+} through a product layer of Fe_2O_3 around a core of Fe_3O_4 has been studied as a function of temperature by Sidhu et al. (1977) and Tang et al. (2003). Extrapolating their results to Martian temperatures (210 K) provides a diffusion coefficient $D = 1.0 \times 10^{-26} \text{ cm}^2/\text{s}$. A representative particle radius is taken to be $R = 35 \text{ nm}$ based on the specific density and specific surface area of the fine particles from the Viking lander data (Ballou et al. 1978). Note that this not the actual particle size, but an effective one, due to the porosity of regolith particles. The time it takes to completely oxidize a spherical particle is (Gavhane 2009; p. 4.9)

$$\tau_{\text{ox}} = \frac{R^2}{6D} \quad (4.3)$$

giving a particle oxidation lifetime of 6.5 Myr. This should be considered an order of magnitude value, and is likely underestimated since real Martian magnetite grains are rich in impurities, which reduce the specific density and impede Fe^{2+} diffusion (Sidhu et al. 1977). While this timescale is relatively long compared to the $\sim 0.1 \text{ Myr}$ needed for the atmosphere to achieve photochemical equilibrium on modern Mars, it is quite brief in terms of the planet's history. Since reactive species like H_2O_2 and O_3 can only directly

oxidize minerals close to the surface due to their limited lifetime (Bullock et al. 1994), fresh material from deeper down must be supplied by regular vertical mixing of the regolith in order for the surface to be an O sink for periods longer than ~ 6.5 Myr.

Just how frequently this regolith mixing must occur to maintain the required O sink of $\sim 10^8 \text{ cm}^{-2} \text{ s}^{-1}$ is influenced by how deep the active oxidation zone penetrates, which in turn is controlled by the lifetime of the oxidizing species. Unfortunately, the lifetime of O_3 in the Martian subsurface appears not to have received any study, and the lifetime of H_2O_2 is very poorly constrained, with estimates ranging from minutes to years. The corresponding oxidation zone depths for H_2O_2 range from < 1 cm to ~ 1 m (Zent 1998). Experiments involving H_2O_2 are difficult to perform due to its high reactivity (B. Teolis, & U. Raut, pers. comm., 2011; A. Zent, pers. comm., 2012). However, an H_2O_2 lifetime on the order of minutes would be more consistent with the available laboratory results (Satterfield & Stein 1957; Schumb et al. 1955; Zhao et al. 2011). This suggests that the active oxidation zone on Mars is quite shallow (< 1 cm), and relatively vigorous regolith mixing is required to maintain a significant O sink.

One candidate for such mixing is impact gardening by meteorites. Meteorites which produce craters < 10 m in diameter are effectively blocked by the current Martian atmosphere, so for a crater depth:diameter ratio of 0.20 for simple craters (Strom et al. 1992), the excavated depth will always be > 2 m. This is very deep relative to the active oxidation zone, so it is a reasonable approximation to consider the impact as a resurfacing process which “resets” the area in the basin of the crater and its ejecta blanket with fresh material. Using the Hartmann crater production function for modern Mars (Ivanov 2001),

assuming resurfacing out to 2 crater radii (Zent 1998), and neglecting overlap between craters, a planetary resurfacing time of 84 Myr is obtained. Note that this is significantly longer than the time needed for total oxidation of regolith particles, suggesting that the active zone would completely oxidize between impact resurfacing. Assuming a representative Martian regolith with 14.0 wt% Fe and 2.0 wt% S (Gellert et al. 2004; Gellert et al. 2006; Lammer et al. 2003; McSween & Keil 2000; Redier et al. 1997; Reider et al. 2004), that all Fe and S is initially unoxidized, and an active oxidation zone < 1 cm, this indicates an O sink of $< 10^6 \text{ cm}^{-2} \text{ s}^{-1}$. This flux is far too small to explain the current O sink needed for Mars to be in photochemical equilibrium.

However, meteorite impacts not only transport target material, but also heat it to high temperatures. This raises the possibility that large amounts of hot, dispersed ejecta exposed to the atmosphere during the impact event could become highly oxidized. Assuming a paraboloid geometry for the craters, a depth:diameter ratio of 0.20, the same regolith Fe and S content as before, and *total* oxidation of the displaced crater volume, an impactor driven O sink of approaching the required $10^8 \text{ cm}^{-2} \text{ s}^{-1}$ is achieved. Unlike the surface oxidation model of Zahnle et al. (2008), this rate is relatively independent of the oxidation state of the atmosphere, being determined instead by the impactor flux characteristics at the planet's surface. While intriguing, it should be cautioned that this value is likely overestimated. In reality, the Fe and S in fresh surface material is already significantly oxidized (Lammer et al. 2003), and only a fraction of the displaced crater volume is fated to become ejecta, with the rest being compressed downward. Also, most of the regolith turnover is produced by relatively small impacts, with half generating

craters < 25 m in diameter. It is questionable whether such small impacts could generate sufficient heat or suspend ejecta long enough to ensure total oxidation. On the other hand, the crater production function used here has simply been truncated at 10 m, while in reality Mars' atmosphere has a more gradual filtering effect on small impactors (Popova et al. 2003). Thus, the possibility that impactor driven oxidation of the crust is a significant O sink on modern Mars cannot be ruled out without more detailed work. It is worth noting that this oxidation route would decrease under a thicker Martian atmosphere due to the reduced flux of meteorites reaching the surface. However, in the early Solar System this might be counteracted by the overall greater flux of material during the Heavy Bombardment period.

A less dramatic method of vertically mixing the regolith is by aeolian (wind) transport. Zent (1997) suggested that for short oxidizer lifetimes in the subsurface, aeolian forces would likely be the dominant transport mechanism. Fluvial (water) erosion does not occur to any significant extent on modern Mars, but certainly operated at times in the past. The rate of deflation, i.e. erosion of the surface, necessary to produce an O sink of $10^8 \text{ cm}^{-2} \text{ s}^{-1}$ is only ~ 10 nm/year, which is ~ 1 cm/Myr or ~ 1 m/Gyr. This rate is in line with those inferred from the weathering rind on a basaltic Martian rock (Hausrath et al. 2008) and topographic features in some areas of Mars (Golombek et al. 2006). However, the erosion rate on Mars seems to have varied dramatically over its history, with average rates at the present time being roughly 100 times lower (Golombek et al. 2006) and early rates > 3.4 Gya being roughly 100 times higher (Craddock & Howard 2002). So while aeolian erosion may have played a role in maintaining a surface O sink

in the distant past, it does not seem likely at the present time. It should also be kept in mind that the eroded oxidized material does not vanish, but is simply moved atop material elsewhere on the planet. Thus, in exposing one area to oxidation another is invariably buried more deeply. Depending on how deposition patterns shift over time, aeolian action may serve only to move oxidized material back and forth.

4.1.2 Ancient Mars

For ancient Mars the possibility of liquid water at or near the planetary surface must be considered when evaluating potential O sinks. Reactions involving a gas-liquid interface are much faster than at gas-solid interfaces (Gooding 1978). For aqueous oxidation, the most important species are O_2 , which is only somewhat soluble but has a relatively high atmospheric concentration, and H_2O_2 , which has a very low concentration but also very high solubility. In contrast, O_3 has both a very low concentration and only moderate solubility. I will consider two scenarios for dry deposition onto an aqueous surface in Mars' past: stagnant groundwater and open water in the form of paleolakes.

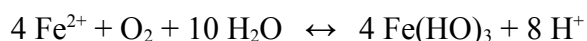
It should be kept in mind that either reductant transport, oxidizer transport, or reaction volume may be the limiting factor for surface oxidation reactions. For ancient Earth, Kasting & Walker (1981) considered the oceans as reaction vessels and determined that the reductant supply of Fe(II) from rivers was not the rate limiting factor for aqueous oxidation. However, since Mars has always possessed a much weaker hydrological cycle than Earth, it is worth reevaluating this concept in the context of this thesis. Using a precipitation runoff factor of 0.2–0.5 (Matsubara et al. 2011) and assuming a river Fe

content similar to Earth, Martian rivers would supply an O sink of $10^8 \text{ cm}^{-2} \text{ s}^{-1}$ for a precipitation rate of $\sim 1 \text{ mm/year}$. This is fairly reasonable rate, comparable to the precipitation received by the driest regions of the Atacama desert on Earth, a region which bears a marked geologic similarity to Mars (Amundson et al. 2008). The precipitation rate could be higher if a large component was snow, because the resulting snowmelt capable of transporting Fe(II) would only be a fraction of the total precipitated. However, it is not clear if it is appropriate to assume that Martian rivers carried a reductant load comparable to those on Earth. Aeolian transport of dust could also serve as an important reductant source to bodies of water. These contributions are difficult to quantify given the currently limited accuracy in understanding and modeling these transport processes on ancient Mars. So while there is a strong possibility that aqueous oxidation on Mars was indeed reductant limited at times in its past, it is difficult to make a definitive assessment given current understanding. For the rest of this section I will generally assume that reductant transport is *not* a limiting factor, and instead focus on oxidizer transport and reaction volume.

In the interest of evaluating oxidizer transport, it is useful to estimate the importance of the free atmosphere resistance ρ_a for the delivery of O_2 and H_2O_2 to the surface. The deposition velocity may then be estimated as $v_d \sim K/H$, with a tropospheric eddy diffusion coefficient $K \sim 10^5\text{--}10^6 \text{ cm}^2/\text{s}$ and a pressure scale height $H \sim 10 \text{ km}$ being suitable for a thick Martian atmosphere. This produces an O transport rate of $10^8 \text{ cm}^{-2} \text{ s}^{-1}$ for an O_2 or H_2O_2 pressure on the order of $10^{-10}\text{--}10^{-11} \text{ bar}$. For an oxidizing atmosphere the O_2 pressure will be much greater than this, so it may be concluded that O_2 deposition

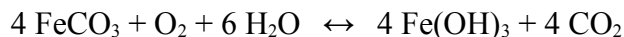
would not be limited by atmospheric transport. However, the current H₂O₂ pressure on Mars falls exactly within this range (Encrenaz et al. 2011). The validation run of the 1 bar full photochemical model in Section 3.1 also produces an H₂O₂ pressure on the order of 10⁻¹⁰ bar. This suggests that on ancient Mars surface deposition of H₂O₂ may have been limited by atmospheric transport.

It is worth mentioning here what the expected product of aqueous oxidation would be on Mars. Marion et al. (2003) showed that unless dissolved O₂ and/or pH are very low, dissolved minerals containing the Fe(II) oxidation state will be driven toward precipitation as oxidized Fe(III) minerals. This is represented by the reaction



They found that a highly acidic pH < 1 was required to dissolve 1000 μM of Fe⁺² even at the relatively modest modern Martian O₂ pressure of ~10⁻⁵ bar. Subsequent reactions may alter the Fe(OH)₃ to goethite (FeO(OH)) and eventually hematite (Fe₂O₃), which also contain the Fe(III) state. Marion et al. (2003) used this example to illustrate that precipitation of Fe phases other than Fe(III) dominated minerals would occur only under the most highly acidic or reducing conditions, and concluded that this explains the prevalence of Fe(III) observed on the Martian surface.

When considering equilibrium chemistry under a thick CO₂ atmosphere, the question arises as to whether the precipitation of other solid phases in the Fe(II) oxidation state, such as FeCO₃, may begin to compete with the formation of Fe(OH)₃. Transition between FeCO₃ and Fe(OH)₃ may be written as



It is seen that 4 CO₂ are released for every O₂ incorporated into the mineral substrate. Applying Le Chatelier's principle, this indicates that it becomes more difficult to precipitate Fe(OH)₃ at higher atmospheric pressure and higher CO₂/O₂ ratio. However, using equilibrium constants for these species from Drever (1997), it is found that FeCO₃ will be stable only for O₂ < 10⁻⁴² bar under a 1 bar CO₂ atmosphere. This clearly shows that, in equilibrium, Fe(OH)₃ should be preferred over FeCO₃ even under weakly oxidizing conditions in a thick CO₂ atmosphere.

For solutions with pH 5–8 the reaction rate of dissolved Fe(II) and O₂ may be expressed as first order with respect to [Fe(II)] and second order for {OH⁻} (Morgan & Lahav 2007)

$$\frac{d[Fe(II)]}{dt} = -k_{O_2}[O_2][Fe(II)]\{OH^-\}^2 \quad (4.4)$$

Under these conditions the dominant Fe(II) species is Fe²⁺, so [Fe(II)] ≈ [Fe²⁺]. Note that the concentration of OH⁻ is given as its activity. Experiments by Millero & Izaguirre (1989) provide a fit for the reaction coefficient k_{O_2} as a function of the temperature and salinity of the solution. Similar work was performed for Fe(II) and H₂O₂ by Millero & Sotolongo (1989), who found a first order dependence in {OH⁻}

$$\frac{d[Fe(II)]}{dt} = -k_{H_2O_2}[H_2O_2][Fe(II)]\{OH^-\} \quad (4.5)$$

The fit for $k_{H_2O_2}$ is based on reaction pathways with two Fe(II) species, one being oxidation of Fe²⁺ and the other being FeOH⁺. The dependence of oxidation rate on pH,

temperature, and salinity for k_{O_2} and $k_{H_2O_2}$ means some assumptions must be made regarding the geochemical environment. Observed Martian mineral assemblages range from carbonate bearing materials which only form under near-neutral pH (Boynton et al. 2009; Michalski & Niles 2010; Wray et al. 2011) to sulfate rich deposits which require a highly acidic environment (Klingelhöfer et al. 2004; Marion et al. 2008; Tosca et al. 2005). This makes for an extensive range of possible aqueous geochemical conditions. However, since the interest here is how much weathering may still allow for an oxidizing atmosphere, I will be conservative and focus on conditions which experience more rapid oxidation. The results of Millero & Izaguirre (1989) and Millero & Sotolongo (1989) suggest that warm, near-neutral pH, freshwater solutions should generally support higher oxidation rates. These conditions seem consistent with the earliest period of Mars' history, when near surface reservoirs of liquid water were likely most extensive. Later cold, acidic, briny Martian environments would be expected to have much slower oxidation rates and would have occurred under highly water limited conditions (Marion et al. 2008; Tosca et al. 2005). In light of this, I examine here two simple but illustrative freshwater scenarios: (1) a “weakly buffered” case consisting of a saturated solution of $FeCO_3$, and (2) a “strongly buffered” case which is saturated with respect to both $FeCO_3$ and $CaCO_3$. The strongly buffered case represents a reasonable upper estimate for the aqueous oxidation rate, and is consistent with the identification of $FeCO_3/CaCO_3$ minerals excavated from the subsurface by large impact craters (Michalski & Niles 2010; Wray et al. 2011). To perform the aqueous chemistry calculations the FREZCHEM v13.3 model (Marion et al. 2010) is used with a 1 bar CO_2 atmosphere at 273.15 K. The results are

shown in Table 4.1.

	FeCO₃ Buffer	CaCO₃ Buffer
pH	5.2	6.1
[Fe²⁺] (μM)	43	1600
[FeOH⁺] (M)	1.2×10^{-9}	8.1×10^{-9}
{OH⁻} (M)	1.7×10^{-10}	1.3×10^{-9}
O₂ Reaction Rate (s⁻¹)	1.5×10^{-9}	2.4×10^{-9}
H₂O₂ Reaction Rate (s⁻¹)	2.5×10^{-3}	3.9×10^{-2}
O₂ Lifetime	11 Martian Years	7 Martian Years
H₂O₂ Lifetime	7 Minutes	0.5 Minutes

Table 4.1: Characteristics of aqueous oxidation of Fe(II) in FeCO₃ and CaCO₃ buffered solutions under 1 bar CO₂ at 273.15 K.

These values for pH and dissolved Fe(II) may be compared with previous studies of aqueous Martian geochemistry (Table 4.2). Catling (1999) modeled an Fe rich solution in contact with ultramafic Martian rocks to study evaporite deposition. Later work by Catling & Moore (2003) on oxidation reactions in Martian bodies of water assumed conditions similar to the Precambrian oceans of Earth. Finally, the experimental work of Bullock et al. (2004) was produced by introducing simulated Martian rock to water under a Mars-like atmosphere containing CO₂, N₂, and O₂ at 1 bar. The two buffering scenarios considered in this thesis compare well with the range of conditions in these previous studies, and are appropriate for providing conservative estimates of O loss to a wet ancient Martian surface.

Study	pH	[Fe(II)] μM
This Work	5.2–6.1	43–1600
(Bullock et al. 2004)	4.2–6.0	1–10
(Catling & Moore 2003)	4.5–6.0	90
(Catling 1999)	5.0–6.7	800

Table 4.2: Comparison of adopted solution conditions with previous modeling and experiment.

While the pH and [Fe(II)] differ significantly between the two buffering cases, the lifetime of O_2 changes by less than 40%. In the weakly buffered case [Fe(II)] is high due to the high solubility of FeCO_3 , but this is counteracted by the low pH, which makes oxidation slow. In the strongly buffered case [Fe(II)] is low due to the lower solubility of FeCO_3 in the presence of the CaCO_3 buffer, but overall the rate is somewhat higher because the high pH makes oxidation by O_2 very fast. The change in lifetime for H_2O_2 is more dramatic, about a factor of 16, because its reaction rate is only first order in $\{\text{OH}^-\}$ and so the decrease in pH does not balance the increase in [Fe(II)] between the weakly and strongly buffered cases.

Using the aqueous oxidation conditions in Table 4.1, the dry deposition O sink rate may now be evaluated for various wet surface configurations. The first scenario I consider is the uptake of oxidizer by stagnant groundwater. This requires finding the steady state solution for the diffusion equation

$$\frac{\partial C}{\partial t} = D \frac{\partial^2 C}{\partial z^2} - RC \quad (4.6)$$

where C is oxidizer concentration, z is depth measured from the water table, D is the effective diffusion coefficient [cm^2/s] of the oxidizer in water, and R is the effective oxidation reaction rate [s^{-1}]. Applying the boundary condition $C(z=0)=C_{eq}$, where C_{eq} is the concentration of oxidizer in equilibrium with its atmospheric pressure above the water table, the solution is

$$C(z)=C_{eq} e^{-\frac{z}{d}} \quad (4.7)$$

where the characteristic depth $d=\sqrt{D/R}$ has been defined. This is representative of the scale at which the oxidizer concentration diminishes with increasing depth. The surface resistance for oxidizer uptake may be expressed as a deposition velocity $v_d=\sqrt{DR}$, and the O flux then calculated by substituting C_{eq} into Eq. (4.1).

Within the saturated soil the effective diffusion coefficient D is calculated from the “free solution” diffusion coefficient D_0 multiplied by a porosity θ and tortuosity τ . (Shackelford & Daniel 1991). Similarly, the effective reaction rate R is the free solution value R_0 multiplied by θ . A representative value for both θ and τ is ~ 0.3 . Using $D_0 = 1.2 \times 10^{-5} \text{ cm}^2/\text{s}$ for O_2 (Kasting & Walker 1981) and $D_0 = 6.0 \times 10^{-6} \text{ cm}^2/\text{s}$ for H_2O_2 (Schumb et al. 1955) in water at 273.15 K and applying the reaction rates for the two buffering cases, I find $d_{\text{O}_2} = 40\text{--}50 \text{ cm}$ and $d_{\text{H}_2\text{O}_2} = 0.07\text{--}0.3 \text{ mm}$. This suggests that an oxidation zone on the order of meters would exist below the water table, the extent of which would be limited by the penetration of O_2 . Setting the O flux to $10^8 \text{ cm}^{-2} \text{ s}^{-1}$, FREZCHEM is used to calculate that a remarkably oxidizing O_2 pressure of $1.4\text{--}1.7 \times 10^{-3} \text{ bar}$ would be in equilibrium with the groundwater in this configuration. On the other

hand, doing the same calculation for H_2O_2 gives a miniscule equilibrium pressure of $2.2\text{--}8.9 \times 10^{-15}$ bar using the Henry's Law constant of 9.3×10^5 mol/L/bar at 273.15 K from (Huang & Chen 2010). It may be concluded from this that oxidation of the surface by H_2O_2 would definitely be limited by atmospheric transport, given the earlier estimate that an O flux of $10^8 \text{ cm}^{-2} \text{ s}^{-1}$ could only be maintained for a much higher pressure of $10^{-10}\text{--}10^{-11}$ bar.

It should be noted that the equilibrium H_2O_2 pressure above the water table is most likely *not* the same as the H_2O_2 pressure at the planetary surface. Recall from the previous section that the limited subsurface lifetime of H_2O_2 does not allow it to penetrate more than a few mm below the surface. If the water table is located deeper than this, as it often would be, then the H_2O_2 pressure would be negligible at the water table and uncoupled from conditions in the atmosphere. However, the groundwater flux for H_2O_2 is still applicable to “dry lakes” in which the water table rises up to intersect the surface during seasonal wetting. This makes the uptake of H_2O_2 highly dependent on the availability of water at the planet's surface. O_2 does not share this sensitivity, since its lifetime in the subsurface is very long, and the crossing of the so-called “vadose zone” (“vadose” being the Latin for “shallow”) from the planet's surface to the water table through the porous soil does little to inhibit its transport. In fact, since molecules travel through a 1 bar gas $\sim 10^4$ times faster than through water, the vadose zone on ancient Mars would need to be several kilometers deep before it began to interfere with the delivery of O_2 to the groundwater.

I will now consider the characteristics of aqueous oxidation in Martian paleolakes.

These bodies of open water readily absorb H_2O_2 from the atmosphere, and deposition is again limited by atmospheric transport and the available area of open water. Therefore, I will focus on O_2 oxidation under water limited conditions, in which aqueous reactions are constrained not by transport of reactants but by the total volume of solution present. Such conditions are likely to have occurred on Mars (Hurowitz & McLennan 2007). The dissolved O_2 is assumed to be well-mixed throughout the water column and in equilibrium with its atmospheric pressure. Given an O source of $10^8 \text{ cm}^{-2} \text{ s}^{-1}$, the equilibrium atmospheric O_2 concentration is then easily calculated for Martian paleolakes of a given total volume. Some suitable examples are given in Table 4.3, along with the results for stagnant groundwater. The surface area of Mars happens to be nearly identical to the land area of Earth, so it seems appropriate to examine the effect of supplying Mars with an amount of water equal to the total lake volume of Earth. At $175 \times 10^3 \text{ km}^3$ (Oki & Kanae 2006), this would represent a 1.2 m global equivalent layer (GEL) of water on Mars. The results of Matsubara et al. (2011) suggest that a system of lakes of around 8.3 m GEL is consistent with the geomorphology of terrain dated to the relatively wet Late Noachian era of Mars' history. Finally, it is informative to explore the case of total melting of the polar ice caps (22 m GEL), which currently represent the largest reservoir of surface water on Mars (Carr & Head 2003; Plaut et al. 2007). For an O flux of $10^8 \text{ cm}^{-2} \text{ s}^{-1}$, all of these scenarios are capable of coexisting with O_2 pressures comparable to or higher than that of the current oxidizing Martian atmosphere.

Aqueous Solution	GEL [m]	Equilibrium O ₂ Pressure [bar]	
		FeCO ₃ Buffer	CaCO ₃ Buffer
Groundwater	NA	1.7×10^{-3}	1.4×10^{-3}
Earth Lake Volume	1.2	2.1×10^{-4}	1.3×10^{-4}
Noachian Lake Volume	8.3	3.0×10^{-5}	1.9×10^{-5}
Total Polar Caps' Volume	22	1.1×10^{-5}	7.2×10^{-6}

Table 4.3: Various scenarios for oxidation rates by O₂ in aqueous solution which represent a globally averaged O sink of 10^8 cm²/s. GEL = global equivalent layer of water. For comparison, the O₂ pressure is 8×10^{-6} bar on modern Mars .

However, it is quite likely that many Martian paleolakes would have experienced surface freezing for a significant fraction of the year, as do lakes at high latitude and altitude on Earth. During these periods atmosphere-water transport and water column mixing would be shut down, violating the assumptions made previously. In the extreme case, the lake would be *amictic* and have a perpetually frozen surface, rendering it inert as an atmospheric chemical sink. A more interesting case, involving regular atmosphere-water communication, is that of a *cold monomictic lake*. These lakes maintain a frozen surface nearly year-round, but are punctuated by a brief thaw in the summer, during which time the water column undergoes a complete mixing from top to bottom. This makes these lakes an analytically tractable but realistic case study for understanding Martian paleolakes as a sink for atmospheric oxidizers.

Consider a cold monomictic lake as a reaction vessel which receives an annual injection of oxidizer from the atmosphere during its brief ice-free summer period. After this injection the dissolved oxidizer is in equilibrium with the atmosphere and has a constant concentration throughout the water column due to post-thaw mixing. These

conditions are identical to those considered previously for oxidation with an unimpeded atmosphere-water interface. However, the lake surface refreezes shortly after the injection and any dissolved oxidizer is steadily consumed beneath the ice. Since the aqueous lifetime of O_2 is much longer than a Martian year (Table 4.1), the somewhat surprising result is that being frozen over for most of the year does little to impede the ability of a cold monomictic lake to sink atmospheric O_2 . So little oxidation occurs between annual summer replenishments that $[O_2]$ does not change significantly from $[O_2]_{eq}$ during the time the liquid is cut off from the atmosphere. The annually averaged flux of O into a cold monomictic lake is thus very close to that of a well mixed lake which never freezes over. This is convenient, as it means that the rate of O_2 loss by aqueous oxidation in cold Martian lakes has little dependence on the details of seasonal freezing and mixing. On the other hand, it makes O_2 loss to lakes highly sensitive to the climatic transition from cold monomictic to amictic. In effect, the sink is fully “on” for the cold monomictic regime and fully “off” for the amictic regime. In contrast with O_2 , the short lifetime of H_2O_2 ensures that its role as an O sink is immediately cut off during periods of lake freezing.

4.2 Wet Deposition of Oxidants

Another mechanism by which atmospheric oxidants are transported to the surface is wet deposition. In this process, soluble species attracted to H_2O are scavenged by cloud aerosols and then precipitated as either rain or snow. The oxidizer this is most important for is H_2O_2 , since, as seen previously, it is very soluble and often transport limited in oxidizing the surface. At the cold tropospheric temperatures of ancient Mars, the Henry's

Law constant for H_2O_2 in liquid water is of order 10^6 mol/L/bar (Huang & Chen 2010). This high solubility suggests that the majority of atmospheric H_2O_2 will be dissolved during a storm event, making its rainout lifetime essentially the precipitation frequency (Giorgi & Chameides 1985). The situation is somewhat more complex for solid precipitation, e.g. snow. It has been shown by Mari et al. (2000) that any H_2O_2 accumulated by supercooled droplets will largely be ejected from the droplet during freezing. And at temperatures below -40°C (233 K) water vapor condenses directly to ice crystals. Under these conditions, H_2O_2 is incorporated by direct deposition from the vapor to solid phase, making the H_2O_2 content governed not by thermodynamics but by kinetics (Sigg et al. 1992). These effects make solid precipitation less efficient at removing H_2O_2 from the atmosphere, and the rainout lifetime of H_2O_2 may be significantly longer than the storm frequency. However, accurate calculation of these processes requires a detailed treatment of the microphysics of cloud condensation on Mars, which is beyond the scope of this thesis. Therefore, in the interest of simplicity, I will assume that the majority of the H_2O_2 column is precipitated during storm events, giving an upper limit on its efficiency as an O sink.

Estimating the storm frequency on ancient Mars is an uncertain calculation at best, however, even an order of magnitude value is sufficient. Treating precipitation as a compound Poisson process (Alexandersson 1985), the average time between storms $\langle\omega\rangle$ can be related to the average precipitation rate $\langle r\rangle$ and average storm depth $\langle d\rangle$ (the amount of precipitation deposited during a storm event) by the expression

$$\langle r\rangle = \langle d\rangle \langle \omega\rangle \quad (4.8)$$

A reasonable estimate for $\langle d \rangle$ can be obtained using the average precipitable water $\langle p \rangle$, the column of H₂O in the atmosphere.

Crude estimates for $\langle r \rangle$ and $\langle p \rangle$ are obtained from a simple diffusion model of H₂O transport from the surface up to the condensation altitude. For a Martian 1 bar CO₂ atmosphere at 273 K and 20% relative humidity, $\langle r \rangle \sim 20$ mm/year and $\langle p \rangle \sim 4$ mm. The corresponding globally averaged values for Earth are $\langle r \rangle \sim 1000$ mm/year and $\langle p \rangle \sim 25$ mm. Regions of Earth having $\langle r \rangle < 250$ mm/year are typically considered deserts. These values may also be compared with the 2 mm/year precipitation rate used by Johnson et al. (2009) to model ancient Mars, approximating conditions in the Atacama desert. Given the great uncertainties involved, the diffusion model produces a fairly reasonable set of values with which to work.

Here I demonstrate that the storm depth d is directly correlated with the available precipitable water p , employing terrestrial climatological data to derive $\langle d \rangle$ from $\langle r \rangle$ and $\langle \omega \rangle$ and correlate it with $\langle p \rangle$. The CRU TS 2.1 database is used to obtain the mean precipitation rate and number of wet days (> 0.1 mm precipitation) (Mitchell & Jones 2005). Precipitable water values are obtained from the MERRA database (Rienecker et al. 2011), as this variable is not contained in the CRU TS. The modern satellite observations upon which the MERRA is based are not available before 1979, and in the CRU TS wet day values after 1990 are not based on observation, but are instead synthetically generated. Thus, to ensure the analysis is based on observations and that values from the MERRA are simultaneous with values from the CRU TS, I have chosen to use data based upon the decadal average of 1981-1990.

The continent of South America was excluded from the analysis because of a positive bias in wet days from Brazilian stations used in the CRU TS, a result of the conversion method used to extrapolate a 0.1 mm wet day threshold from records based on a 1.0 mm threshold. Greenland was also excluded due to its poor weather station coverage. In the production of the CRU TS grids, the number of wet days in a month were not allowed to exceed the amount of precipitation (in mm) (Mitchell & Jones 2005). The effect is an artificially increase $\langle d \rangle$ in this analysis. To remove this artifact, I excluded all grid points which had been reset in this way for one or more months of the year. In order to accurately calculate $\langle d \rangle$ it must be certain that most of the wet days have been recorded. Assuming an exponential distribution for d and using the CRU TS wet day threshold of 0.1 mm, it is estimated that $\langle d \rangle > 2$ mm is required for at least 95% of the precipitation events to be recorded as wet days. Thus, regions with $\langle d \rangle < 2$ mm have been excluded from the analysis.

To examine the relationship between $\langle d \rangle$ and $\langle p \rangle$ I define a proportionality factor $\langle \eta \rangle = \langle d \rangle / \langle p \rangle$, which may be thought of as the mean fraction of the precipitable water actually precipitated during a storm. The histogram of $\log(\langle \eta \rangle)$ in Fig. 4.1 is approximately normally distributed, though some enhancement is evident in the right tail. Investigation reveals that this tail is attributable to areas with intense orographic lift (i.e. large mountains). In order to obtain robust statistics I calculate a 5% trimmed mean and Winsorized variance. This yields $\log(\langle \eta \rangle) = -0.46 \pm 0.14$, or $\langle \eta \rangle \approx 1/3$ with a likely range of 1/4–1/2. For Earth's globally averaged atmospheric water budget this predicts a precipitation frequency $\langle \omega \rangle \approx 3$ days. As a tropospheric average, this is consistent with

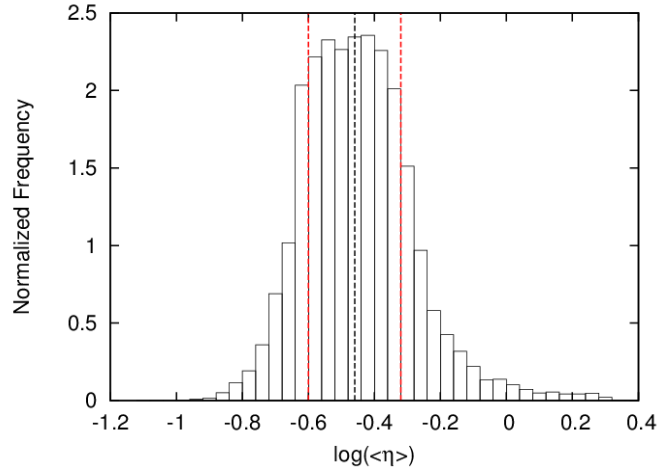


Figure 4.1: Frequency distribution of $\log(\langle \eta \rangle)$ for Earth derived from CRU TS and MERRA data. The mean of -0.46 is indicated by the heavy dashed black line, and the standard deviation of ± 0.14 is indicated by the red dashed lines.

the 1D parametrized rainout model of Giorgi & Chameides (1985) and the rainout of HNO_3 in the 3D global chemistry-transport model of Neu & Prather (2012). While the variability of η is substantial in the context of Earth science, using $\langle \eta \rangle = 1/3$ is satisfactory for the purpose of estimating rainout rates on ancient Mars. Its accuracy is probably comparable to that of the simple diffusion model in predicting the mean precipitation rate $\langle r \rangle$.

Substituting in the values of $\langle r \rangle \sim 20$ mm/year and $\langle p \rangle \sim 4$ mm for the Martian climate example, I obtain $\langle d \rangle \sim 1$ mm and $\langle \omega \rangle \sim 20\text{--}30$ days. This is comparable to precipitation frequencies in many desert regions on Earth. If most of the H_2O_2 column is precipitated during a storm event, an O flux of $10^8 \text{ cm}^{-2} \text{ s}^{-1}$ is achieved for 10^{-11} bar H_2O_2 . This is similar to the pressure needed to support the same flux using turbulent atmospheric transport. It suggests that wet deposition of H_2O_2 could have been an

important contributor to the flux of oxidizing species to the ancient Martian surface when a modest hydrological cycle was active.

However, this assumes that all of the wet deposited H_2O_2 goes on to participate in redox reactions. When Kasting et al. (1985) examined the wet deposition of H_2O_2 for Earth under paleoclimate conditions, they estimated an H_2O_2 lifetime in the soil on the order of 1 day before reacting with minerals. They assumed that all of the H_2O_2 would disproportionate to $\text{H}_2\text{O} + \frac{1}{2}\text{O}_2$, and that the penetration achieved over the H_2O_2 lifetime would ensure this occurred at sufficient depth that the O_2 generated would oxidize soil material before it could diffuse out to the relatively O_2 poor atmosphere. Their argument is convenient for estimating O loss to the surface by wet deposition of H_2O_2 , because it allows one to simply assume that one O is consumed for every H_2O_2 deposited.

This scenario is not consistent with the analysis of aqueous oxidation on Mars that has been performed here. The lifetime of H_2O_2 is on the order of minutes, preventing it from penetrating very deeply into the subsurface, and the lifetime of O_2 is over several years, allowing it to easily diffuse out to the atmosphere. It seems more likely that oxidation would be directly mediated by H_2O_2 and limited by the ability of that species to diffuse out of the wet soil. The oxidation efficiency is characterized by a factor X_{ox} , equal to the amount of oxidizer consumed in redox reactions as a fraction of the original amount deposited by the precipitation event. Upon exiting the saturated portion of the soil the H_2O_2 would rapidly diffuse away through the subsurface and be decomposed by heterogeneous reactions, as explored in Section 4.1. Thus, the problem may be simplified by assuming an equilibrium H_2O_2 pressure ~ 0 at the interface between the aqueous

solution and subsurface pore space atmosphere. For a free layer of precipitated solution of depth d in the subsurface open to pore space atmosphere both above and below, an effective diffusion coefficient D and an effective reaction rate R , the oxidation fraction is

$$X_{ox} = 1 - \frac{2}{u} \tanh\left(\frac{u}{2}\right) \quad (4.9)$$

where the dimensionless parameter $u = d\sqrt{(R/D)}$ characterizes the efficiency of escape from the layer. More oxidizer escapes for small u , while less escapes for large u . Another plausible scenario is that the precipitated layer is in contact with a subsurface water table depleted in H_2O_2 . In this case the system is open to atmosphere only at the top boundary, and the oxidation fraction is

$$X_{ox} = 1 + \frac{1}{u}(e^{-u} - 1) \quad (4.10)$$

Derivations for Eq. (4.9) and (4.10) are available in Appendix C. Example values for X_{ox} are given in Table 4.4 using $d \sim 1$ mm and the values for D and R from Section 4.2. An additional case has been calculated for an unbuffered $[Fe(II)] = 10$ μ M solution with pH = 3.9. This is more representative of conditions in Martian rainwater just after precipitation. It would take at least a few minutes for pH buffering minerals to dissolve into the solution, as in the Phoenix lander wet chemistry experiment (Boynton et al. 2009), which is comparable to the time it takes for H_2O_2 to diffuse out of the system. Under these conditions, H_2O_2 has a much longer lifetime of 1.6 hours, which is reflected by the X_{ox} being significantly lower than the other cases. This suggests that the ability of wet deposited H_2O_2 to sink O is largely controlled by events in the first several minutes

after precipitation. An accurate analysis would require a detailed treatment involving dissolution of minerals and a time varying reaction rate.

	Unbuffered	FeCO₃ Buffer	CaCO₃ Buffer
Free Layer	0.07	0.49	0.86
Adjacent to Water Table	0.36	0.74	0.93

Table 4.4: Comparison of X_{ox} for various aqueous oxidation conditions. A precipitated solution layer of thickness 1 mm is assumed.

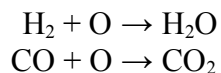
One last possible deposition process for H₂O₂ in the Martian atmospheres under consideration is the possibility that it could accumulate up to its condensation point and precipitate directly (Kong & McElroy 1977). Unfortunately, the literature lacks any direct measurements of H₂O₂ vapor pressure over the solid phase (Fray & Schmitt 2009). The unstable nature of H₂O₂ makes its vapor pressure difficult to measure, as it is prone to decompose upon contact with the walls of its containment vessel and the pressure gauge itself (Manatt & Manatt 2004). I have therefore developed new formulations for the vapor pressure of H₂O₂ based on theoretical and experimental data for the gas, liquid, and solid phases that are available in the literature. The method and resulting formulations are described in Appendix B.

For an H₂O₂ pressure of 10⁻¹⁰ bar, comparable to the tropospheric concentration on modern Mars, a condensation point of 142 K is calculated. This is very cold, and even on modern Mars such low temperatures are not reached except high in the stratosphere and at the extreme poles during winter. H₂O₂ pressures are not expected to be much larger than 10⁻¹⁰ bar for the ancient Martian troposphere, and the warmer temperatures expected

for a thicker atmosphere would tend to make it even more difficult for H₂O₂ to condense in the troposphere. This does not rule out the possibility of stratospheric H₂O₂ clouds on ancient Mars. However, as on Earth, the lack of convection in the stratosphere would only weakly suspend the precipitating particles, preventing them from growing large enough to avoid evaporation before reaching the surface. Thus, direct precipitation of H₂O₂ on ancient Mars is unlikely, and wet deposition as a component of H₂O precipitation is more important.

4.3 Volcanic Source of Reductants

Gaseous volcanic emissions on Earth are rich in highly reducing species, primarily H₂ and CO, and this is expected to also be the case on Mars (Craddock & Greeley 2009). Of these two species, H₂ is the more abundant. Once injected into the atmosphere, these species chemically reduce the atmosphere's oxidation, each acting to consume 1 O per molecule released



Previous estimates used for reductant emission rates in Mars past vary considerably. In modeling SO₂ photochemistry on ancient Mars, Tian et al. (2010) assumed a volcanic H₂ production rate of $1 \times 10^{10} \text{ cm}^{-2} \text{ s}^{-1}$, comparable to that used for models of Earth. This is not particularly realistic, as it does not take into account the fact that Mars is much less volcanically active than Earth. Catling & Moore (2003) used a much smaller value of $3.6 \times 10^8 \text{ cm}^{-2} \text{ s}^{-1}$ in studying the environmental conditions

necessary for the production of hematite (Fe_2O_3) deposits on Mars. This was based on scaling the volcanic activity of early Earth down to a less intense Martian level using the eruption rate estimates of Jakosky & Shock (1998).

While there is no evidence for current volcanic activity on Mars, it has been inferred from the dating of volcanic edifices, lava fields, and Martian meteorites that have landed on Earth that there has been major activity as recently as $\sim 100\text{--}200$ Ma (Neukum et al. 2010; Robbins et al. 2011). As a general trend, it appears that Mars' volcanic activity has steadily declined over the past several Gyrs, and so a greater flux of volcanic emissions can be expected the further back one goes. For the current time, Kiefer (2003) has estimated a very low lava eruption rate of $\sim 10^{-4}$ km^3/year . Examining the volume of volcanic features emplaced over the past 3.8 Gyr, Greeley & Schneid (1991) inferred that the sum of extrusive and intrusive volcanism (i.e. above and below the surface) has produced material at an average rate of 0.17 km^3/year , which they compared to an estimated $26\text{--}34$ km^3/year for modern Earth. However, only the extrusive component of volcanism generates eruptions which efficiently outgas to the atmosphere. Greeley & Schneid (1991) estimated an average extrusion rate of 0.02 km^3/year on Mars over the past 3.8 Gyr, much larger than the estimate of Kiefer (2003) for the present. Estimates of volcanic activity extending beyond 3.8 Gyr into the Noachian, the earliest period of Mars' history, become increasingly uncertain due to the terrain being heavily cratered and altered by erosion. However, convective modeling of the Martian mantle has been used by O'Neill et al. (2007) to fit to the observed extrusion rates and extrapolate backward into the Noachian. Fitting to the average rate of Greeley & Schneid (1991), they found a

Noachian eruption rate of just under $0.06 \text{ km}^3/\text{year}$, while fitting to the current rate estimate of Kiefer (2003) suggested a Noachian rate closer to $0.02 \text{ km}^3/\text{year}$. This agreement is reasonably good, considering the uncertainties involved in the parameters governing mantle convection and volcanism on Mars.

To convert these extrusion rates into reductant emission rates, Craddock & Greeley (2009) suggested that measurements of the volcanic gas composition and outgassing per extruded volume from terrestrial Hawaiian basalts could be used. Using their figures, the O sink represented by H_2 and CO emission from a $0.06 \text{ km}^3/\text{yr}$ volcanic source would be $8 \times 10^7 \text{ cm}^{-2} \text{ s}^{-1}$, while for $0.02 \text{ km}^3/\text{yr}$ it would be $3 \times 10^7 \text{ cm}^{-2} \text{ s}^{-1}$. Note that these values are of order the $10^8 \text{ cm}^{-2} \text{ s}^{-1}$ needed to strongly perturb the oxidation state of the Martian atmosphere. However, it should be recognized that these rates are averaged over geologic timescales on the order of a Gyr, and that Mars' volcanic activity has been episodic over such periods of time (Neukum et al. 2010; Robbins et al. 2011). Episodes of high activity would thus produce emission rates significantly greater than $10^8 \text{ cm}^{-2} \text{ s}^{-1}$, and would be separated by periods in a less active or quiescent state with rates much less than $10^8 \text{ cm}^{-2} \text{ s}^{-1}$. This quantitatively shows that an oxidizing Martian atmosphere could not be in photochemical equilibrium during past periods of volcanic activity. It validates the qualitative argument made at the beginning of this thesis that only the periods of time between volcanic episodes could have supported the oxidizing conditions necessary to support a substantial O_3 layer.

It is worth making a note here regarding the assumption that terrestrial volcanic gases are representative of Martian emissions. The recent results of Hirschmann &

Withers (2008) and Stanley et al. (2011) concerning the CO₂ content of Martian basalts demonstrate that terrestrial volcanic analogs must be used with caution. Their measurements indicate that the O₂ fugacity of the Martian mantle is much less than that of Earth, suggesting that Martian magma is more reducing. On the other hand, recent work has also demonstrated that the H₂O content (McCubbin et al. 2012) and temperature conditions (Baratoux et al. 2011) of the Martian mantle are very similar to that of Earth. Along with O₂ fugacity, these factors are what determine the H₂ content of magma (Holland 1962). Based these measurements, volcanic emissions on Mars are expected to have greater H₂ content than those on Earth. This drives the atmosphere into a reducing state using a lower eruption rate than otherwise, and cements the conclusion that oxidizing conditions on Mars would be limited to volcanically quiet periods.

4.4 Summary

In this chapter I have examined a variety of O sinks for Mars both past and present. Loss of O to the modern Martian surface is limited by the regolith turnover rate, and likely plays only a minor role in the O budget compared to loss of O to space. Aqueous O₂ oxidation on ancient Mars was likely water limited, and considerable amounts of liquid water, up to ~ 20 m across the planet, are compatible with an O₂ pressure comparable to or higher than the present value. H₂O₂ dry deposition is primarily limited by atmospheric transport and the availability of open water that it may readily dissolve in. Wet deposition of H₂O₂ has the potential to be an important O sink on ancient Mars, but an accurate determination of the flux requires more detailed modeling of its

precipitation with H₂O and reaction in the surface after deposition. Direct precipitation of H₂O₂ in the troposphere is found to be unlikely on ancient Mars. Finally, it is shown using estimates of past Martian volcanism that oxidizing atmospheric conditions could only exist during the quiescent periods between episodes of volcanic activity.

5. Conclusions

In this thesis I have examined the possibility that a substantial O₃ layer could have formed on ancient Mars and provided feedback on the atmospheric photochemistry and climate. For this purpose a detailed 1D climate model using line-by-line radiative cross-section calculations was developed and coupled to a photochemical model. I find that the most favorable conditions for O₃ accumulation are likely to be atmospheres of 0.3–1 bar CO₂ with a chemically passive planetary surface. The literature suggests that these conditions could support mixing fractions of O₂ in the range of 10⁻⁵–10⁻². My modeling demonstrates that in such relatively thick, oxidizing atmospheres a significant O₃ layer could indeed form. Climate forcing by these O₃ layers includes reduction of planetary albedo by several percent, suppression of CO₂ condensation and convection in the upper troposphere, and a slight greenhouse effect of order 1 K. Overall, the climate forcing exerted by a thick Martian O₃ layer is found to be small, and irrelevant to the problem of warming Mars' surface above the freezing point of water. On the other hand, effective shielding of UV radiation harmful to primitive life is obtained for O₂ mixing ratios only somewhat higher than 10⁻⁵. The presence and thickness O₃ layer also has a strong effect on the H₂O dissociation rate. For thin O₃ layers, H₂O dissociation is “Mars-like”,

occurring at a high rate and being driven by photolysis, while for thick O₃ layers it is “Earth-like”, being typically slower and controlled by O(¹D) attack.

Investigation of non-passive surface conditions was also performed to identify how large Martian weathering rates and volcanic emissions could be while still maintaining a relatively oxidizing atmosphere. It is found that modern Mars is not likely to support a major surface O sink, and that most current O loss must be to space. For wetter past climates weathering by O₂ is typically water limited, with the equivalent of a global ~20 m layer of liquid water still allowing for an O₂ pressure comparable to the modern value. Weathering by H₂O₂ is transport limited by atmospheric turbulence and availability of open water for dry deposition. Wet deposition of H₂O₂ may be comparable to dry deposition, but a more detailed analysis of cloud microphysics and time dependent redox reactions in the subsurface are necessary for an accurate determination. An estimate was made of the level of volcanic activity during the first billion years of Mars' history, and indicates that oxidizing conditions could not have existed during one of the planets' global episodes of volcanism. Oxidizing conditions could only have been stable during the less active interludes separating these bursts of activity.

In conclusion, these results indicate that at some time (or times) in the past Mars likely did support an O₃ significantly thicker than its present one. Further investigation is warranted using the full photochemical model that I have developed, and inclusion of a non-passive planetary surface to study in detail the transition from oxidizing to reducing atmospheric conditions is of particular interest. A thorough evaluation of O₃ feedback on the H₂ budget and atmospheric escape processes is also a potentially fertile topic of study.

Interactions of an O₃ layer with clouds made up of CO₂, H₂O, and possibly H₂O₂ is another intriguing area for future work. The concept of a substantial O₃ layer in Mars' past offers rich possibilities in the ongoing investigation of the planet's atmospheric evolution.

Bibliography

- Alms, G.R., Burnham, A.K., Flygare, W.H., 1975. Measurement of the dispersion in polarizability anisotropies. *J. Chem. Phys.* 63, 3321–3326. doi:10.1063/1.431821
- Alexandersson, H., 1985. A Simple Stochastic Model of the Precipitation Process. *J. Climate Appl. Meteor.* 24, 1285–1295. doi:10.1175/1520-0450(1985)024<1285:ASSMOT>2.0.CO;2
- Amundson, R., et al., 2008. On the *in situ* aqueous alteration of soils on Mars. *Geochimica et Cosmochimica Acta* 72, 3845–3864. doi:10.1016/j.gca.2008.04.038
- Ballou, E. V., Wood, P. C., Wydeven, T., Lehwalt, M. E., Mack, R.E., 1978. Chemical interpretation of Viking Lander 1 life detection experiment. *Nature* 271, 644–645. doi:10.1038/271644a0
- Baranov, Y.I., Lafferty, W.J., Fraser, G.T., 2004. Infrared spectrum of the continuum and dimer absorption in the vicinity of the O₂ vibrational fundamental in O₂/CO₂ mixtures. *J. Mol. Spectr.* 228, 432–440. doi:10.1016/j.jms.2004.04.010
- Baulch, D.L., et al., 2005. Evaluated Kinetic Data for Combustion Modeling: Supplement II. *J. Phys. Chem. Ref. Data* 34, 757–1397. doi:10.1063/1.1748524

- Baratoux, D., Toplis, M.J., Monnereau, M., Gasnault, O., 2011. Thermal history of Mars inferred from orbital geochemistry of volcanic provinces. *Nature* 472, 338–341. doi:10.1038/nature09903
- Bideau-Mehu, A., Guern, Y., Abjean, R., Johannin-Gilles, A., 1973. Interferometric determination of the refractive index of carbon dioxide in the ultraviolet region. *Opt. Commun.* 9, 432–434. doi:10.1016/0030-4018(73)90289-7
- Black, G., Porter, G., 1962. Vacuum ultra-violet flash photolysis of water vapour. *Proc. R. Soc. London A* 266, 185–197. doi:10.1098/rspa.1962.0055
- Bougher, S.W., Blelly, P.L., Combi, M., Fox, J.L., Mueller-Wodarg, I., Ridley, A., Roble, R.G., 2008. Neutral Upper Atmosphere and Ionosphere Modeling. *Space Science Reviews* 139, 107–141. doi: 10.1007/s11214-008-9401-9
- Boynton, W.V., et al., 2009. Evidence for calcium carbonate at the Mars Phoenix landing site. *Science* 325, 61–64. doi:10.1126/science.1172768
- Brown, L.R., Humphrey, C.M., Gamache, R.R., 2007. CO₂-broadened water in the pure rotation and ν_2 fundamental regions. *J. Mol. Spectr.* 246, 1–21. doi:10.1016/j.jms.2007.07.010

- Bullock, M. A., Stoker, C.R., McKay, C.P., Zent, A.P., 1994. A coupled soil-atmosphere model of H₂O₂ on Mars. *Icarus* 107, 142–154. doi:10.1006/icar.1994.1012
- Bullock, M. A., Moore, J. M., Mellon, M. T., 2004. Laboratory simulations of Mars aqueous geochemistry. *Icarus* 170, 404–423. doi:10.1016/j.icarus.2004.03.016
- Caldwell J., Back, R.A., 1965. Combination reactions of hydroxyl radicals in the flash photolysis of water vapour. *Trans. Faraday Soc.* 61, 1939–1945. doi:10.1039/TF9656101939
- Campbell, I.M., Gray, C.N., 1973. Rate constants for O(³P) recombination and association with N(⁴S). *Chem. Phys. Lett.* 18, 607–609. doi:10.1016/0009-2614(73)80479-8
- Carr, M. H., Head, J. W. III, 2003. Oceans on Mars: An assessment of the observational evidence and possible fate, *JGR*, 108(E5), 5042, doi:10.1029/2002JE001963
- Carr, M., Head, J. W., 2010. Geologic history of Mars. *Earth Planet. Sci. Lett.* 294, 185–203. doi:10.1016/j.epsl.2009.06.042
- Catling, D.C., 1999. A chemical model for evaporites on early Mars: Possible

sedimentary tracers of the early climate and implications for exploration. *JGR* 104, 16453–16470. doi:10.1029/1998JE001020

Catling, D.C., Moore, J.M., 2003. The nature of coarse-grained crystalline hematite and its implications for the early environment of Mars. *Icarus* 165, 277–300. doi:10.1016/S0019-1035(03)00173-8

Chaufray, J.Y., Bertaux, J.L., Leblanc, F., Quémerais, E., 2008. Observation of the hydrogen corona with SPICAM on Mars Express. *Icarus* 195, 598–613. doi:10.1016/j.icarus.2008.01.009

Chapman, S., 1930. A Theory of Upper-Atmospheric Ozone. *Memoirs of the Royal Meteorological Society* 3, 103–125.

Chevrier, V., Mathé, P.-E., Rochette, P., Grauby, O., Bourrié, G., Trolard, F., 2006. Iron weathering products in a CO₂ + (H₂O or H₂O₂) atmosphere: Implications for weathering processes on the surface of Mars. *Geochimica et Cosmochimica Acta* 70, 4295–4317. doi:10.1016/j.gca.2006.06.1368

Clough, S.A., et al., 2005. Atmospheric radiative transfer modeling: a summary of the AER codes. *JQSRT* 91, 233–244. doi:10.1016/j.jqsrt.2004.05.058

- Cockell, C.S., 2000. The ultraviolet history of the terrestrial planets — implications for biological evolution. *Planet. Space Sci.* 48, 203–214. doi: 10.1016/S0032-0633(99)00087-2
- Colaprete, A., Toon, O.B., 2003. Carbon dioxide clouds in an early dense Martian atmosphere. *JGR* 108, 5025. doi:10.1029/2002JE001967
- Corrêa, M.P., Souza, R.A.F., Ceballos, J.C., Fomin, B., 2005. Preliminary results of simulations of a user-friendly fast line-by-line computer code for simulations of satellite signal. *Anais XII Simpósio Brasileiro de Sensoriamento Remoto, Goiânia, Brasil, INPE*, 363–370.
- Craddock, R.A., Howard, A.D., 2002. The case for rainfall on a warm, wet early Mars. *JGR* 107(E11), 5111. doi:10.1029/2001JE001505
- Craddock, R.A., Greeley, R., 2009. Minimum estimates of the amount and timing of gases released into the martian atmosphere from volcanic eruptions. *Icarus* 204, 512–526. doi:10.1016/j.icarus.2009.07.026
- Daescu, D., Sandu, A., Carmichael, G.R., 2003. Direct and Adjoint Sensitivity Analysis of Chemical Kinetic Systems with KPP: II – Validation and Numerical Experiments, *Atmospheric Environment* 37, 5097–5114. doi:10.1016/j.atmosenv.2003.08.020

Damian, V., Sandu, A., Damian, M., Potra, F., Carmichael, G.R., 2002. The Kinetic PreProcessor KPP – A Software Environment for Solving Chemical Kinetics. *Computers and Chemical Engineering* 26, 1567–1579. doi:10.1016/S0098-1354(02)00128-X

Dorofeeva, O., Iorish, V. S., Novikov, V. P., Neumann, D. B., 2003. NIST-JANAF Thermochemical Tables. II. Three molecules related to atmospheric chemistry: HNO₃, H₂SO₄, and H₂O₂. *J. Phys. Chem. Ref. Data* 32, 879–901. doi:10.1063/1.1547435

Drever, J.I., 1997. *The Geochemistry of Natural Waters: Surface and Groundwater Environments*. 3rd edition. Upper Saddle River, NJ: Prentice Hall.

Eastman, E. D., 1929. Specific heats of gases at high temperatures. Tech. Paper 445, Bureau of Mines.

Encrenaz, T., Greathouse, T.K., Lefevre, F., Atreya, S.K., 2011. Hydrogen peroxide on Mars: Observations, interpretation and future plans. *Planet. Space Sci.* 68, 3–17. doi:10.1016/j.pss.2011.03.019

Feldman, P. D., et al., 2011. *Rosetta*-Alice observations of exospheric hydrogen and

oxygen on Mars. *Icarus* 214, 394–399. doi:10.1016/j.icarus.2011.06.013

Forget, F., Pierrehumbert, R.T., 1997. Warming early Mars with carbon dioxide clouds that scatter infrared radiation. *Science* 278, 1273–1276. doi:10.1126/science.278.5341.1273

Forster, P. M. de F., K. P. Shine, 1997. Radiative forcing and temperature trends from stratospheric ozone changes. *JGR* 102(D9), 10841–10855. doi:10.1029/96JD03510

Forster, P. M., et al., 2011. Evaluation of radiation scheme performance within chemistry climate models. *JGR* 116, D10302. doi:10.1029/2010JD015361

Fox, J.L., 2003. Effect of H₂ on the Martian ionosphere: Implications for atmospheric evolution. *JGR* 108(A6), 1223. doi:10.1029/2001JA000203

Fox, J.L., Hać, A.B., 2009. Photochemical escape of oxygen from Mars: A comparison of the exobase approximation to a Monte Carlo method. *Icarus* 204, 527–544. doi:10.1016/j.icarus.2009.07.005

François, L.M., Gérard, J.C., 1988. Ozone, climate and biospheric environment in the ancient oxygen-poor atmosphere. *Planet. Space Sci.* 36, 1391–1414. doi:0.1016/0032-0633(88)90007-4

- Fray, N., Schmitt, B., 2009. Sublimation of ices of astrophysical interest: A bibliographic review. *Plan. Space Sci.* 57, 2053–2080. doi:10.1016/j.pss.2009.09.011
- Gavhane, K.A., 2006. *Chemical Reaction Engineering II*. Nirali Prakashan.
- Gellert, R., et al., 2004. Chemistry of Rocks and Soils in Gusev Crater from the Alpha Particle X-ray Spectrometer. *Science* 305, 829–832. doi:10.1126/science.1099913
- Gellert, R., et al., 2006. Alpha Particle X-Ray Spectrometer (APXS): Results from Gusev crater and calibration report. *JGR* 111, E02S05. doi:10.1029/2005JE002555
- Giguère, P.A., Liu, I.D., Dugdale, J.S., Morrison, J.A., 1954. Hydrogen Peroxide: The Low Temperature Heat Capacity of the Solid and Third Law of Entropy. *Can. J. Chem.* 32, 117–128. doi:10.1139/v54-019
- Giorgi, F., Chameides, W.L., 1985. The rainout parameterization in a photochemical model. *JGR* 90(D5), 7872–7880. doi:10.1029/JD090iD05p0787
- Golombek, M. P., et al., 2006. Erosion rates at the Mars Exploration Rover landing sites and long-term climate change on Mars. *JGR* 111, E12S10. doi:10.1029/2006JE002754

- Gooding, J.L., 1978. Chemical weathering on Mars. *Icarus* 33, 483–513.
doi:10.1016/0019-1035(78)90186-0
- Greeley, R., Schneid, B., 1991. Magma generation on Mars – Amounts, rates, and comparisons with earth, moon, and Venus. *Science* 254, 996–998.
doi:10.1126/science.254.5034.996
- Grott, M., Morschhauser, A., Breuer, D., Hauber, E., 2011. Volcanic outgassing of CO₂ and H₂O on Mars. *Earth Planet. Sci. Lett.* 308, 391–400.
doi:10.1016/j.epsl.2011.06.014
- Gruszka, M., Borysow, A., 1998. Computer simulation of the far infrared collision induced absorption spectra of gaseous CO₂. *Mol. Phys.* 93, 1007–1016.
doi:10.1080/002689798168709
- Halvey, I., Zuber, M.T., Schrag, D.P., 2007. A Sulfur Dioxide Climate Feedback on Early Mars. *Science* 318, 1903–1907. doi:10.1126/science.1147039
- Halevy, I., Pierrehumbert, R. T., and Schrag, D. P., 2009. Radiative transfer in CO₂-rich paleoatmospheres. *JGR* 114, D18112. doi:10.1029/2009JD011915

- Hanisch, F., Crowley, J.N., 2003. Ozone decomposition on Saharan dust: an experimental investigation. *Atmos. Chem. Phys.* 3, 119–130. doi:10.5194/acp-3-119-2003
- Hauglustaine, D.A., Granier, C., Brasseur, G.P., Mégie, G., 1994. The importance of atmospheric chemistry in the calculation of radiative forcing on the climate system. *JGR* 99(D1), 1173–1186. doi:10.1029/93JD02987
- Hirschmann, M.M., Withers, A.C., 2008. Ventilation of CO₂ from a reduced mantle and consequences for the early Martian greenhouse. *Earth Plan. Sci. Lett.* 270, 147–155. doi:10.1016/j.epsl.2008.03.034
- Hiscox, J.A., Lindner, B.L., 1997. Ozone and planetary habitability. *Journal of the British Interplanetary Society* 50, 109–114.
- Holland, H. D., 1962. Model for the evolution of the Earth's atmosphere. *Petrologic Studies: A Volume in Honor of AF Buddington* 30, 726-732.
- Huang, D., Chen, Z., 2010. Reinvestigation of the Henry's law constant for hydrogen peroxide with temperature and acidity variation. *J. Env. Sci.* 22, 570–574. doi:10.1016/S1001-0742(09)60147-9
- Hausrath, E.M., Navarre-Sitchler, A.K., Sak, P.B., Steefel, C.I., Brantley, S.L., 2008.

Basalt weathering rates on Earth and the duration of liquid water on the plains of Gusev Crater, Mars. *Geology* 36, 67–70. doi:10.1130/G24238A.1

Hunten, D., 1993. Atmospheric Evolution of the Terrestrial Planets. *Science* 259, 915–920. doi:10.1126/science.259.5097.915

Hurowitz, J.A., McLennan, S.M., 2007. A ~ 3.5 Ga record of water-limited, acidic weathering conditions on Mars. *Earth and Plan. Sci. Let.* 260, 432–443. doi:10.1016/j.epsl.2007.05.043

Inn, E.C.Y., 1974. Rate of recombination of oxygen atoms and CO at temperatures below ambient. *J. Chem. Phys.* 61, 1589–1590. doi:10.1063/1.1682139

Ivanov, B.A., 2001. Mars/Moon Cratering Rate Ratio Estimates. *Space Sci. Rev.* 96, 87–104. doi:10.1023/A:1011941121102

Jakosky, B.M., Shock, E.L., 1998. The biological potential of Mars, the early Earth, and Europa. *JGR* 103(E8), 19359–19364. doi:10.1029/98JE01892

Jamieson, C., Garcia, R.M., Pejakovic, D.A., Kalogerakis, K.S., 2009. Oxygen Atom Recombination in Carbon Dioxide Atmospheres. American Astronomical Society, DPS meeting #41, #54.01.

- Johnson, R.E., Combi, M.R., Fox, J.L., Ip, W.H., Leblanc, F., McGrath, M.A., Shematovich, V.I., Strobel, D.F., Waite, J.H., 2008. Exospheres and Atmospheric Escape. *Space Science Reviews* 139, 355–397. doi:10.1007/s11214-008-9415-3
- Johnson, S.S., Mischna, M.A., Grove, T.L., Zuber, M.T., 2008. Sulfur-induced greenhouse warming on Early Mars. *JGR* 113, E08005. doi:10.1029/2007JE002962
- Johnson, S.S., Pavlov, A.A., Mischna, M.A., 2009. Fate of SO₂ in the ancient Martian atmosphere: Implications for transient greenhouse warming. *JGR* 114, E11011. doi:10.1029/2008JE003313
- Kaplan, L.D., Münch, G., Spinrad, H., 1964. An Analysis of the Spectrum of Mars. *Astrophysical Journal* 139, 1–15. doi: 10.1086/147736
- Kasting, J.F., Liu, S.C., Donahue, T.M., 1979. Oxygen Levels in the Prebiological Atmosphere. *JGR* 84(C6), 3097–3107. doi:10.1029/JC084iC06p03097
- Kasting, J.F., Donahue, T.M., 1980. The Evolution of Atmospheric Ozone. *JGR* 85(C6), 3255–3263. doi:10.1029/JC085iC06p03255
- Kasting, J. F., Walker, J.C.G., 1981. Limits on Oxygen Concentration in the Prebiological

Atmosphere and the Rate of Abiotic Fixation of Nitrogen. *JGR* 86(C2), 1147–1158.
doi:10.1029/JC086iC02p01147

Kasting, J. F., Holland, H.D., Pinto, J.P., 1985. Oxidant Abundances in Rainwater and the Evolution of Atmospheric Oxygen. *JGR* 90(D6), 10497–10510.
doi:10.1029/JD090iD06p10497

Kasting, J. F., 1991. CO₂ Condensation and the Climate of Early Mars. *Icarus* 94, 1–13.
doi:10.1016/0019-1035(91)90137-I

Kasting, J.F., 1995. O₂ concentrations in dense primitive atmospheres: commentary. *Planet. Space Sci.* 43, 11–13. doi:10.1016/0032-0633(94)00203-4

Kasting, J.F., 1997. Warming Early Earth and Mars. *Science* 276, 1213–1215.
doi:10.1126/science.276.5316.1213

Kelly, N. J., et al., 2006. Seasonal polar carbon dioxide frost on Mars: CO₂ mass and columnar thickness distribution. *JGR* 111, E03S07. doi:10.1029/2006JE002678

Kiefer, W.S., 2003. Melting in the Martian mantle: Shergottite formation and implications for present-day mantle convection on Mars. *Meteor. Planet. Sci.* 38, 1815–1832.
doi:10.1111/j.1945-5100.2003.tb00017.x

Kiehl, J.T., Trenberth, K.E., 1997. Earth's Annual Global Mean Energy Budget. Bull. Amer. Meteor. Soc., 78, 197–208. doi:10.1175/1520-0477(1997)078%3C0197:EAGMEB%3E2.0.CO;2

King, M.B., Al-Najjar, H., 1974. A method for correlating and extending vapour pressure data to lower temperatures using thermal data: Vapour pressure equations for some n-alkanes at temperatures below the normal boiling point. Chem. Eng. Sci. 29, 1003–1011. doi:10.1016/0009-2509(74)80092-8

Klingelhöfer, G.R.D.S., et al., 2004. Jarosite and hematite at Meridiani Planum from Opportunity's Mössbauer spectrometer. Science 306, 1740–1745. doi:10.1126/science.1104653

Kong, T.Y., McElroy, M.B., 1977. The global distribution of O₃ on mars. Planet. Space Sci. 25, 839–857. doi:10.1016/0032-0633(77)90038-1

Krasnopolsky, V.A., 1993. Photochemistry of the Martian Atmosphere (Mean Conditions). Icarus 110, 313–332. doi:10.1006/icar.1993.1027

Krasnopolsky, V.A., 1995. Uniqueness of a solution of a steady state photochemical problem: Applications to Mars. JGR 100(E2), 3263–3276. doi:10.1029/94JE03283

Krasnopolsky, V.A., 2003. Mars Photochemistry: Weak Points and Search for Solutions. Sixth International Conference on Mars: #3002. <http://www.lpi.usra.edu/meetings/sixthmars2003/pdf/3002.pdf>

Krasnopolsky, V.A., 2006. Photochemistry of the martian atmosphere: Seasonal, latitudinal, and diurnal variations. *Icarus* 185, 153–170. doi:10.1016/j.icarus.2006.06.003

Krasnopolsky, V.A., Feldman, P.D., 2001. Detection of Molecular Hydrogen in the Atmosphere of Mars. *Science* 294, 1914–1917. doi:10.1126/science.1065569

Kuntz, M., Höpfner, M., 1999. Efficient line-by-line calculation of absorption coefficients. *JQSRT* 63, 97–114. doi:10.1016/S0022-4073(98)00140-X

Kurucz R.L., 1992. Synthetic infrared spectra in infrared solar physics. In: Rabin D.M., Jefferies J.T., (Eds.), *IAU Symposium*, 154. Kluwer Academic Press, Norwell, MA.

Lammer, H., Lichtenegger, H.I.M., Kolb, C., Ribas, I., Guinan, E.F., Abart, R., Bauer, S.J., 2003. Loss of water from Mars: Implications for the oxidation of the soil. *Icarus* 165, 9–25. doi:10.1016/S0019-1035(03)00170-2

- Lebonnois, S., Hourdin, F., Eymet, V., Crespin, A., Fournier, R., Forget, F., 2010. Superrotation of Venus' atmosphere analyzed with a full general circulation model. JGR 115, E06006. doi:10.1029/2009JE003458.
- Lederberg, J., Sagan, C., 1963. Microenvironments for Life on Mars. PNAS 48, 1473–1475. doi: 10.1073/pnas.48.9.1473
- Lefèvre, F., Lebonnois, S., Montmessin, F., Forget, F., 2004. Three-dimensional modeling of ozone on Mars. JGR 109, E07004. doi:10.1029/2004JE002268
- Lemmon, E.W., Huber, M.L., McLinden, M.O., 2010. NIST Standard Reference Database 23: Reference Fluid Thermodynamic and Transport Properties-REFPROP, Version 9.0, National Institute of Standards and Technology, Standard Reference Data Program, Gaithersburg.
- Letchworth, K., Benner, D., 2007. Rapid and accurate calculation of the Voigt function. JQSRT 107, 173–192. doi:10.1016/j.jqsrt.2007.01.052
- Levy, H., 1971. Normal Atmosphere: Large Radical and Formaldehyde Concentrations Predicted. Science 173, 141–143. doi:10.1126/science.173.3992.141
- Li, H., Ji, X., Yan, J., 2006. A new modification on RK EOS for gaseous CO₂ and gaseous

mixtures of CO₂ and H₂O. *Int. J. Energy Res.* 30, 135–148. doi:10.1002/er.1129

Liang, M.C., Hartman, H., Kopp, R.E., Kirschvink, J.L., Yung, Y.L., 2006. Production of hydrogen peroxide in the atmosphere of the Snowball Earth and the origin of oxygenic photosynthesis. *PNAS* 103, 18896–18899. doi:10.1073/pnas.0608839103

Lindner, B. L., 1988. Ozone on Mars: The effects of clouds and airborne dust. *Planet. Space Sci.* 36, 125–144. doi:10.1016/0032-0633(88)90049-9

Lindzen, R. S., 1981. Turbulence and stress owing to gravity wave and tidal breakdown. *JGR* 86(C10), 9707–9714. doi:10.1029/JC086iC10p09707

Liou, KN., 2002. *An introduction to atmospheric radiation*. 2nd ed., Academic Press. p. 126

López-Valverde, M., Edwards, D., López-Puertas, M., Roldán, C., 1998. Non-local thermodynamic equilibrium in general circulation models of the Martian atmosphere 1. Effects of the local thermodynamic equilibrium approximation on thermal cooling and solar heating. *JGR* 103, 16799–16811. doi:10.1029/98JE01601

Mackwell, S. J., 1992. Oxidation kinetics of fayalite (Fe₂SiO₄). *Phys. Chem. Min.* 19, 220–228. doi:10.1007/BF00202311

- Manatt, S.L., Manatt, M.R.R., 2004. On the Analyses of Mixture Vapor Pressure Data: The Hydrogen Peroxide/Water System and Its Excess Thermodynamic Functions. *Chemistry* 10, 6540–6557. doi:10.1002/chem.200400104
- Manga, M., Patel, A., Dufek, J., Kite, E.S., 2012. Wet surface and dense atmosphere on early Mars suggested by the bomb sag at Home Plate Mars. *Geophys. Res. Lett.* 39, L01202. doi:10.1029/2011GL050192
- Marion, G.M., Catling, D.C., Kargel, J.S., 2003. Modeling aqueous ferrous iron chemistry at low temperatures with application to Mars. *Geochimica et Cosmochimica Acta* 67, 4251–4266. doi:10.1016/S0016-7037(03)00372-7
- Marion, G.M., Kargel, J.S., Catling, D.C., 2008. Modeling ferrous–ferric iron chemistry with application to martian surface geochemistry. *Geochimica et Cosmochimica Acta*, Volume 72, 242–266. doi:10.1016/j.gca.2007.10.012
- Marion, G.M., Mironenko, M.V., Roberts, M.W., 2010. FREZCHEM: A geochemical model for cold aqueous solutions. *Computers & Geosciences* 36, 10–15. doi:10.1016/j.cageo.2009.06.004
- Mari, C., Jacob, D.J., Bechtold, P., 2000. Transport and scavenging of soluble gases in a

deep convective cloud. *JGR* 105(D17), 22,255–22,267. doi:10.1029/2000JD900211

Massie, S.T., Hunten, D. M., 1981. Stratospheric eddy diffusion coefficients from tracer data. *JGR* 86(C10), 9859–9868. doi:10.1029/JC086iC10p09859

Matsubara, Y., Howard, A.D., Drummond, S.A., 2011. Hydrology of early Mars: Lake basins. *JGR* 116, E04001. doi:10.1029/2010JE003739

McCubbin, M.F., et al., 2012. Hydrous melting of the martian mantle produced both depleted and enriched shergottites. *Geology* 40, 683–686. doi:10.1130/G33242.1

McElroy, M.B., Donahue, T.M., 1972. Stability of the Martian atmosphere. *Science* 177, 986–988. doi:10.1126/science.177.4053.986

McSween, H.Y., Keil, K., 2000. Mixing relationships in the Martian regolith and the composition of globally homogeneous dust. *Geochimica et Cosmochimica Acta* 64, 2155–2166. doi:10.1016/S0016-7037(99)00401-9

Meadows, V. S., Crisp, D., 1996. Ground-based near-infrared observations of the Venus nightside: The thermal structure and water abundance near the surface. *JGR* 101(E2), 4595–4622. doi:10.1029/95JE03567

- Michalski, J.R., Niles, P.B., 2010. Deep crustal carbonate rocks exposed by meteor impact on Mars. *Nature Geoscience*, 751–755. doi:10.1038/ngeo971
- Millero, F.J., Izaguirre, M., 1989. Effect of ionic strength and ionic interactions on the oxidation of Fe(II). *J. Sol. Chem.* 18, 585–599. doi:10.1007/BF00664239
- Millero, F.J., Sotolongo, S., 1989. The oxidation of Fe(II) with H₂O₂ in seawater. *Geochimica et Cosmochimica Acta* 53, 1867–1873. doi:10.1016/0016-7037(89)90307-4
- Minschwaner, K., Anderson, G.P., Hall, L.A., Yoshino, K. 1992. Polynomial coefficients for calculating O₂ Schumann-Runge cross sections at 0.5 cm⁻¹ resolution. *JGR* 97(D9), 10103–10108. doi: 10.1029/92JD00661
- Mischna, M.A., Kasting, J.F., Pavlov, A., Freedman, R., 2000. Influence of carbon dioxide clouds on early martian climate. *Icarus* 145, 546–554. doi:10.1006/icar.2000.6380
- Mitchell, T.D., Jones, P.D., 2005. An improved method of constructing a database of monthly climate observations and associated high-resolution grids. *International journal of climatology* 25, 693–712. doi:10.1002/joc.1181

- Montmessin, F., et al., 2006. Subvisible CO₂ ice clouds detected in the mesosphere of Mars. *Icarus* 183, 403–410. doi:10.1016/j.icarus.2006.03.015
- Montmessin, F., et al., 2011. A layer of ozone detected in the nightside upper atmosphere of Venus. *Icarus* 216, 82–85. doi:10.1016/j.icarus.2011.08.010
- Mousavipour, S.H., Saheb, V., 2007. Theoretical study on the kinetic and mechanism of H+HO₂ reaction. *Bull. Chem. Soc. Jpn.* 80, 1901–1913. doi:10.1246/bcsj.80.1901
- Morgan, B., Lahav, O., 2007. The effect of pH on the kinetics of spontaneous Fe(II) oxidation by O₂ in aqueous solution – basic principles and a simple heuristic description. *Chemosphere* 68, 2080–2084. doi:10.1016/j.chemosphere.2007.02.015
- Nair, H., Allen, M., Anbar, A.D., Yung, Y.L., Clancy, R.T., 1994. A Photochemical Model of the Martian Atmosphere. *Icarus* 111, 124–150. doi:10.1006/icar.1994.1137
- Neu, J.L., Prather, M.J., 2012. Toward a more physical representation of precipitation scavenging in global chemistry models: cloud overlap and ice physics and their impact on tropospheric ozone. *Atmos. Chem. Phys.* 12, 3289–3310. doi:10.5194/acp-12-3289-2012
- Neukum, G., et al., 2010. The geologic evolution of Mars: Episodicity of resurfacing

events and ages from cratering analysis of image data and correlation with radiometric ages of Martian meteorites. *Earth Planet. Sci. Lett.* 294, 204–222. doi:10.1016/j.epsl.2009.09.006

Oki, T., Kanae, S., 2006. Global Hydrological Cycles and World Water Resources. *Science* 313, 1068–1072. doi:10.1126/science.1128845

Old, J.G., Gentili, K.L., Peck, E.R., 1971. Dispersion of Carbon Dioxide. *J. Opt. Soc. Am.* 61, 89–90. doi:10.1364/JOSA.61.000089

O'Neill, C., Lenardic, A., Jellinek, A.M., Kiefer, W.S., 2007. Melt propagation and volcanism in mantle convection simulations, with applications for Martian volcanic and atmospheric evolution. *JGR* 112, E07003. doi:10.1029/2006JE002799

Orkin, V.L., Kozlov, S.N., Poskrebyshev, G.A., Kurylo, M.J., 2006. Rate Constant for the Reaction of OH with H₂ between 200 and 480 K. *J. Phys. Chem.* 110, 6978–6985. doi:10.1021/jp057035b

Parkinson, T.D., Hunten, D.M., 1972. Spectroscopy and Aeronomy of O₂ on Mars. *J. Atm. Sci.* 29, 1380–1390. doi:10.1175/1520-0469(1972)029%3C1380:SAOOO%3E2.0.CO;2

- Perriat, P., Domenichini, B., Gillot, B., 1996. A model for oxidation in finely divided ferrites taking into account the stresses generated during reaction. *J. Phys. Chem. Sol.* 57, 1641–1652. doi:10.1016/0022-3697(96)00055-8
- Perrin, M.Y., Hartmann, J.M., 1989. Temperature-dependent measurements and modeling of absorption by CO₂-N₂ mixtures in the far line-wings of the 4.3- μ m CO₂ band. *JQSRT* 42, 311–317. doi:10.1016/0022-4073(89)90077-0
- Plaut, J.J., et al., 2007. Subsurface Radar Sounding of the South Polar Layered Deposits of Mars. *Science* 316, 92–95. doi:10.1126/science.1139672
- Pollack, J.B., Kasting, J.F., Rochardson, S.M., Poliakoff, K., 1987. The case for a wet, warm climate on early Mars. *Icarus* 71, 203–224. doi:10.1016/0019-1035(87)90147-3
- Popova, O., Nemtchinov, I., Hartmann, W. K., 2003. Bolides in the present and past martian atmosphere and effects on cratering processes. *Meteor. & Planet. Sci.* 38, 905–925. doi:10.1111/j.1945-5100.2003.tb00287.x
- Pradhan, M., Kyriakou, G., Archibald, A.T., Papageorgiou, A.C., Kalberer, M., Lambert, R.M., 2010. Heterogeneous uptake of gaseous hydrogen peroxide by Gobi and Saharan dust aerosols: a potential missing sink for H₂O₂ in the troposphere. *Atmos.*

Chem. Phys 10, 7127–7136. doi:10.5194/acp-10-7127-2010

Quine, B.M., and Drummond, J.R., 2002. GENSPECT: a line-by-line code with selectable interpolation error tolerance. JQSRT 74, 147–165. doi:10.1016/S0022-4073(01)00193-5

Rieder, R., et al., 1997. The Chemical Composition of Martian Soil and Rocks Returned by the Mobile Alpha Proton X-ray Spectrometer: Preliminary Results from the X-ray Mode. Science 278, 1771–1774. doi:10.1126/science.278.5344.1771

Rieder, R., et al. 2004. Chemistry of rocks and soils at Meridiani Planum from the Alpha Particle X-ray Spectrometer. Science 306, 1746-1749. doi:10.1126/science.1104358

Rienecker, M.M., et al., 2011. MERRA - NASA's Modern-Era Retrospective Analysis for Research and Applications. J. Climate 24, 3624–3648. doi:10.1175/JCLI-D-11-00015.1

Ribas, I., et al., 2010. Evolution of the Solar Activity Over Time and Effects on Planetary Atmospheres. II. κ^1 Ceti, an Analog of the Sun when Life Arose on Earth. Astrophys. J. 714, 384–395. doi:10.1088/0004-637X/714/1/384

- Richardson, M.I., Mischna, M.A., 2005. Long-term evolution of transient liquid water on Mars. *JGR* 110, E03003. doi:10.1029/2004JE002367
- Robbins, S.J., Achille, G.D., Hynek, B.M., 2011. The volcanic history of Mars: High-resolution crater-based studies of the calderas of 20 volcanoes. *Icarus* 211, 1179–1203. doi:10.1016/j.icarus.2010.11.012
- Rothman, L.S., et al., 2009. The HITRAN 2008 molecular spectroscopic database. *JQSRT* 110, 533–572. doi:10.1016/j.jqsrt.2009.02.013
- Rosenqvist, J., Chassefière, E., 1995. Inorganic chemistry of O₂ in a dense primitive atmosphere. *Planet. Space Sci.* 43, 3–10. doi:10.1016/0032-0633(94)00202-3
- Sander S.P., et al., 2011. Chemical Kinetics and Photochemical Data for Use in Atmospheric Studies, Evaluation Number 17, JPL Publication 10-6, Jet Propulsion Laboratory, Pasadena, CA.
- Sandu, A., Daescu, D., Carmichael, G.R., 2003. Direct and Adjoint Sensitivity Analysis of Chemical Kinetic Systems with KPP: I – Theory and Software Tools, *Atmospheric Environment* 37, 5083–5096. doi:10.1016/j.atmosenv.2003.08.019
- Satoh, M., 2004. Atmospheric Circulation Dynamics and General Circulation Models.

Springer-Praxis, p. 378

Satterfield, C.N., Stein, T.W., 1957. Decomposition of Hydrogen Peroxide Vapor on Relatively Inert Surfaces. *Ind. Eng. Chem.* 49, 1173–1180. doi:10.1021/ie50571a042

Seguin, M., 1966. Instability of FeCO_3 in air. *AJS* 264, 562–568. doi:10.2475/ajs.264.7.562

Segura, A., Navarro-González R., 2005. Nitrogen fixation on early Mars by volcanic lightning and other sources. *Geophys. Res. Lett.*, 32, L05203, doi:10.1029/2004GL021910

Segura, A., Meadows, V. S., Kasting, J. F., Crisp, D., Cohen, M., 2007. Abiotic formation of O_2 and O_3 in high- CO_2 terrestrial atmospheres. *A&A* 472, 665–679. doi:10.1051/0004-6361:20066663

Selsis, F., Despois, D., Parisot, J.-P., 2002. Signature of life on exoplanets: Can Darwin produce false positive detections? *A&A* 388, 985–1003. doi:10.1051/0004-6361:20020527

Schumb, W.C., Satterfield, C.N., Wentworth, R.L., 1955. Hydrogen Peroxide. American Chemical Society Monograph No. 128.

- Shackelford, C.D., Daniel, D.E., 1991. Diffusion In Saturated Soil I. Background. *J. Geotech. Eng.* 117, 467–484. doi:10.1061/(ASCE)0733-9410(1991)117:3(467)
- Sidhu, P.S., Gilkes, R.J., Posner, A.M., 1977. Mechanism of the low temperature oxidation of synthetic magnetites. *J. Inorg. Nucl. Chem.* 39, 1953–1958. doi:10.1016/0022-1902(77)80523-X
- Sigg, A., Staffelbach, T., Neftel, A., 1992. Gas phase measurements of hydrogen peroxide in Greenland and their meaning for the interpretation of H₂O₂ records in ice cores. *J. Atm. Chem.* 14, 223–232. doi:10.1007/BF00115235
- Smith, G.P., Robertson, R., 2008. Temperature dependence of oxygen atom recombination in nitrogen after ozone photolysis. *Chem. Phys. Lett.* 458, 6–10. doi:10.1016/j.cplett.2008.04.074
- Span, R., Wagner, W., J., 1996. A New Equation of State for Carbon Dioxide Covering the Fluid Region from the Triple-Point Temperature to 1100 K at Pressures up to 800 MPa. *Phys. Chem. Ref. Data* 25, 1509–11596. doi:10.1063/1.555991
- Stanley, B.D., Hirschmann, M.M., Withers, A.C., 2011. CO₂ solubility in Martian basalts and Martian atmospheric evolution. *Geochimica et Cosmochimica Acta*, 75, 5987–

6003. doi:10.1016/j.gca.2011.07.027

Stock, J.W., et al., 2012. Chemical pathway analysis of the Martian atmosphere: CO₂-formation pathways. *Icarus* 219, 13–24. doi:10.1016/j.icarus.2012.02.010

Stocker, D.W., Burchardt, M.P., Plooster, M., Stedman, D.H., 1987. Continuous eddy-correlation dry deposition flux measurements. Rosmead, CA: Final Rep. Western Energy. Supply and Transmissions Assoc.

Strom, R.G., Croft, S.K., Barlow, N.G., 1992. The Martian Impact Cratering Record in Mars, H.H. Kieffer et al., Eds. Tucson, AZ: University of Arizona Press.

Sutter, B., Dalton, J.B., Ewing, S.A., Amundson, R., McKay, C.P., 2007. Terrestrial analogs for interpretation of infrared spectra from the Martian surface and subsurface: Sulfate, nitrate, carbonate, and phyllosilicate-bearing Atacama Desert soils. *JGR* 112(G4), G04S10. doi:10.1029/2006JG000313

Squyres, S.W., Kasting, J.F., 1994. Early Mars: How Warm and How Wet? *Science* 265, 744–749. doi:10.1126/science.265.5173.744

Tang, J., Myers, M., Bosnick, K.A., Brus, L.E., 2003. Magnetite Fe₃O₄ nanocrystals: spectroscopic observation of aqueous oxidation kinetics. *J. Phys. Chem. B* 107(30),

7501–7506. doi:10.1021/jp027048e

Tian, F., Claire, M.W., Haqq-Misra, J.D., Smith, M., Crisp, D.C., Catling, D., Zahnle, K., Kasting, J.F., 2010. Photochemical and climate consequences of sulfur outgassing on early Mars. *Earth Planet. Sci. Lett.* 295, 412–418. doi:10.1016/j.epsl.2010.04.016

Tonkov, M.V., et al., 1996. Measurements and empirical modeling of pure CO₂ absorption in the 2.3- μ m region at room temperature: Far wings, allowed and collision-induced bands. *Appl. Opt.* 35, 4863–4870. doi:10.1364/AO.35.004863

Toon, O.B., McKay, C.P., Ackerman, T.P., Santhanam, K., 1989. Rapid calculation of radiative heating rates and photodissociation rates in inhomogeneous multiple scattering atmospheres. *JGR* 94(D13), 16287–16301. doi:10.1029/JD094iD13p16287

Tosca, N.J., et al., 2005. Geochemical modeling of evaporation processes on Mars: Insight from the sedimentary record at Meridiani Planum. *Earth Planet. Sci. Lett.* 240, 122–148. doi:10.1016/j.epsl.2005.09.042

Tvorogov, S.D, Rodimova, O.B., Nesmelova, L.I., 2005. On the correlated *k*-distribution approximation in atmospheric calculations. *Opt. Eng.* 44, 071202. doi:10.1117/1.1955318

- Vaille, A., Bougher, S.W., Tenishev, V., Combi, M.R., Nagy, A.F., 2010. Water loss and evolution of the upper atmosphere and exosphere over martian history. *Icarus* 206, 28–39. doi:10.1016/j.icarus.2009.04.036
- Walkauskas, L.P., Kaufman, F., 1975. Gas phase hydrogen atom recombination. Symposium (International) on Combustion 15, 691–699. doi:10.1016/S0082-0784(75)80339-0
- Wells, R.J., 1999. Rapid approximation to the Voigt/Faddeeva function and its derivatives. *JQSRT* 64, 29–48. doi:10.1016/S0022-4073(97)00231-8
- Wordsworth, R., Forget, F., Eymet, V., 2010a. Infra-red collision-induced and far-line absorption in dense CO₂ atmospheres. *Icarus* 210, 992–997. doi:10.1016/j.icarus.2010.06.010
- Wordsworth, R., Forget, F., Selsis, F., Madeleine, J.-B., Millour, E., Eymet, V., 2010b. Is Gliese 581d habitable? Some constraints from radiative-convective climate modeling. *A&A* 522, A22. doi:10.1051/0004-6361/201015053
- Wray, J.J., et al., 2011. Evidence for regional deeply buried carbonate-bearing rocks on Mars. Lunar and Planetary Science Conference XLII: #2635. <http://www.lpi.usra.edu/meetings/lpsc2011/pdf/2635.pdf>

Yung Y. L., Nair H., Gerstell M. F., 1997. CO₂ Greenhouse in the Early Martian Atmosphere: SO₂ Inhibits Condensation. *Icarus* 130, 222–224. doi:10.1006/icar.1997.5808

Zahnle, K. J., Haberle, R. M., Catling, D. C., Kasting, J. F., 2008. Photochemical instability of the ancient Martian atmosphere. *JGR* 113, E11004. doi:10.1029/2008JE003160

Zellner, R., Erlen, K., Field, D., 1977. Kinetics of the Recombination Reaction $\text{OH} + \text{H} + \text{M} \rightarrow \text{H}_2\text{O} + \text{M}$ at Low Temperatures. *Symp. Int. Combust. Proc.* 16, 939–948. doi:10.1016/S0082-0784(77)80386-X

Zent, A., 1997. The Role of Impact Gardening in Disturbing the Oxidation Stratigraphy of the Martian Regolith. *Lunar and Planetary Science XXVIII*: #1776. <http://www.lpi.usra.edu/meetings/lpsc97/pdf/1776.PDF>

Zent, A., 1998. On the thickness of the oxidized layer of the Martian regolith. *JGR* 103(E13), 31491–31498. doi:10.1029/98JE01895

Zhao, Y., Chen, Z., Shen, X., Zhang, X., 2011. Kinetics and Mechanisms of Heterogeneous Reaction of Gaseous Hydrogen Peroxide on Mineral Oxide Particles.

Environ. Sci. Technol. 45, 3317–3324. doi:10.1021/es104107c

Appendix A: Heat Capacity of CO₂

In order to calculate the tropospheric lapse rate, the specific heat capacity c_p of the atmosphere is required, which in this case is dominated by CO₂. From a theoretical standpoint, CO₂ is well approximated as a rigidly rotating linear molecule with internal vibrational modes. Applying statistical mechanics, its zero-pressure heat capacities may then be written as

$$\frac{c_p}{R} = 1 + \frac{c_v}{R} = 1 + \frac{3}{2} + \frac{2}{2} + \sum_j \left(\frac{\theta_j}{T} \right)^2 \frac{e^{-\frac{\theta_j}{T}}}{\left(1 - e^{-\frac{\theta_j}{T}} \right)^2} \quad (\text{A.1})$$

where R is the universal gas constant, T is the gas temperature, and θ_j is the characteristic temperature of the j th vibrational mode. Since relatively low planetary temperatures are of interest here ($T < 373$ K) only the lowest few vibrational modes need to be considered: the symmetric stretch mode $\nu_1 = 1330 \text{ cm}^{-1}$ ($\theta_1 = 1910$ K) and the doubly degenerate bending mode $\nu_2 = 667 \text{ cm}^{-1}$ ($\theta_2 = 960$ K). The asymmetric stretch mode $\nu_3 = 2349 \text{ cm}^{-1}$ ($\theta_3 = 3380$ K) is inactive at the temperatures of interest. For $T < 373$ K, Eq. (A.1) produces zero-pressure c_p values in excellent agreement ($< 0.1\%$ difference) with the values generated by the NIST REFPROP program v9.0 (Lemmon 2010), (see Fig. A.1). This software uses a complex CO₂ equation of state (EOS) from Span & Wagner (1996) and was derived from a thorough review of experimental data. For $T > 140$ K the theoretical model is also in good agreement with the c_p parameterization derived from the

temperature structure of the Venusian atmosphere by Lebonnois et al. (2010). There is a greater discrepancy with the expression used by Kasting (1991), which has been used by much of the Mars and paleo-Earth modeling community. However, a review of the literature reveals that this formulation originated in a paper by Eastman (1929) and is intended for application from 300–2500 K.

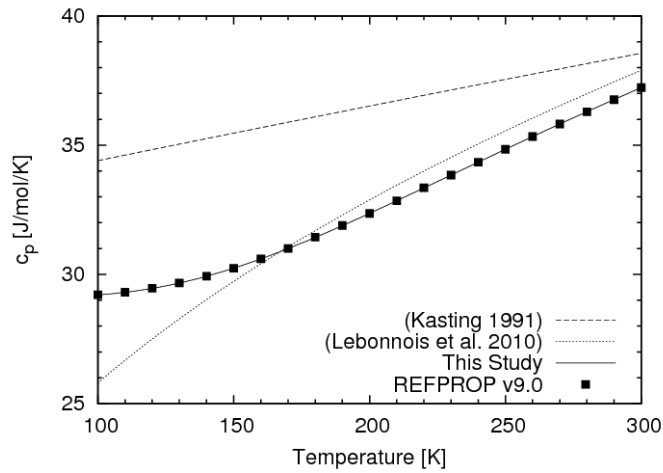


Figure A.1: Comparison of CO₂ specific heat capacity formulations.

At non-zero pressures the heat capacity must be corrected for the non-ideal nature of the gas. This is due to collisions with other molecules influencing the degrees of freedom in which the molecule stores energy. To make this correction the appendix of Wordsworth et al. (2010b) is followed. To summarize, the Redlich-Kwong EOS of Li et al. (2006) is used, having the form

$$p = \frac{RT}{v-b} - \frac{a}{v(v-b)\sqrt{T}} \quad (\text{A.2})$$

where p is pressure, v is volume, and a and b are parameters specific to the gas under

consideration. For the relatively low pressures considered here, this may be expressed as a Virial expansion

$$\frac{pv}{RT} \approx 1 + \frac{B}{v} = 1 + \frac{1}{v} \left(b - \frac{a}{RT^{3/2}} \right) \quad (\text{A.3})$$

The pressure correction to the heat capacity can then be calculated via the thermodynamic definition

$$\begin{aligned} c_p(p, T) &= c_p(0, T) - T \int_0^p \left(\frac{\partial^2 v}{\partial T^2} \right)_{p'} dp' \\ &= c_p(0, T) - T p \left(\frac{\partial^2 B}{\partial T^2} \right) \end{aligned} \quad (\text{A.4})$$

In practice, differentiating B analytically was found to be tractable. In the Redlich-Kwong formulation of Li et al. (2006), the parameter a is dependent on both p and T , with the form $a = a_1(T) + a_2(T)p$. However, the pressure correction to a is small, and unimportant for the relatively low pressures relevant to Mars' past (≤ 5 bar). I have thus neglected it. Calculating c_p by this method agrees well with the NIST REFPROP program over the range of pressures and temperatures considered in this study.

Testing the sensitivity of the radiative-convective model to the value of c_p found that the surface temperature is not strongly affected by the use of the formulation developed here as compared to that of Kasting (1991). Although the lapse rate increases significantly, a concurrent lowering in the height of the tropopause limits the surface temperature increase to at most a few K.

Appendix B: Vapor Pressure of H₂O₂

Here I develop two formulations for estimating the vapor pressure of H₂O₂ at low temperatures over the solid phase from the data available in the literature. The simpler approach is that taken by Lindner (1988) when examining H₂O₂ precipitation on modern Mars, and assumes a Clausius–Clapeyron form for the vapor pressure p at temperature T with constant latent heat L

$$L = T(V^G - V^C) \frac{dp}{dT} \quad (\text{B.1})$$

where V^G and V^C are the vapor and condensate molar volumes respectively. This may be simplified by substituting in $V^G = RT/p$ and $V^C \approx 0$, as the gas phase is relatively ideal and V^C is negligible compared to V^G at the low vapor pressures present over the solid phase. The latent heat of sublimation is estimated to be $L = 15.58 \text{ kcal/mol} = 65.19 \text{ kJ/mol}$ at the freezing point of H₂O₂, based on the sum of the latent heats of melting and vaporization (Schumb et al. 1955). To find the integration constant needed to solve Eq. (B.1) for p , it is convenient to use $p = 45.8 \text{ Pa}$ at the freezing point. This value was determined by using a four-parameter fit to extrapolate from measurements over the liquid phase which have been corrected for decomposition (Manatt & Manatt 2004). This gives the formulation

$$\ln p = 32.57 - \frac{7840}{T} \quad (\text{B.2})$$

This formula has a slope nearly identical to that of Lindner (1988), but it produces

significantly higher vapor pressures (+27%) due to the correction for H₂O₂ decomposition.

This simple extrapolation of vapor pressure may be improved upon by taking advantage of thermodynamic data available from the literature and applying the technique of King & Al-Najjar (1974). This approach is also based on the Clausius–Clapeyron relation, but accounts for non-constant L by using the thermodynamic relationship

$$\frac{dL}{dT} = C_p^0 - C_p^C + J \quad (\text{B.3})$$

where C_p^0 and C_p^C are the specific heat capacities at constant pressure of the gas phase (in the low pressure limit) and condensed phase respectively. The function J encapsulates non-ideal behavior of the vapor phase, and may be neglected if the gas is approximately ideal. The empirical criterion for a gas to be considered sufficiently ideal for this application is that the reduced temperature be < 0.45 . H₂O₂ has a critical temperature $T_C = 739.5$ K (Manatt & Manatt 2004), so its vapor phase may be considered ideal for $T < 330$ K. Since the freezing point of H₂O₂ occurs at 272.73 K (Schumb et al. 1955), it is acceptable to consider vapor over the solid phase to be an ideal gas, and J may be neglected in this analysis. Temperature dependent data for C_p^0 is obtained from the ideal gas thermodynamic tables of Dorofeeva et al. (2003) and C_p^C is taken from the experimental measurements of Giguère et al. (1954).

For many substances the relationship between T and dL/dT will be approximately linear when the vapor phase behaves ideally (King & Al-Najjar 1974). This is expressed

as

$$\frac{dL}{dT} = A + BT \quad (\text{B.4})$$

where A and B are coefficients fit from the heat capacity data. Integrating and combining Eqs. (B.3) and (B.4) produces expressions for the latent heat and vapor pressure

$$L = AT + \frac{1}{2}BT^2 + D \quad (\text{B.5})$$

$$\ln p = \frac{A}{R} \ln T + \frac{BT}{2R} - \frac{D}{RT} + E \quad (\text{B.6})$$

where D and E are constants of integration. Their values are determined using at least two measured values of L and/or p at known temperature(s). For these required data points the values of L and p at the freezing point from the literature are used, just as for the constant L formulation.

A plot of dL/dT versus T for H_2O_2 using data for C_p^0 and C_p^C from 150–270 K is given in Fig. B.1. As expected, the relationship is linear. A least-squares regression produces the coefficients $A = 21.34$ and $B = -0.1273$ with $R^2 = 0.9997$. Substituting these values into Eqs. (B.5) and (B.6) and using the values for L and p at the freezing point, the following formulations are obtained

$$L = 21.34T - 0.06365T^2 + 64100 \quad (\text{B.7})$$

$$\ln p = 2.567 \ln T - 0.007655T - \frac{7710}{T} + 19.79 \quad (\text{B.8})$$

with L in units of J/mol and p in units of Pa. In practice it is found that accounting for non-constant L produces a significant, but not dramatic, decrease in the estimate of H_2O_2

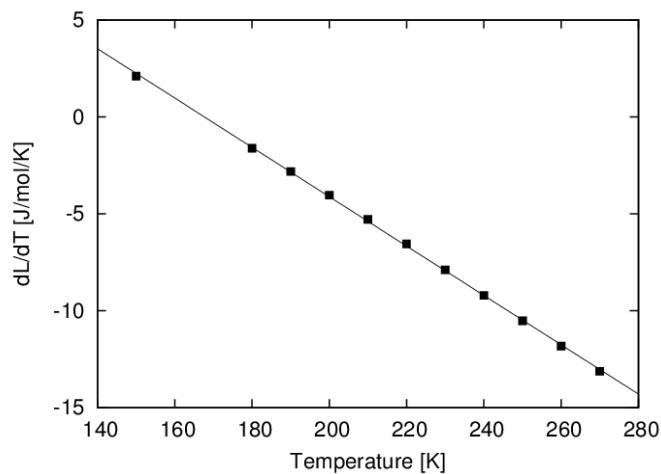


Figure B.1: Plot of dL/dT for H_2O_2 as a function of temperature, using the data of (Dorofeeva et al. 2003) and (Giguère et al. 1954). The line represents the linear fit $dL/dT = 21.34 - 0.1273T$.

vapor pressure at low temperatures. This is due to L being quite constant, varying only 1% between 270 K and 150 K, which translates into a difference in p of -18% at 150 K relative to assuming a constant L . Eq. (B.8) is used to calculate the vapor pressure of H_2O_2 in the results of this thesis.

Appendix C: Fate of Precipitated H₂O₂

I derive here an analytical model to determine the fate of an strong trace oxidizer (e.g. H₂O₂) dissolved in precipitation and deposited on a terrestrial surface. The goal is to find what fraction of the oxidizer is consumed by redox reactions in solution (e.g. with dissolved Fe²⁺), while the rest escapes by diffusion to the surrounding atmosphere. To obtain the time dependent profile of oxidizer concentration C as a function of depth z , a solution must be found to the partial differential equation

$$\frac{\partial C}{\partial t} = D \frac{\partial^2 C}{\partial z^2} - RC \quad (\text{C.1})$$

which is Fick's second law with effective diffusion coefficient D and an additional term on the rhs to allow for the reductive consumption of the oxidizer species at an effective rate R . Both D and R are taken to be constant in z and t . For R , this is equivalent to assuming that the dissolved reductant is either greatly in excess of the oxidizer or rapidly replenished from minerals in contact with the solution.

I will consider two exemplary geometries for the oxidation model. In the first, a storm event rapidly deposits a layer of precipitation, which then percolates into the unsaturated subsurface (the vadose zone). The precipitated oxidizing solution is treated as a slab of thickness d permeating the porous subsurface and bearing an initial oxidizer concentration $C(z, t=0) = C_0$. The coordinate $z = 0$ is located at the upper surface of the slab, which is not required to be the planetary surface. Here I am interested in transient

solutions of the diffusion equation, unlike the steady state solutions described in Chapter 4 for dry deposition of atmospheric oxidizers. Once I have solved for $C(z, t)$, the fraction of oxidizer consumed is defined as

$$X_{ox} = \frac{\int_0^{\infty} \int_0^d RC(z, t) dz dt}{\int_0^d C(z, 0) dz} \quad (C.2)$$

which is simply the amount of oxidizer consumed divided by the total initial amount.

To solve Eq. (C.1) a couple of boundary conditions (BCs) are required in addition to the initial condition. Assuming that both the bottom and top faces of the slab are open to atmosphere that is relatively poor in oxidizer (i.e. $C_{eq} \ll C_0$) allows the enforcement of the BCs $C \approx 0$ at $z = 0$ and $z = d$ for all times t . Assuming a separable form

$$C(z, t) = Z(z)T(t) \quad (C.3)$$

and substituting into Eq. (C.1)

$$Z \frac{\partial T}{\partial t} = DT \frac{\partial^2 Z}{\partial z^2} - RZT \quad (C.4)$$

the expression can be rearranged to isolate the z and t dependencies

$$\frac{1}{DT} \frac{\partial T}{\partial t} + \frac{R}{D} = \frac{1}{Z} \frac{\partial^2 Z}{\partial z^2} = -\lambda \quad (C.5)$$

where λ is some constant. This allows for solution of Z and T

$$Z(z) = A \sin(\sqrt{\lambda} z) + B \cos(\sqrt{\lambda} z) \quad T(t) = \Gamma e^{-(\lambda D + R)t} \quad (C.6)$$

Applying the BCs $C(0, t) = C(d, t) = 0$, it is clear that the B coefficients must be 0 and λ

$= (n\pi/d)^2$, where n is an integer. This gives a solution of the form

$$C(z, t) = \sum_{n=1}^{\infty} A_n \sin\left(\frac{n\pi z}{d}\right) e^{-\left(\frac{n\pi}{d}\right)^2 (D+R)t} \quad (\text{C.7})$$

The coefficients A_n are determined using the initial condition $C(z, 0) = C_0$

$$A_n = \frac{2C_0}{d} \int_0^d \sin\left(\frac{n\pi z'}{d}\right) dz' \quad (\text{C.8})$$

which results in $A_n = 0$ for even n and $A_n = 4C_0/\pi nd$ for odd n . Thus is obtained

$$C(z, t) = \frac{C_0}{d} \frac{4}{\pi} \sum_{n=0}^{\infty} \frac{1}{2n+1} \sin\left(\frac{n\pi z}{d}\right) e^{-\left(\frac{n\pi}{d}\right)^2 (D+R)t} \quad (\text{C.9})$$

Though this expression is not particularly elegant, its insertion into Eq. (C.2) followed by integration yields the remarkably simple solution

$$X_{ox} = 1 - \frac{2}{\xi} \tanh\left(\frac{\xi}{2}\right) \quad (\text{C.10})$$

where the non-dimensional parameter $\xi = d\sqrt{R/D}$ has been defined. This parameter encapsulates the competition between consumption via redox reaction and diffusive escape from the solution in determining the fate of the oxidizer. For $\xi \ll 1$ most of the oxidizer will escape, while for $\xi \gg 1$ most of it will be consumed. Plausible values of ξ for terrestrial planet conditions may be in either of these domains.

In the second geometry I consider, the precipitated layer of oxidizing solution is deposited in contact with a subsurface water table lacking oxidizer, which is taken to be a

semi-infinite slab. The initial condition is now C_0 for z from 0 to d , and 0 from d to ∞ . The upper boundary at the precipitant-atmosphere interface is taken to be $C = 0$ at $z = 0$ as before, while the lower boundary is now $C = 0$ at $z = \infty$. To solve Eq. (C.1) for this set of BCs, I choose to find the fundamental solution and convolute it with the initial condition. This is most readily achieved by first obtaining the fundamental solution for a different set of BCs, with $C = 0$ at $z = \pm\infty$. The initial condition for a fundamental solution is $C(z, t=0) = C_0 \delta(z)$, where δ is the Dirac delta function. Performing a Laplace transformation on Eq. (C.1) then gives

$$p \hat{c}(z, p) - C_0 = D \frac{\partial^2 \hat{c}}{\partial z^2} - R \hat{c}(z, p) \quad (\text{C.11})$$

and makes the new BCs $\hat{c}(z \rightarrow \pm\infty, t) = 0$. Using the substitution $q = \sqrt{(R+p)/D}$, Eq. (C.11) is then solved for \hat{c}

$$\hat{c}(z, q) = \frac{C_0}{2D} \frac{e^{-qz}}{q} \quad (\text{C.12})$$

Performing an inverse Laplace transformation produces the fundamental solution

$$C(z, t) = \frac{C_0}{\sqrt{4\pi Dt}} e^{-\frac{z^2}{4Dt} - Rt} \quad (\text{C.13})$$

This may be adjusted to the desired BCs of $C = 0$ at $z = 0$ and $z = \infty$ by applying the superposition principle and adding a reflection about the z axis with negative sign. The convolution of this fundamental solution and the initial condition of C_0 for z from 0 to d is then

$$C(z, t) = \frac{C_0}{\sqrt{4\pi Dt}} \int_0^\infty \left(e^{-\frac{(z-y)^2}{4Dt} - Rt} - e^{-\frac{(z+y)^2}{4Dt} - Rt} \right) (H(y) - H(y-d)) dy \quad (\text{C.14})$$

where H is the Heaviside step function. Performing the integration gives the solution

$$C(z, t) = C_0 \left[\operatorname{erf} \left(\frac{z}{\sqrt{4Dt}} \right) - \frac{1}{2} \operatorname{erf} \left(\frac{z-d}{\sqrt{4Dt}} \right) - \frac{1}{2} \operatorname{erf} \left(\frac{z+d}{\sqrt{4Dt}} \right) \right] e^{-Rt} \quad (\text{C.15})$$

where “erf” is the error function. With the domain of z extending to infinity, the fraction of oxidizer consumed is

$$X_{ox} = \frac{\int_0^\infty \int_0^\infty RC(z, t) dz dt}{\int_0^\infty C(z, 0) dz} \quad (\text{C.16})$$

which, following insertion of Eq. (C.15) and integration, becomes

$$X_{ox} = 1 + \frac{1}{\xi} (e^{-\xi} - 1) \quad (\text{C.17})$$

where ξ is defined as for the previous geometry.

Comparison of X_{ox} for the two geometries as a function of ξ reveals that while both have the same general behavior, contact with the water table dramatically increases the amount of oxidizer consumed at small ξ (Fig. C.1). At a qualitative level this is not surprising, since the oxidizer may only escape through the upper boundary in this geometry. However, the difference in oxidizer consumed can be quite large, over an order of magnitude for $\xi < 0.5$.

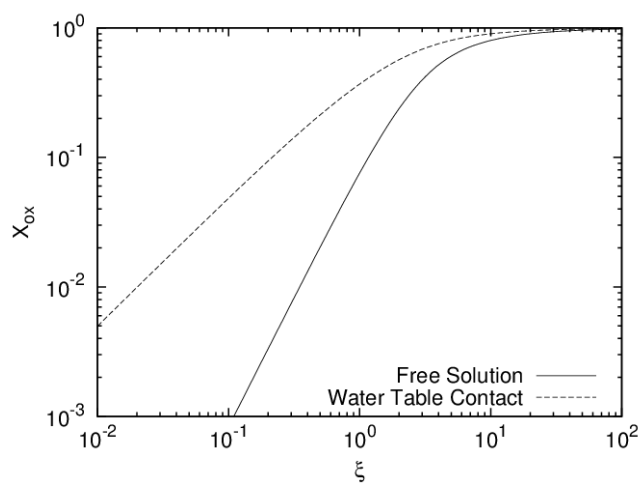


Figure C.1: Fraction of oxidizer consumed as a function of parameter ξ .